Doctoral Dissertation

博士論文

Observational Studies on Non-potential Magnetic Field in Solar Active Regions

(太陽活動領域における非ポテンシャル磁場の観測的研究)

A Dissertation Submitted for the Degree of Doctor of Philosophy

April 2019

平成31年4月博士（理学）申請

Department of Earth and Planetary Science

Graduate School of Science, The University of Tokyo

東京大学大学院理学系研究科地球惑星科学専攻

Yusuke Kawabata

川畑　佑典

Abstract

In the solar atmosphere, the regions where the strong magnetic field concentrates are called active regions. Active regions sometimes produce explosive events, such as solar flares and coronal mass ejections causing several influences to the geomagnetic environment. These explosive energy release events are produced by the energy stored in the magnetic field created by electric currents in the outer atmosphere, which is called a non-potential magnetic field. The main interest of this thesis is how the non-potential magnetic field is distributed in active regions. The measurements of the magnetic field have been mainly performed at the photospheric height. The coronal magnetic field measurements through polarimetric observations are difficult even with the state-of-art instruments. To overcome the difficulty, the nonlinear force-free field (NLFFF) modeling has been extensively used to infer the three-dimensional (3D) magnetic field in the solar corona. The main concept of the force-free field modeling is to extrapolate the coronal magnetic field from the spatial map of the magnetic field observed in the photosphere.

We attempt to investigate the non-potential magnetic field and its 3D structure in active regions, while we tackle the technical problem in the NLFFF modeling. We focus on two different viewpoints with the NLFFF modeling and observations. One is the non-uniqueness of the solution and the other is the force-freeness of the photospheric magnetic field. The novelties in our studies are followings. (1) We investigate the dependency of the NLFFF calculation with respect to the initial guess of the 3D magnetic field. While previous studies often use potential field as the initial guess in the NLFFF modeling, we adopt the linear force-free fields with different constant force-free alpha as the initial guesses.

This method enables us to investigate how unique the magnetic field obtained with the NLFFF extrapolation is. (2) We examine the direct measurements of the chromospheric magnetic field in the whole active regions through the spectropolarimetric observations at He I 10830 Å. The results of NLFFF extrapolation from the photosphere are compared with the direct measurements. The comparisons allow quantitative estimation of the NLFFF uncertainty.

With these novelties, we obtained following findings. (1) The dependence of the initial condition of the NLFFF extrapolation is smaller in the strong magnetic field region. Therefore, the magnetic field at the lower height (< 10 Mm) tends to be less affected by the initial condition (correlation coefficient $C > 0.9$ with different initial condition), although the Lorentz force is concentrated at the lower height. The 10-100 times larger Lorentz force, which is normalized by the square of the magnetic field strength, remains at the lower height ($<$ 10 Mm) than that at higher region ($>$ 10 Mm). (2) Chromospheric magnetic field may have larger non-potentiality compared to the photospheric magnetic field. The large non-potentiality in the chromospheric height may not be reproduced by the NLFFF extrapolation from the photospheric magnetic field. The magnitude of the underestimation of the non-potentiality at the chromospheric height may reach 30-40 degree in signed shear angle. Our results indicate that while the NLFFF extrapolation produces unique result at the lower height, the non-potentiality is underestimated at the chromospheric height. From a comparative analysis of the chromospheric magnetic field and the NLFFF extrapolation for two active regions, we reveal that the magnetic field in the upper atmosphere may have higher non-potentiality than previously thought based on the NLFFF modeling. Our studies emphasize the importance of the chromospheric magnetic field measurements for more accurate 3D magnetic field modeling and the understanding of the non-potentiality in active regions corona. Because the non-potentiality is crucial in the MHD instability, our findings would improve the understanding of the onset mechanisms for solar flares and CMEs, which affect the environment in the solar system. In the current state, the chromospheric magnetic field observations in active regions are very few in number. We strongly suggest that we should make efforts to perform much more observations of the chromospheric magnetic field in flare-productive active regions with the future large aperture telescopes, giving improvement of the 3D magnetic field modeling.

Acknowledgments

I would like to show my greatest appreciation to my supervisor, Dr. Toshifumi Shimizu for his insightful comments and suggestions throughout the course of my study. I would also like to express my gratitude to Dr. Satoshi Inoue and Dr. Andrés Asensio Ramos for helpful discussions as a collaborator. I have had the support and encouragement of all the members in my laboratory, T., Sakao, D., Brooks, T., Matsumoto, Lee Kyoung-Sun, Carlos Quite Noda, Y., Iida, S., Ishikawa, M., Ohyama, Y., Bamba, T., Okamoto, K., Watanabe, T., Kawate, T., Oba, R., Kanoh, M., Yamada, T., Hasegawa, T., Doi, M., Abe, K., Daiguji. I am also grateful to my family for their warm and hearty support. *Hinode* is a Japanese mission developed and launched by ISAS/JAXA, in collaboration with NAOJ as domestic partner, and NASA and STFC (UK) as international partners. The mission is operated by these agencies in cooperation with ESA and NSC (Norway). *Solar Dynamics Observatory* is a mission for NASA's Living With a Star program. The German Vacuum Tower Telescope is operated by the Kiepenheuer-Institut für Sonnenphysik at the Spanish Observatorio del Teide of the Instituto de Astrofísica de Canarias (IAC). The Dunn Solar Telescope is operated by the National Solar Observatory (NSO). Numerical computations were carried out on Supercomputer for earth Observation, Rockets, and Aeronautics (SORA) of Japan Aerospace Exploration Agency, JAXA.

Contents

Chapter 1

General Introduction

1.1 Magnetic Field in the Solar Atmosphere

In the Sun, there exists magnetic field with a wide range of scales and strengths. In this section, focusing on active regions, the property and role of the magnetic field in the solar atmosphere are summarized.

1.1.1 Active Regions and Sunspots

An active region is defined as an area with strong magnetic fields in the solar atmosphere. The other region where the strong magnetic field does not concentrate is called quiet region or quiet Sun. In the solar photosphere, active regions are observed as single sunspot or multiple sunspots, which are the cross-sections of the magnetic flux bundles, as shown in the black box of the upper panel of Figure 1.1. Sunspots and active regions have been intensely studied theoretically and observationally (see Solanki, 2003; Rempel & Schlichenmaier, 2011; Borrero & Ichimoto, 2011, for overviews). In the solar corona, which is an upper part of solar atmosphere located at a few to thousands Mm above the photosphere, loop-like structures can be seen above the active regions in the image of extreme ultraviolet (EUV) at 193 Å, as shown in the lower panel of Figure 1.1. The image of 193 Å is emission from hot coronal plasma (1 MK). From the ideal magnetohydrodynamics theory, the magnetic field lines are frozen into the plasmas (Priest, 2014). Therefore, we can regard the loop-like structure in the EUV image as the magnetic field lines extending from the solar surface.

Figure 1.2 shows the relation between the visible structure of the active region and line-of-sight (LOS) magnetic field. Active regions are numbered by the National Oceanic and Atmospheric Administration (NOAA). The active region in Figure 1.2 is numbered as NOAA 12599. Not just a simple dark spot, there are some fine structures in the sunspot (Schlichenmaier, 2009). The darkest region in the center of the sunspot is called an umbra and the surrounding bright and the filamentary structure is called a penumbra. The magnetic field tends to become weaker and to be inclined from the center of the umbra to the penumbra. The umbra has lower temperature than the penumbra and the quiet region because the strong magnetic field in the sunspot inhibits the heat transport by the convection. The magnetic field in active regions is thought to be created in the solar interior and emerge to the surface. After emerging from the solar interior, active regions evolve in a few days and decay in days to several weeks (van Driel-Gesztelyi & Green, 2015). When active regions emerge, they are usually composed of two spots with opposite polarities. These two spots are sometimes called leading spots and following spots, respectively. Observationally, it has been known that the following spots decay faster than the leading spots as shown in the negative polarity region in the bottom panel of Figure 1.2. Another prominent structure in active region is a plage. Plages are observed as bright disperse regions in the layer of $\sim$ 1000 km above the photosphere, which is called chromosphere. At the photospheric height, plages possess strong magnetic field corresponding to 1 kG, which can be seen as the disperse negative polarity region in the bottom panel of Figure 1.2. The size and the magnetic flux of plages in active regions also evolve with emergence and decay of sunspots. During the evolution, some active regions become more complex structure and store the non-potential magnetic energy, which is important process for initiating energetic events as mentioned in Section 1.1.2.

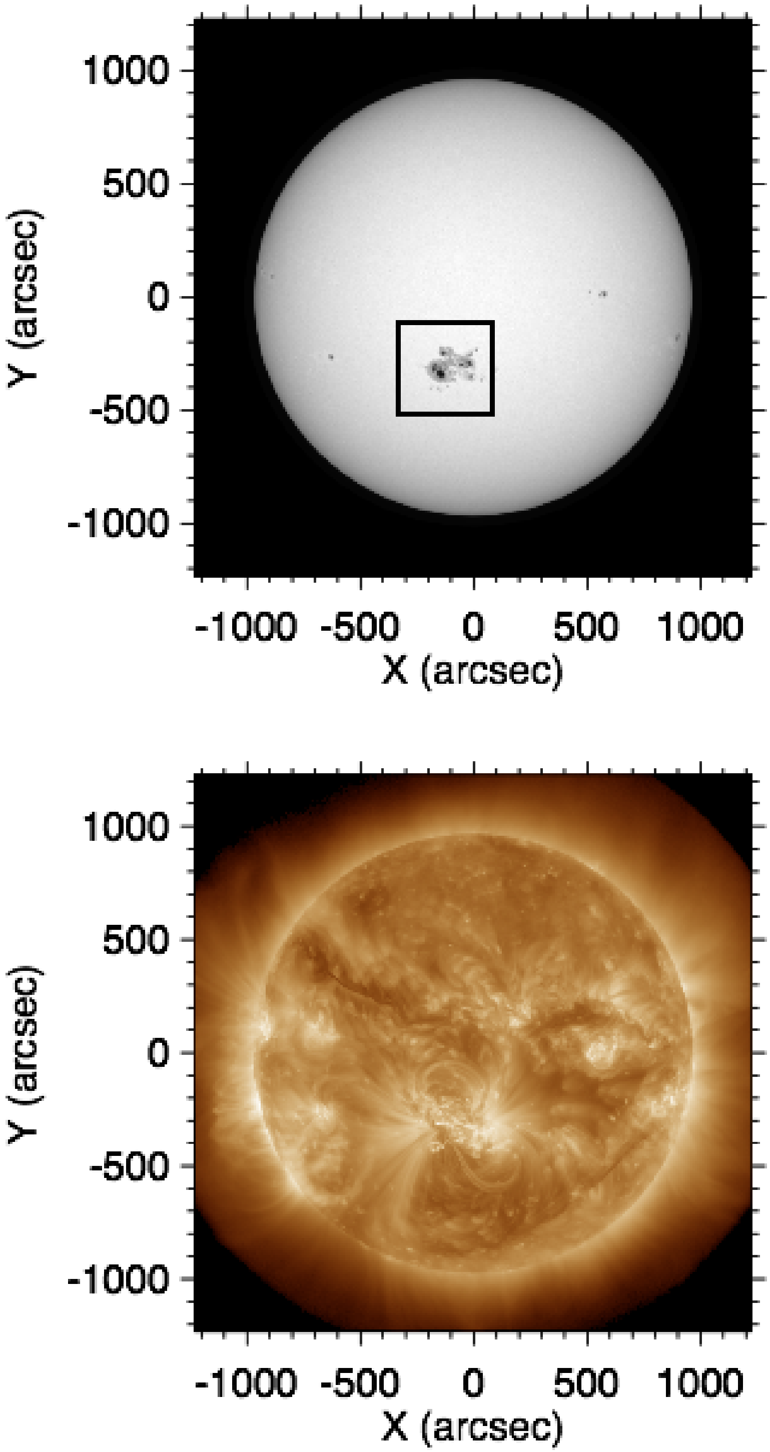

Figure 1.1: Upper panel: Continuum image observed with *Solar Dynamics Observatory* (*SDO*)/Helioseismic and Magnetic Imager (HMI) on 23 Oct 2014. The black box indicates the location of an active region. Lower panel: EUV image observed with *SDO*/Atmospheric Imaging Assembly (AIA) at 193 Å (Fe XII, XXIV) on 23 Oct 2014.

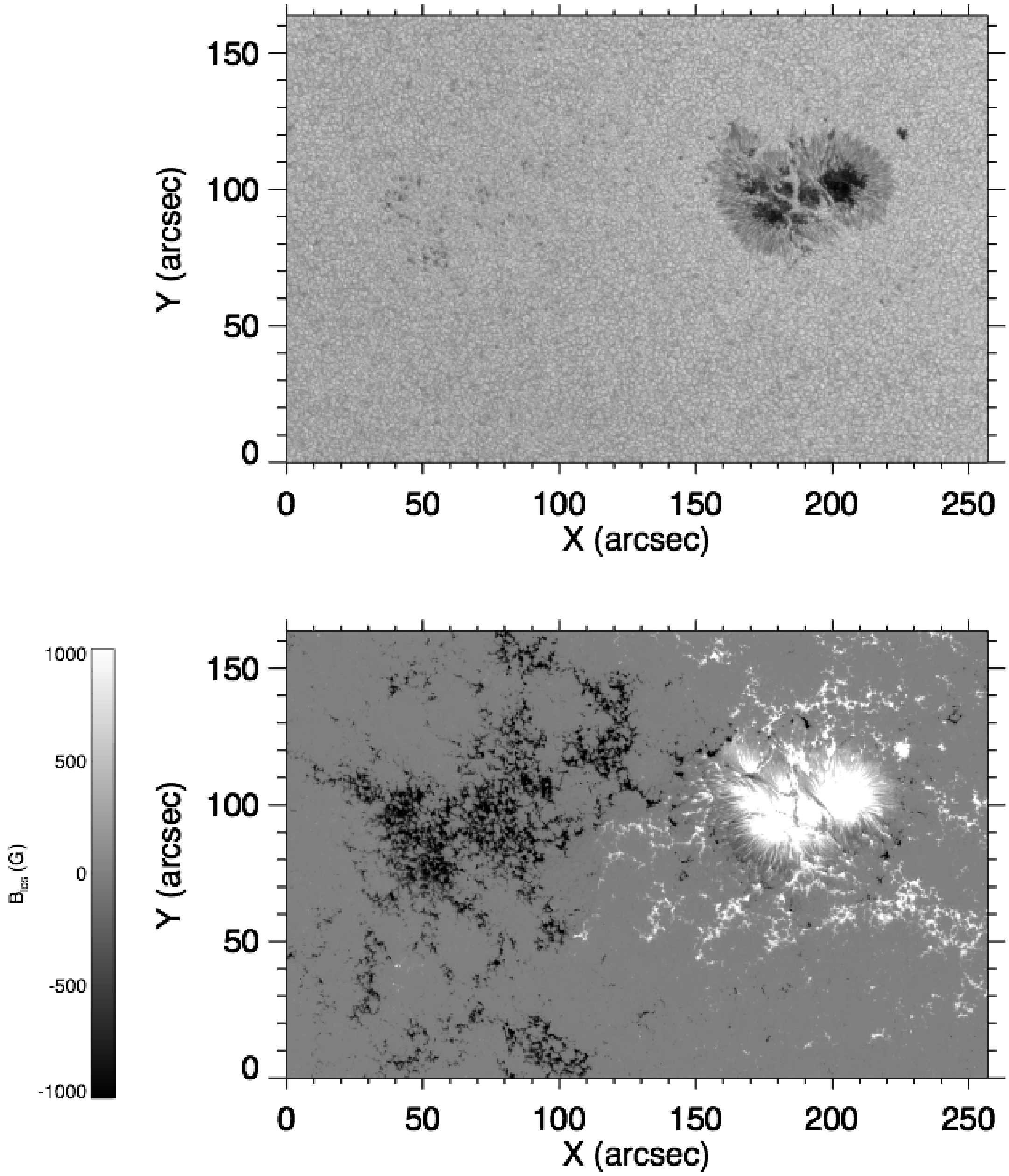

Figure 1.2: Upper panel:Continuum image of NOAA 12599 observed with *Hinode*/Solar Optical Telescope (SOT) SP on 8 Oct 2016. Lower panel: LOS magnetic field of NOAA 12599.

1.1.2 Non-potential Magnetic Field in the Solar Atmosphere

Active regions contain the strong magnetic field and sometimes produce explosive events by releasing the magnetic energy. The important fact is that active regions can not release all of the magnetic energy they have but the extra energy from the minimum energy state. The minimum energy state of the magnetic field above the photosphere is a potential field. The potential field is produced by electric currents in the solar interior and does not contain electric currents above the photosphere. Therefore, the potential field is sometimes called the current-free field. Explosive energy release events, such as solar flares and coronal mass ejections (CMEs), are produced by the magnetic field created by electric currents in the outer atmosphere, which is called a non-potential magnetic field. In other words, the deviation of the magnetic energy from the energy of the potential field (free energy) can be used for the explosive events,

$$E_{\mathrm{free}} = \int \frac{B^2 - B_{\mathrm{pot}}^2}{8\pi} dV, \tag{1.1}$$

where E_{free} is magnetic free energy, B is magnetic field, and B_{pot} is potential field.

When solar flares occur, electromagnetic radiation is emitted in the broad spectrum range from radio to γ-rays (Benz, 2017). Solar flares are often accompanied by CMEs, which are defined as ejections of large amounts of plasma from the solar corona into interplanetary space. Shearing, rotating, or emerging motion in the photosphere might transfer the non-potential magnetic energy from the photosphere to the corona (Krall et al., 1982; Hagyard et al., 1984; Leka et al., 1996). As a result, bundles of twisted field lines, which possess magnetic free energy, are formed in the solar corona. After the storage process, the coronal magnetic energy is released by the magnetic reconnection, which is triggered by loss of equilibrium of the twisted flux rope as shown in Figure 1.3. When the twisted flux rope (dashed line) erupts, overlying field lines (solid lines) are blown out and the magnetic reconnection occurs in newly formed anti-parallel field lines. The magnetic reconnection heats and accelerates the plasmas in the corona and produces bright two

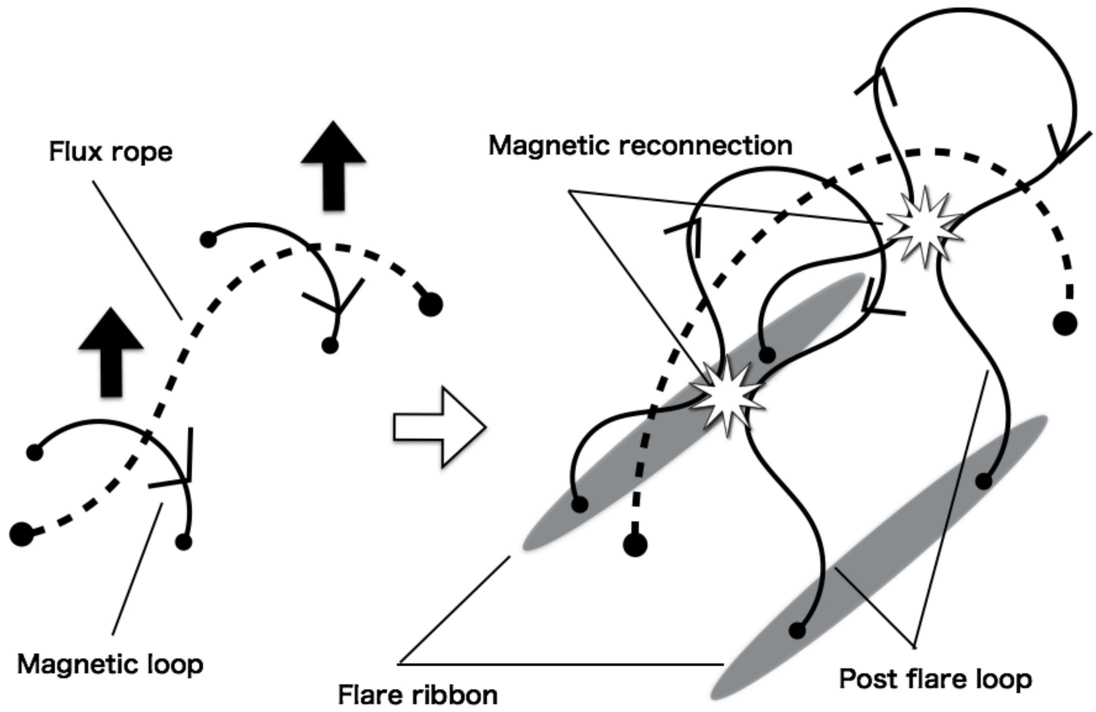

Figure 1.3: A twisted non-potential magnetic field line, which is called flux rope (dashed line) is formed under the potential-like overlying field lines. When the flux rope erupts by some mechanism of loss of equilibrium, overlying magnetic fields (solid lines) are blown out, resulting in the occurrence of the magnetic reconnection.

ribbons at the footpoint of field lines. On the other hand, the erupting coronal plasmas are identified as CMEs. The open question is what is the condition on the onset of the solar flares and CMEs.

Many models were proposed to explain the onset of solar flares and CMEs; break-out (Antiochos et al., 1999), tether cutting (Moore et al., 2001), preflare reconnection of emerging flux with pre-existing overlying magnetic fields (Kusano et al., 2012; Bamba et al., 2013; Wang et al., 2017) and magnetohydrodynamics (MHD) instabilities, such as torus instability (Kliem & Török, 2006) and kink instability (Kruskal & Schwarzschild, 1954). In any models, the occurrence of solar flares is closely related to the three-dimensional (3D) magnetic field configuration. Therefore, inferring correct 3D magnetic field is crucial task to understand the onset mechanism of solar flares and CMEs. As shown in the bottom panel of Figure 1.1, the qualitative identification of coronal magnetic field lines is possible by using EUV and/or X-ray observations. However, the quantitative information such as magnetic field strength can not be obtained with these observations. In addition, these kinds of observations suffer from the projection effects and superposition of multiple loops, which limit the detail understanding of 3D pictures. In solar observations, magnetic fields are often measured with polarimetric observations. Although the polarimetric observations are mainly performed at the photospheric height, those in the solar corona are quite difficult, which is described in Section 1.2. The alternative method to infer the coronal magnetic field is described in Section 1.3.

1.2 Magnetic Field Measurements through Polarimetric Observations

The magnetic field in the solar atmosphere is usually measured through the spectropolarimetric observations with slit-based or filter-based instruments. When there exists magnetic field in the solar atmosphere, spectral lines will split or widen, which is known as the Zeeman effect. Hale (1908) firstly detected the Zeeman effect in sunspots and showed that the spectropolarimetry can be used as a diagnostic of magnetic field in the solar atmosphere. In this section, the principle of the spectropolarimetric observations is presented.

In spectropolarimetric observation, we measure the Stokes parameters, which are defined as follows (del Toro Iniesta, 2007),

$$
\begin{aligned}
I &= \langle E_x^2 \rangle + \langle E_y^2 \rangle, \\
Q &= \langle E_x^2 \rangle - \langle E_y^2 \rangle, \\
U &= 2\langle E_x E_y \cos\phi(t) \rangle, \\
V &= 2\langle E_x E_y \sin\phi(t) \rangle,
\end{aligned}
\tag{1.2}
$$

where E_x and E_y are the amplitude of the electric field of the electromagnetic wave in x and y direction in the Cartesian coordinates, ϕ is the phase difference between them, and

t is the time, respectively. The physical meaning of the Stokes parameters (I, Q, U, and V) is as follows. Stokes I is the total intensity of the input light; Stokes Q and U show the intensity difference of two linearly polarized components (0° and $90°$ for Q, $45°$ and $135°$ for U); Stokes V is the intensity difference of two circularly polarized components. In practice, we measure only the intensity of the light $I_{\mathrm{meas}}(\theta, \delta)$ with varying observed angle θ and phase lag δ of the one component of $\boldsymbol{E}$ with respect to the orthogonal component.

The evolution of the Stokes parameters along the line-of-sight (LOS) is described by the radiative transfer equation (Trujillo Bueno, 2003),

$$\frac{d\boldsymbol{I}}{ds} = \boldsymbol{K}\boldsymbol{I} - \boldsymbol{\epsilon}, \tag{1.3}$$

where $\boldsymbol{I} \equiv (I, Q, U, V)^T$ is the Stokes vector (T denotes the transpose), s is the geometrical distance along the ray, $\boldsymbol{K}$ is the propagation matrix, and $\boldsymbol{\epsilon}$ is the emission vector. While the propagation matrix represents absorption and dispersion effects, the emission vector represents the emissive property of the medium. The emission vector and the propagation matrix are defined as following,

$$\boldsymbol{\epsilon} = (\epsilon_I, \epsilon_Q, \epsilon_U, \epsilon_V)^T, \tag{1.4}$$

$$\boldsymbol{K} = \begin{pmatrix} \eta_I & \eta_Q & \eta_U & \eta_V \\ \eta_Q & \eta_I & \rho_V & -\rho_U \\ \eta_U & -\rho_V & \eta_I & \rho_Q \\ \eta_V & \rho_U & -\rho_Q & \eta_I \end{pmatrix}, \tag{1.5}$$

where the matrix elements are composed of emission (ϵ_I, ϵ_Q, ϵ_U, and ϵ_V), absorption (η_I), dichroism (η_Q, η_U, and η_V), and dispersion (ρ_Q, ρ_U, and ρ_V) characteristics of the solar medium. By introducing the optical depth, defined $d\tau = -\eta_I ds$, the Equation (1.3) can be rewritten as,

$$\frac{d\boldsymbol{I}}{d\tau} = \boldsymbol{K}^*\boldsymbol{I} - \boldsymbol{S}, \tag{1.6}$$

where $\boldsymbol{K}^* = \boldsymbol{K}/\eta_I$, and $\boldsymbol{S} = \boldsymbol{\epsilon}/\eta_I$ is the source function vector. The propagation matrix and source function vector are functions of physical parameters of atmospheres, such as the temperature, electron pressure, the LOS velocity, the magnetic field vector. By performing the inversion of the radiative transfer equation, we can estimate these atmospheric parameters.

The spectropolarimetric observations have been performed by using mainly photospheric lines. The state-of-art spacecrafts, such as *Hinode* (Kosugi et al., 2007) and *Solar Dynamics Observatory* (*SDO*; Pesnell et al., 2012) have enabled us to observe magnetic field in the photosphere with high spatial resolution and high polarimetric accuracy. An example of spectropolarimetric observations of Fe I 6301.5 Å and 6302.5 Å with Solar Optical Telescope (SOT; Tsuneta et al., 2008; Shimizu et al., 2008; Suematsu et al., 2008; Ichimoto et al., 2008)/Spectropolarimeter (SP; Lites et al., 2013) aboard the *Hinode* satellite is shown in Figure 1.4. Red lines show the Stokes parameters in the sunspot, while blue lines show those in the quiet sun. The Zeeman effect can be clearly seen in the Stokes parameters of the red lines. While photospheric magnetic field can be inferred with high accuracy through spectropolarimetric observations, it is difficult to obtain magnetic field in the corona. In the corona, the polarimetric signal is weak and is suffered from large doppler broadening since the magnetic field in active regions is smaller at the coronal height ($10 \sim 100$ G) than at the photospheric height ($100 \sim 3000$ G) and the temperature is higher in the corona (1 MK $\sim$) than in the photosphere (~ 6000 K).

1.3 Force-Free Field Extrapolation

1.3.1 Formulation of Force-Free Field Extrapolation

As described in Section 1.2, vector magnetic fields are mainly obtained in the photosphere. The energy release sites of solar flares exist in the corona, where it is challenging to measure the magnetic field because of low signal of polarization. Although EUV and/or

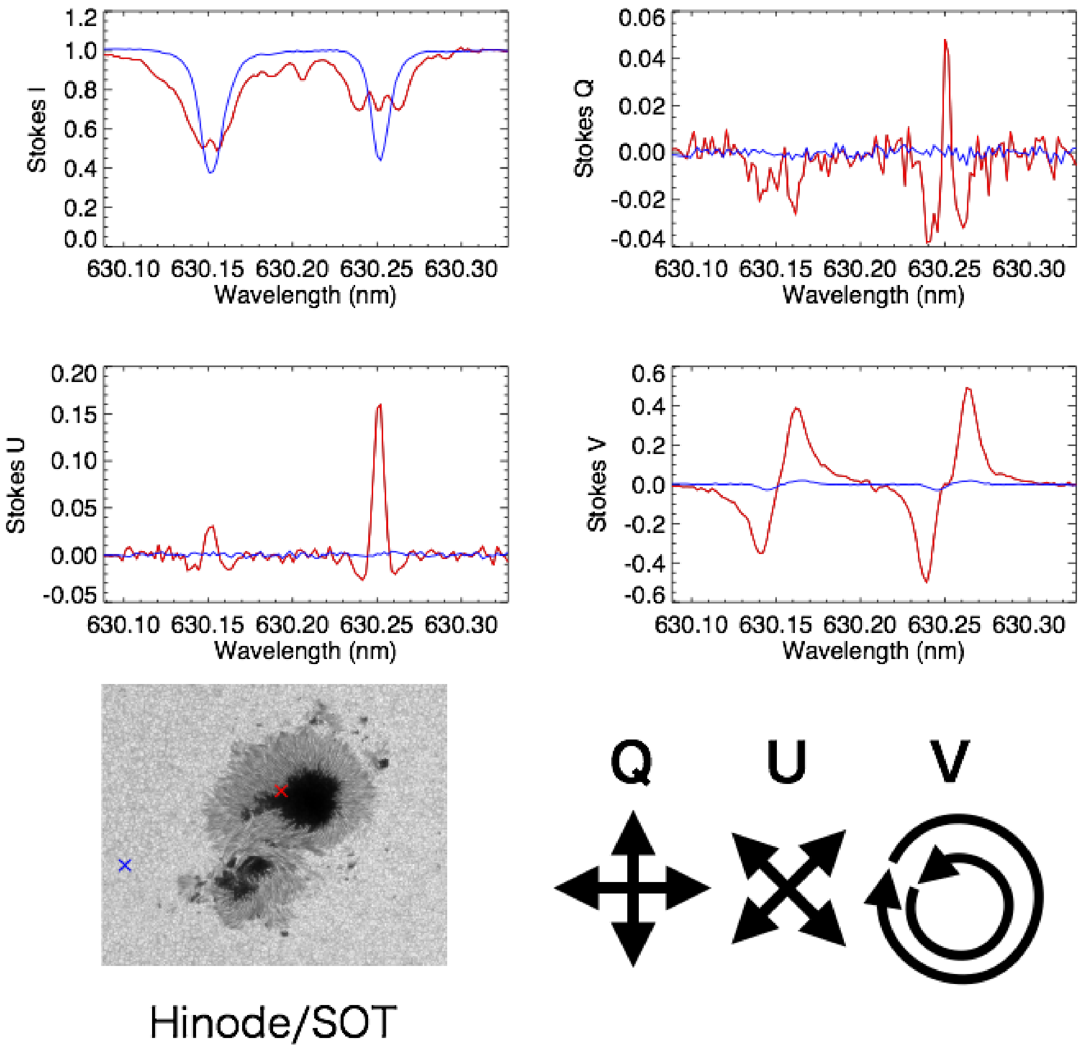

Figure 1.4: Full stokes vector of sunspot (Red) and quiet sun (Blue) observed with *Hinode*/SOT SP at Fe I 6301.5 Å and 6302.5 Å.

X-ray imaging observations provide the morphological information of the coronal magnetic structures, it is difficult to conduct the quantitative discussion. The force-free field modeling is one of the alternative methods to infer the 3D magnetic field in the solar corona. The main concept of the force-free field modeling is to extrapolate the coronal magnetic field from the spatial map of the magnetic field in the photosphere based on two assumptions (Wiegelmann & Sakurai, 2012). First assumption is the mechanical equilibrium of the plasmas in the solar corona. The Alfvén transit time in the coronal loop in active regions is a few to five minutes (Alfvén speed is 1000 km $\sim$ and the size of active region is 100 Mm$\sim$). On the other hand, the coronal magnetic loops in the EUV and X-ray images seem to be unchanged on timescales of order one hour. These facts support the assumption that the magnetic field in the solar corona evolves in the quasi-static state. Second assumption is the domination of the Lorentz force in the solar corona. In the solar corona, the plasma $\beta(= 8\pi p/B^2)$, which is the ratio between the plasma pressure and the magnetic pressure, is thought to be sufficiently small, $\beta \ll 1$ as shown in Figure 1.5 (Gary, 2001).

The above two assumptions lead to the condition that the Lorentz force vanishes in the solar corona, i.e., the magnetic tension and the magnetic pressure are balanced. That is,

$$\boldsymbol{j} \times \boldsymbol{B} = 0, \tag{1.7}$$

where $\boldsymbol{j}$ is the current density, and the current density follows the Ampére's law

$$\nabla \times \boldsymbol{B} = \frac{4\pi}{c}\boldsymbol{j}. \tag{1.8}$$

Equation (1.7) can be written

$$\nabla \times \boldsymbol{B} = \alpha(\boldsymbol{r})\boldsymbol{B}, \tag{1.9}$$

where α is called the force-free parameter, which has a spatial dependence. From the

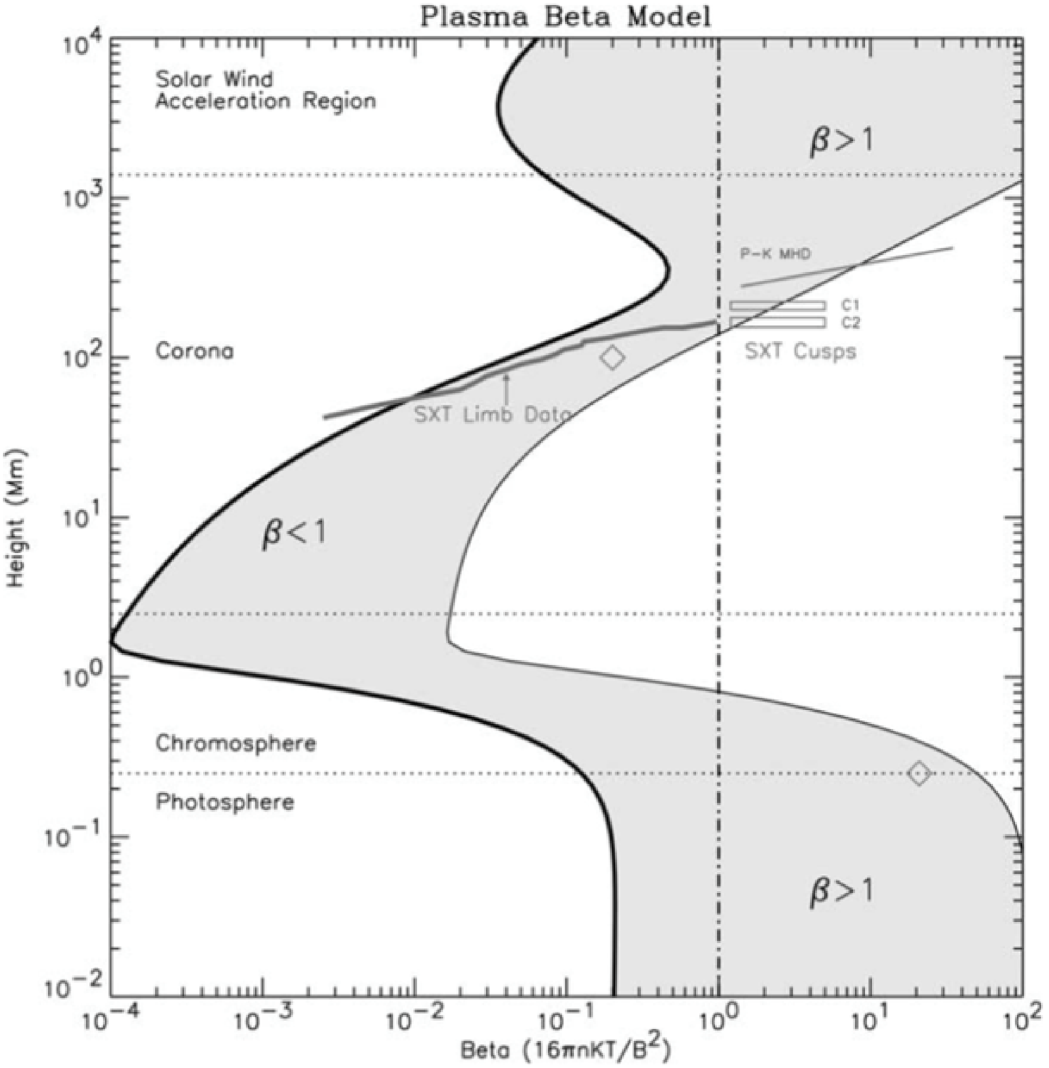

Figure 1.5: Variation of plasma β with hight (Gary, 2001). While in the photosphere plasma β is more than unity, it becomes sufficient small($\ll 1$) in the corona. The heavy line and the thin line correspond to the sunspot of 2500 G and the plage region of 150 G, respectively. Reproduced with permission of Springer Science and Business

divergence free condition of magnetic field,

$$\boldsymbol{\nabla} \cdot \boldsymbol{B} = 0. \tag{1.10}$$

By taking the divergence of Equation (1.9) and using Equation (1.10),

$$\boldsymbol{B} \cdot \boldsymbol{\nabla}\alpha = 0. \tag{1.11}$$

Equation (1.11) indicates that the α is constant along the field line. Equations (1.9) and (1.11) are mathematically equivalent to Equations (1.7), (1.8), and (1.10). Therefore, we have to solve either set of equations when performing the force-free field extrapolation.

Depending on the spatial distribution of α, the equations of force-free field will become simple. The most simple approximation of the force free field is called potential field (or current-free field $j = 0$). Equation (1.9) reduces the Laplace equation

$$\nabla^2\Psi = 0, \tag{1.12}$$

where Ψ is the scalar magnetic potential. Similar to potential field, if α is constant everywhere, the field is called linear force-free field (LFFF). Equations (1.9) and (1.10) become a Helmholtz equation

$$\Delta\boldsymbol{B} + \alpha^2\boldsymbol{B} = 0. \tag{1.13}$$

The equations of potential field and LFFF can be solved by a Green's function method (Chiu & Hilton, 1977) or a Fourier method (Alissandrakis, 1981).

On the other hand, if α is not a constant in space, the field is called nonlinear force-free field (NLFFF). Different from potential field and LFFF, we need numerical techniques to compute NLFFF. The most simple method is the vertical integration method proposed by Nakagawa (1974). The method is not iterative and just integrate Equation (1.9) from the photospheric vector magnetic field. This approach, however, is mathematically ill-posed and known to be unstable. Therefore, other algorithms have been developed to compute NLFFF fields. There exist mainly two approaches. First approach is to solve the NLFFF equations with the boundary conditions, which is a mathematically well-posed problem. The example of this approach was proposed by Grad & Rubin (1958), and so is often called Grad-Rubin method. In this approach, the distribution of α in only one polarity and the vertical magnetic field are prescribed to the bottom boundary. Bineau (1972) has proved the existence of the stable and unique solution of NLFFF in the bounded domain with small α values. One weak point of this approach is that the vector magnetic field on the bottom boundary is not consistent with the observed photospheric magnetic field. Second approach is to find the closest force-free equilibrium field matching the observed vector magnetic field in the photosphere, which is prescribed to the bottom boundary. While this approach keeps the bottom boundary consistent with the observed magnetic vector in the photosphere, this approach is an ill-posed problem and there is no proof of unique and stable solutions. The examples of this approach are the optimization methods (Wheatland et al., 2000; Wiegelmann & Neukirch, 2006) and the magnetohydrodynamics (MHD) relaxation methods (Chodura & Schlueter, 1981; Mikic & McClymont, 1994; Inoue et al., 2014).

1.3.2 Application of NLFFF Extrapolation to Solar Photospheric Magnetic Field

Since the space-borne telescope, such as *Hinode* and *SDO*, made it possible to regularly measure the photospheric vector magnetic field with high precision, the NLFFF extrapolation has been widely used as the tool for inferring the coronal magnetic field. In this section, previous studies, which applied the NLFFF modeling to solar observations, are summarized. We focus on the topics about the energy storage and the onset mechanism of solar flares.

Regarding the energy storage problem, Schrijver et al. (2008) applied NLFFF to real solar observations with *Hinode* SOT/SP. They found that strong electrical currents emerge together with magnetic flux before the occurrence of solar flares and that magnetic energy decrease of $\sim 10^{32}$ erg with the coronal electrical currents after the solar flares, which is comparable energy to solar flares and CMEs. Sun et al. (2012) investigated the temporal evolution of the magnetic energy and free energy based on the NLFFF extrapolation from the photosphere. They reported that the magnetic free energy reaches a maximum of $\sim 2.6 \times 10^{32}$ erg and 0.34×10^{32} erg decrease is found within 1 hr after the X-class flare. They also showed that over 50 % of the free energy is stored in the volume below the 6 Mm height. Kawabata et al. (2017) investigated the formation of the non-potential field in the X-shaped quadrupolar structure. The temporal three-dimensional magnetic field evolution shows that the sufficient free energy had already been stored more than 10 hr before the occurrence of the M-class flare and that the storage was observed in a localized region (around one polarity in the quadrupolar structure).

The onset mechanism was also studied through analyzing the 3D magnetic field structure just before the occurrence of the solar flares. Savcheva et al. (2012) presented the magnetic field topology analysis of sigmoidal structure based on the NLFFF modeling using *Hinode* data. They found that the characteristic magnetic field structure, which is called hyperbolic flux tube (HFT), was formed before the occurrence of solar flares. The HFT is a place where the current sheets can develop and reconnection is most likely to occur (Titov, 2007). They suggested that the magnetic reconnection at the HFT drives loss of equilibrium via the torus instability. Inoue et al. (2013) studied the three-dimensional magnetic structure focused on the magnetic twist in the solar active region. They showed that the magnetic twist over the half-turn was built up just before the M6.6 and X2.2 flares and disappeared after the flare events. On the other hand, the magnetic twist remained after M1.0 and M1.1 flares. They suspected that the weakly twisted lines surrounding around the strongly twisted lines might suppress the activity of the strongly twisted lines. Kawabata et al. (2017) found that the free energy in the localized region in the quadrupolar active region decreased just 1 hour before the solar flare, implying the occurrence of the precursor reconnection proposed by the tether cutting model (Moore et al., 2001) or breakout (Antiochos et al., 1999). The NLFFF modeling is also used for the initial condition of the MHD simulation to investigate the dynamics of solar flares. Amari et al. (2014) studied the coronal field response to the photospheric magnetic field change with MHD simulation by using the NLFFF as an initial condition. They showed that when the magnetic energy stored in the NLFFF is too high, no equilibrium is possible Muhamad et al. (2017) conducted three-dimensional magnetohydrodynamic simulations by using the NLFFF from the photospheric magnetic field observation as the initial condition. They gave the artificial magnetic disturbance to the initial NLFFF by injecting the small emerging bipole . They confirmed that the emergence of the small bipole into the highly sheared global magnetic field of an active region can effectively trigger a flare, as proposed by Kusano et al. (2012). Inoue et al. (2018) also studied the triggering process and initial dynamics of solar flares by performing MHD simulation by using the NLFFF. They found that the tether-cutting reconnection raise the twisted flux rope to the toroidal unstable area and drive the eruption.

The results of the previous studies above depend on the accuracy of the NLFFF modeling. Although many previous studies applied NLFFF to solar active regions and showed qualitatively agreement between NLFFF and coronal images (Régnier & Amari, 2004; Valori et al., 2012; Sun et al., 2012; Inoue et al., 2012; Jiang et al., 2014; Wang et al., 2014; Kawabata et al., 2017; Muhamad et al., 2018), there still exist some regions where NLFFF produce quite different field lines from coronal images (De Rosa et al., 2009). As shown in Section 1.4, there are several remaining problems of the NLFFF modeling we have to solve.

1.4 Remaining Problems

1.4.1 Non-uniqueness of NLFFF

The mathematical problem of the NLFFF is the existence of the stable and unique solution of the NLFFF. The existence of unique solution of the NLFFF has not been proved except for the limited case (Bineau, 1972). In addition to the mathematical problem, the NLFFF applications to the solar observations have some uncertainties, e.g., observational errors and numerical methods. The question is, in practical way, how large the uncertainty of the NLFFF modeling is. In other words, is there a possibility that completely different NLFFF results are obtained based on the same bottom boundary? Schrijver et al. (2006) applied six NLFFF algorithm to analytical force-free field solutions and compared solutions with each other. The best method reproduced the total energy in the magnetic field within 2% error. They also found that the NLFFF in the outer domains of the volume depends sensitively on the details of the specified boundary conditions. Metcalf et al. (2008) also compared NLFFF methods by using solar-like reference model. They applied NLFFF methods to both forced (not force-free) and force-free bottom boundaries. They show that while the NLFFF with the force-free bottom boundary reproduced helical flux bundle, that with forced bottom boundary did not reproduce reference model well. Their results suggest the importance of the force-freeness in the bottom boundary, which will be mentioned in detail in Section 1.4.2. De Rosa et al. (2009) applied various kinds of NLFFF algorithm (Grad-Rubin, optimization, and MHD relaxation) to the photospheric magnetic field observed with Hinode and investigated how different the solutions from different algorithm are. They evaluated the magnetic energy, E_B, normalized by potential magnetic energy, $E_{\rm pot}$,

$$\frac{E_B}{E_{\rm pot}} = \frac{\frac{1}{8\pi}\int B^2 dV}{\frac{1}{8\pi}\int B_{\rm pot}^2 dV}, \tag{1.14}$$

where $B_{\rm pot}$ is the potential magnetic field. The normalized energy has a range of 0.87-1.25 in different algorithms. In terms of the morphology of 3D field lines, they compare field lines with images. They found that field lines from NLFFF do not agree with EUV images and the average misalignment is 20-40 degrees. They suspected that small field of view (FOV) of the observation and the projection effect might cause this alignment. This result implies that we have to improve NLFFF to converge appropriate solution. Thalmann et al. (2013) investigated the effect of the observational instrument on the solution of NLFFF. They used a photospheric magnetic field observed with different instrument, i.e. , the *Hinode*/SOT SP and *SDO*/Helioseismic and Magnetic Imager (HMI; Schou et al., 2012). They concluded that the relative estimates such as normalized magnetic energy and the overall structure of the magnetic fields might be reliable, although there were remarkable deviations in the absolute value between the instruments. DeRosa et al. (2015) investigated the influence of spatial resolution on NLFFF with three kinds of methods similar to De Rosa et al. (2009). They showed that the free energy tends to be higher with increasing resolutions and magnetic helicity values vary significantly among different resolutions. They recommended that the consistency between modeled field lines and the coronal loop images should be checked before using NLFFF in a scientific setting.

In previous studies above, they showed how different results NLFFF produced. In terms of total magnetic energy, the difference of method did not produce large difference, less than 15 %, if we do not consider the Grad-Rubin method, i.e., consider only the method using the same bottom boundary (De Rosa et al., 2009). The questions is whether the completely different solutions are produced or not based on the same bottom boundary, in other words, how unique the solution is when focusing on one method. If completely different solutions exist, how can we obtain the result most consistent to the coronal imaging observations? As we mention in Section 1.3.2, in some cases, NLFFF showed qualitatively agreement with coronal images, in the other cases, NLFFF produce quite different field lines from coronal images (De Rosa et al., 2009). Therefore, the problem we have to tackle is to reveal whether completely different solution with same bottom boundary can exist or not in the practical calculation and what we should do in case that the modeled field lines do not agree with the coronal images.

1.4.2 Validity of Force-Free Assumption

One of the most controversial problems in NLFFF extrapolation is force-freeness in the photosphere. As shown in Figure 1.5 from the model of Gary (2001), the plasma beta in the plage region in the photosphere is order of 10^2, while the center of sunspot is almost force-free. This result is often cited as the non-force-freeness in the photosphere.

There are some previous studies to investigate the force-freeness in the active regions in the photosphere based on the necessary condition of the force-free approximation shown by Low (1985). The Lorentz force can be written as the divergence of the Maxwell stress tensor,

$$M_{ij} = -\frac{B^2}{8\pi}\delta_{ij} + \frac{B_i B_j}{4\pi}. \tag{1.15}$$

Assuming that the strength of magnetic field vanishes in the infinity height, the volume-integrated Lorentz force can be written by the surface integrals,

$$F_x = \frac{1}{4\pi}\int B_x B_z dxdy, \tag{1.16}$$

$$F_y = \frac{1}{4\pi}\int B_y B_z dxdy, \tag{1.17}$$

$$F_z = \frac{1}{8\pi}\int (B_z^2 - B_x^2 - B_y^2) dxdy. \tag{1.18}$$

According to Low (1985), in oder to regard the magnetic field as being force-free state, three components of the net Lorentz force are necessary to sufficiently be smaller than the integrated magnetic pressure force,

$$F_p = \frac{1}{8\pi}\int (B_x^2 + B_y^2 + B_z^2) dxdy. \tag{1.19}$$

Metcalf et al. (1995) investigated the force-freeness in the photosphere and the chromosphere by observing Na I 5896 Å line. They showed that while $|F_z|/F_p \sim 0.4$ in the photosphere, $|F_z|/F_p$ becomes 0.1 roughly 400km above the photosphere and concluded that the photosphere is not force-free but the chromosphere is. Moon et al. (2002) analyzed 12 magnetograms from Fe I 6301.5 and 6302.5 Å lines and showed that the value of $|F_z|/F_p$ ranges form 0.06 to 0.32 with a median value of 0.13. This result implies that the photospheric magnetic field is not far from the force-free state. On the other hand, Liu et al. (2013) performed statistical study of the force-freeness (925 magnetograms) and found that only 25 % of the active regions satisfy $|F_z|/F_p < 0.1$. It should be noted that the conditions described above is not sufficient condition for force-free.

The validity of the NLFFF modeling has been checked by the X-ray and/or EUV imaging observations. As described above, imaging observations has a disadvantage that the quantitative information such as magnetic field strength can not be obtained. Moreover, X-ray and/or EUV observations suffer from the projection effects and projection of multiple loops. Therefore, how the non-force-freeness in the photosphere can affect the 3D configuration of the magnetic field in the NLFFF modeling is unclear.

1.5 Approach to the Problems

In this thesis, we tackle the two problems mentioned in Section 1.4 by examining the following two topics.

1.5.1 NLFFF from Different Initial Conditions

To investigate whether completely different solutions with the same bottom boundary exist or not, we evaluate NLFFF extrapolation with different initial conditions. As is often the case with the nonlinear inverse problems, the different initial guesses may often produce completely different converged solutions. Therefore the uniqueness of the NLFFF calculation can be studied by giving different initial conditions.

The NLFFF extrapolation is usually performed as follows,

(1) Set the 3D initial condition by using photospheric vertical magnetic field.

(2) Give the information of the horizontal magnetic field to the bottom boundary.

(3) Perform some relaxation process.

In the process (1), almost all previous studies use the potential field as an initial condition. We perform NLFFF calculation not only with the potential field but also with linear force-free field as an initial condition. Several force-free alpha values are given in the linear force-free case. Comparisons among the NLFFF results with different initial conditions will provide some insights to the uniqueness of the NLFFF extrapolation.

1.5.2 Observations of Chromospheric Magnetic Field

To reveal the non-potentiality of the magnetic field in the upper atmosphere, we make use of spectropolarimetric observations with chromospheric spectral lines for a couple of active reigons and derive the chromospheric magnetic field. The derived chromospheric magnetic field is compared with the potential as well as NLFFF from the photospheric magnetic field. The chromosphere is an intermediate layer between the photosphere and corona, which exists at 1000-2000 km height from the photosphere. There are several benefits from the measurements of the chromospheric magnetic field in terms of the understanding of the phenomena occurring in active regions. First, the magnetic field in the chromosphere will play an important role in improving the extrapolation method. As above, the force-freeness of the photospheric magnetic field in active regions is controversial, whereas the chromospheric magnetic field is thought to be sufficiently force-free (Metcalf et al., 1995; Gary, 2001). Therefore, using the chromospheric magnetic field as the bottom boundary has high expectations to improve the NLFFF modeling. Second, we can quantitatively validate the NLFFF modeling from the photospheric magnetic field and discuss the effect of the non-force-freeness to the extrapolation. Third, in terms of solar flares, the magnetic reconnections in the chromospheric layer is attracting attention as an onset mechanism of solar flares (Kusano et al., 2012; Bamba et al., 2013; Wang et al., 2017).

Accurate measurements of the chromospheric magnetic field are challenging but an highly important effort. The magnetic field in the chromosphere has been attempted to be measured similar to photospheric magnetic field (see the review of de la Cruz Rodríguez & van Noort, 2017). The common spectral lines for the diagnostics of the chromospheric layer observed by the ground-based telescope are the Ca II H & K lines (3934 and 3968 Å), Hα (6563 Å), Ca II infrared lines (8949, 8542, and 8662 Å), and He I lines (5876 and 10830 Å). In the solar atmosphere, the Zeeman effect and the Hanle effect are the primary mechanisms to produce polarimetric signals in these spectral lines in the presence of the magnetic field. The Hanle effect modifies polarization signals which are produced by scattering polarization when the magnetic field is inclined with respect to the local solar vertical direction (Trujillo Bueno, 2001). Compared to the Zeeman effect, the Hanle effect is sensitive to weak field in the range between 1 and 100 G for typical solar spectral lines. One of the difficulties to infer the magnetic field in the chromosphere from the spectropolarimetric observations is the necessity of the consideration of the complex atmospheric model. For example, as shown in Figure 1.6, the spectral lines of Ca II K line and Hα have broad range of the solar atmosphere (Vernazza et al., 1981). This fact means that the complex atmospheric model must be considered, when solving the radiative transfer equations.

In this thesis, to avoid construct complex model atmosphere, He I 10830 Å will be used for the diagnostics of the chromosphere. He I 10830 Å results form the transition between terms of the triplet system of helium ($2s^3S$ and $2p^3P$). This line has a different property from Ca II lines and Hα presented above. In the condition of the collisional rates in the chromosphere, the lower term of He I 10830 Å ($2s^3S$) can not be populated. The only way to populate the lower term is the EUV radiation from the corona. Therefore, the formation layer of He I 10830 Å is thinner compared to other chromospheric lines, which makes possible to interpret the line as constant slab or Milne-Eddington atmosphere. The detail method to invert the spectropolarimetric data will be described in Chapter 3.

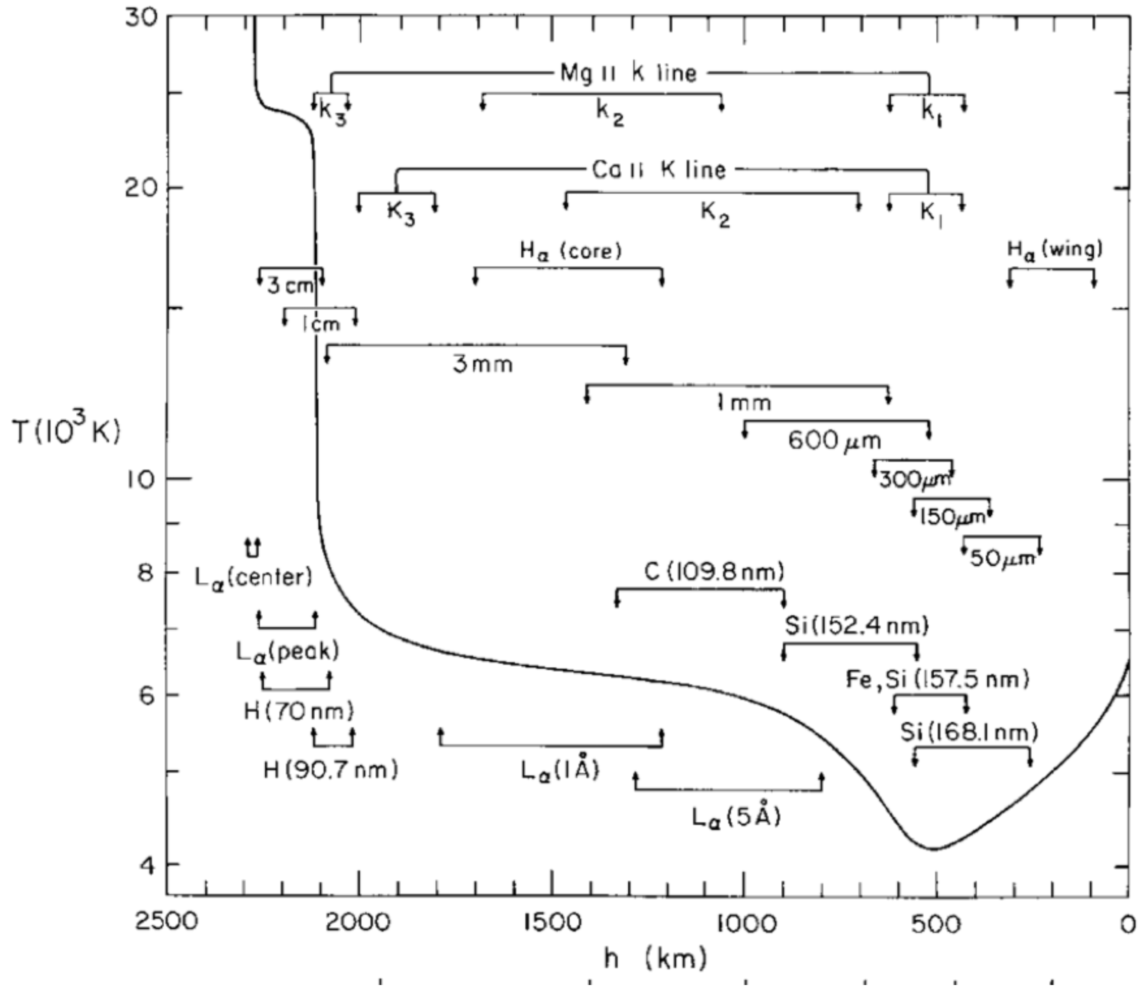

Figure 1.6: Temperature variation as a function of height and formation height of each spectral line.From Vernazza et al. (1981).ⓒAAS. Reproduced with permission

1.6 Purpose of Thesis

In this thesis, we attempt to investigate the distribution of non-potential field at the upper atmosphere and evaluate whether NLFFF extrapolations can predict it reasonably. In Chapter 2, the NLFFF extrapolations are performed with different initial conditions in order to investigate how many solutions will appear under the single bottom boundary and how different each solution is. In Chapter 3, the chromospheric magnetic field is derived from the spectropolarimetric observations at He I 10830 Å and the field is compared with the NLFFF extrapolation from photospheric field. We investigate whether a state-of-art NLFFF modeling can predict the observed chromospheric field and study what kind of difference is there between modeling and observation. In Chapter 4, we discuss our results and present future prospects. We summarize our findings and present a conclusion in Chapter 5.

Chapter 2

Initial Condition Dependence in NLFFF Modeling

2.1 Introduction

In this chapter, we investigate how different the results of the NLFFF modeling will be when the the different initial conditions are given. As mentioned in Section 1.4.1, previous studies show that different results are obtained depending on the calculation methods used in the NLFFF modeling (Schrijver et al., 2006; Metcalf et al., 2008; Schrijver et al., 2008; De Rosa et al., 2009). The one of the causes of the difference between the Grad-Rubin method and the other two methods (optimization and MHD relaxation methods) is the treatment of the bottom boundary. Because the former method relax the 3D magnetic field so that the force-free alpha along the magnetic field line is constant, the horizontal component of magnetic field at the bottom boundary is different from the observational magnetic field in the photosphere. On the other hand, the latter methods keep the bottom boundary as the observational magnetic field vector in the photosphere. We give priority to keeping the magnetic field measured in the photosphere at the bottom boundary. Therefore, we focus on one method, MHD relaxation method, which is developed by Inoue et al. (2014). As targets to analyze, we chose two active regions, NOAA 11692 and

NOAA 11967 to investigate how significantly different coronal magnetic field structures are derived depending on initial conditions. The examined active regions are two extreme examples; one has rather simple bi-pole magnetic distribution at the photosphere and the other shows a complicated field distribution at the photosphere. The photospheric vertical magnetic field distributions are shown in the left upper and lower panels of Figure 2.1. The detailed observational information will be described in Section 2.2. While the former is composed of bi-pole magnetic fields and shows a weak twist in the photosphere, the latter has multi-pole magnetic fields and shows a strong twist. The global alpha is one of the index values for expressing the degree of the the twist in the active regions. Tiwari et al. (2009a,b) defined global alpha α_g such as,

$$\alpha_g = \frac{\sum(\frac{\partial B_y}{\partial x} - \frac{\partial B_x}{\partial y})B_z}{\sum B_z^2}, \tag{2.1}$$

which can be calculated from the photospheric vector magnetic field, B_x, B_y, and B_z, where z-axis is defined as the vertical direction to the solar surface. A global alpha of NOAA 11692 is $\alpha_g = -1.0 \times 10^{-8}\mathrm{m}^{-1}$ and NOAA 11967 has $\alpha_g = -5.0 \times 10^{-8}\mathrm{m}^{-1}$. Absolute values of α_g in various active regions usually vary from 0 to $5.0 \times 10^{-8}\mathrm{m}^{-1}$ (Pevtsov et al., 1995, 1997). Therefore, the two active regions we analyzed are contrasting examples in terms of the twist.

In the MHD relaxation method, we give an arbitrary 3D magnetic field structure as the initial condition for the modeling and relax it after changing the transverse field to the observed transverse field at the bottom boundary. Usually, the potential field is chosen as the initial condition. In this study, we choose the LFF as the initial condition in addition to the potential field and perform NLFFF extrapolations with different initial conditions, i.e., different constant force-free alpha. We give 5 different initial conditions for NOAA11692 and 12 different initial conditions for NOAA11967 to measure how the obtained result is different from each other.

This chapter is organized as follows: The observations and data reduction are described in Section 2.2. The method of MHD relaxation and numerical settings are described in Section 2.3. Section 2.4 presents the results followed by discussions in Section 2.5. Section 2.6 summarizes the findings in this chapter.

2.2 Observations and Data Reduction

2.2.1 Observations at NOAA 11692

NOAA active region 11692 was a typical active region with a round leading sunspot consisting of an umbra and penumbra. Several opposite polarity magnetic field are broadly distributed at the following area. This active region produced 14 C-class flares and 2 M-class flares between 12 Mar 2013 and 22 Mar 2013. The vector magnetic field map in the upper left of Figure 2.1 was observed with *Hinode*/SOT SP and *SDO*/HMI. The FOV of the SP observation is shown by a green box in Figure 2.1. To increase the narrow FOV of SP when extrapolating the coronal magnetic field by NLFFF modeling, we used the data obtained by the HMI. The gray scale shows the vertical components of the magnetic field to the solar surface and the green arrows show the horizontal magnetic field, which are derived by the inversion of the spectropolarimetric data described in Section 2.2.3. The leading spot has the negative polarity and the positive polarity is dominant at the following region. The negative spot has the anti-clockwise horizontal magnetic field while the strong horizontal magnetic field can not be identified in the positive following region. The SP performs spectropolarimetric observations with two magnetically sensitive Fe I lines at 6301.5 Å and 6302.5 Å with a spectral sampling of 21.5 mÅ per pixel and scanned this region between 03:00 and 03:35 UT on 15 Mar 2013. The map has an effective pixel size of $0''.3$ with the FOV of $166'' \times 123''$. Although the SP provides the polarimetric information based on the slit observations with the high spectral sampling of 21.549 mÅ pix^{-1}, the slit observations limit the field of view (FOV). NOAA 11692 was located around disk center (-161$''$, 257$''$) at the time of the SP scanning. The HMI measures polarization based on the 6 narrow bands (band width: 76 mÅ +/- 10 mÅ) observations around Fe I 6173 Å line. The HMI has an advantage of the regular observation of the full disk of the Sun with the spatial sampling of $0.''5$ pix^{-1}. We also used the HMI data obtained at 03:11 UT on 15 Mar 2013.

To evaluate the validity in the result from the NLFFF extrapolations, we utilized the soft X-ray image observed with the X-ray telescope (XRT: Golub et al., 2007) on board *Hinode*, as shown in the upper right panel of Figure 2.1. The image was observed with Be-thin filter at 03:57 UT on 15 Mar 2013 with a field of view of $395''\times395''$. The pixel sampling is $1.0''$. A sigmoidal structure can be clearly identified in the X-ray image.

2.2.2 Observations at NOAA 11967

NOAA active region 11967 was a flare-productive active region, which produced 10 M-class and 38 C-class flares from 31 January 2014 to 9 February 2014. In the same way as the data for NOAA 11692, we combined a magnetic field map of SP and HMI. We used one of the SP scanned maps obtained at 07:50-08:45 UT on 3 February 2014, as shown in the green box in the lower left panel of Figure 2.1. The gray scale shows the vertical components of the magnetic field to the solar surface and the green arrows show the horizontal magnetic field, which are derived by the inversion of the spectropolarimetric data described in Section 2.2.3. The map has an effective pixel size of $0''.3$ with a field of view (FOV) of $280''\times130''$. NOAA 11967 was located at almost disk center (-100$''$, -100$''$) at the time of the SP scanning. We used the HMI data obtained at 07:47 UT. NOAA 11967 was mainly composed of four magnetic polarities (P1, N1, P2, and N2 in Figure 2.1). While P1 shows round-shape structure, N1, N2, and P2 show the elongated structures. At the polarity inversion line (PIL) between N1 and P2, the sheared horizontal magnetic fields are well visible.

We also used X-ray images obtained with XRT with Be-thin filter at 07:12 UT on 3 February 2014 with a field of view of $512''\times512''$, as shown in the lower right panel of

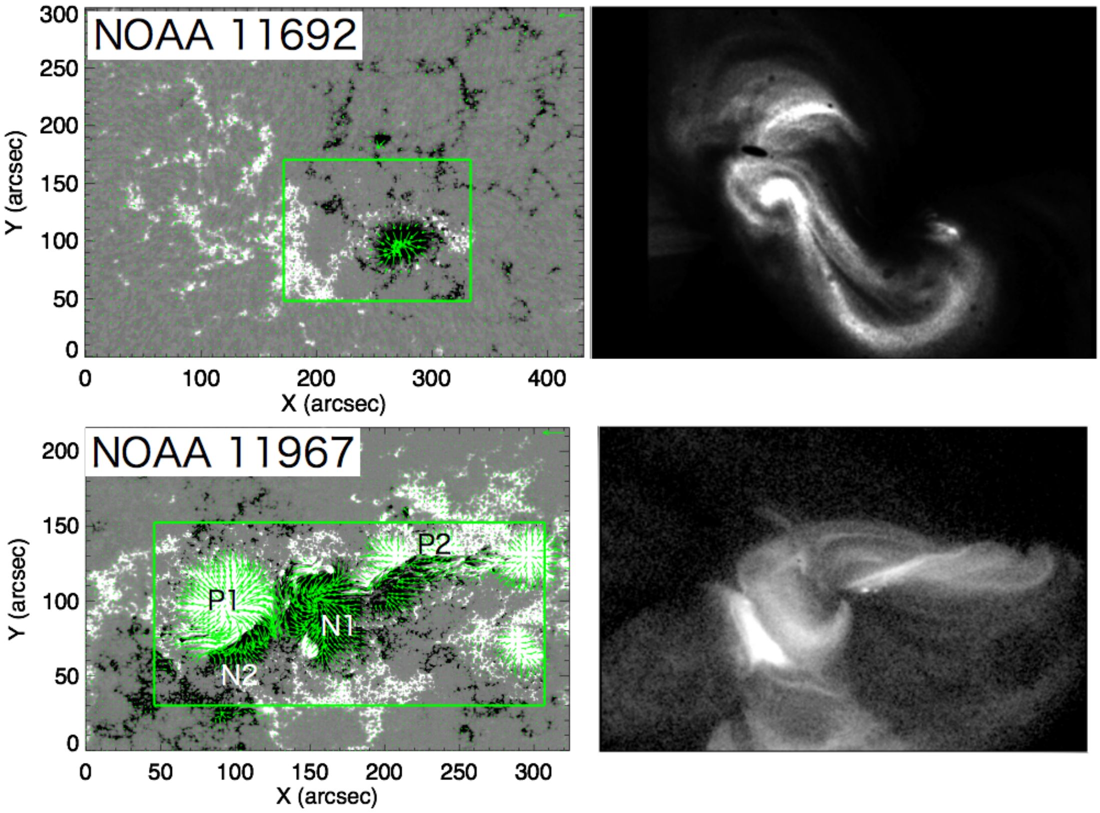

Figure 2.1: Left upper panel: The spatial distribution of the magnetic field vertical to the solar surface in NOAA 11692. *Hinode*/SOT SP and *SDO*/HMI data are combined in this map. The green rectangle shows the FOV of *Hinode*/SOT SP scanned between 03:00 and 03:35 UT on 15 Mar 2013. The green arrows show the horizontal magnetic field. Right upper panel: Soft X-ray image of NOAA 11692 observed with *Hinode*/XRT. Left lower panel: The spatial distribution of the vertical magnetic field in NOAA 11967. *Hinode*/SOT SP and *SDO*/HMI data are combined in this map. The green rectangle shows the FOV of *Hinode*/SOT SP observed at 07:50-08:45 UT on 3 February 2014. The green arrows show the horizontal magnetic field. Right lower panel: Soft X-ray image of NOAA 11967 observed with *Hinode*/XRT

Figure 2.1. Compared to NOAA 11692, NOAA 11967 had a complex structure of coronal loops, because this active region has multiple locations of the both polarities. The sheared magnetic field lines between N1 and P2 also can be seen in the X-ray image.

2.2.3 Data Reduction

For the calibration of the Stokes profiles obtained with *Hinode*/SOT SP, we used the Solarsoft routine SP_PREP (Lites & Ichimoto, 2013) and applied a *Milne-Eddington atmosphere* (ME) model in order to derive the physical parameters by a nonlinear least square fitting using the code based on MELANIE (Socas-Navarro, 2001). SP_PREP corrects the wrap-around of the Stokes I, dark and flat, instrumental polarization, spectral line curvature, thermal drift, and orbital doppler shift. When we derive the magnetic field azimuth, there is well-known ambiguity called 180 degree ambiguity in the LOS reference frame (Landi Degl'Innocenti & Landolfi, 2004). The 180 degree ambiguity in the transverse magnetic field direction was solved with the minimum energy ambiguity resolution method (Metcalf, 1994; Leka et al., 2009).

For the data of HMI, the vector magnetic field data products are provided by the HMI team, which is called Space-weather HMI Active Region Patches (SHARP; Bobra et al., 2014). The HMI data was used to expand the FOV of the 4×4 binned data of SP ($1.2''$/pix) for NOAA 11692 and the 2×2 binned data of SP ($0.6''$/pix) for NOAA 11967. The binning was performed in order to reduce the calculation time of the NLFFF extrapolation. As described in Section 1.4.1, the spatial resolution affect the energy and free energy of NLFFF modelings (DeRosa et al., 2015), because the binning process changes the magnetic energy and free energy at the bottom boundary. In this study, we focus on the dependence of the initial condition on the results of the NLFFF based on the same bottom boundary. Therefore, we perform the NLFFF modeling based on the bottom boundary with single binning factor for each active region ($1.2''$/pix for NOAA 11692 and $0.6''$/pix for NOAA 11967).

2.3 MHD Relaxation Method and Numerical Settings

The nonlinear force-free field extrapolation is performed by the MHD relaxation method (Inoue et al., 2014), which uses the following equations,

$$\frac{\partial \boldsymbol{v}}{\partial t} = -(\boldsymbol{v}\cdot\boldsymbol{\nabla})\boldsymbol{v} + \frac{1}{\rho}\boldsymbol{j}\times\boldsymbol{B} + \nu\nabla^2\boldsymbol{v}, \tag{2.2}$$

$$\frac{\partial \boldsymbol{B}}{\partial t} = \nabla\times(\boldsymbol{v}\times\boldsymbol{B} - \eta\boldsymbol{j}) - \nabla\phi, \tag{2.3}$$

$$\boldsymbol{j} = \nabla\times\boldsymbol{B}, \tag{2.4}$$

$$\frac{\partial \phi}{\partial t} + c_h^2\nabla\cdot\boldsymbol{B} = -\frac{c_h^2}{c_p^2}\phi, \tag{2.5}$$

where ρ is the pseudo density, which is assumed to be equal to $|\boldsymbol{B}|$ to ease the relaxation by equalizing the Alfvén speed in space, ϕ is the convenient potential for $\nabla\cdot\boldsymbol{B}$ cleaning and ν is the viscosity, which is set to a constant (1.0×10^{-3}). The length, magnetic field, velocity, and time were normalized by $L_0 = 157$ Mm for NOAA 11967 and $L_0 = 314$ Mm for NOAA 11692 and $B_0 = 4000$ G, $V_{\rm A} \equiv B_0/(4\pi\rho_0)^{1/2}$, and $\tau_A \equiv L_0/V_A$, where V_A is the Alfvén velocity. Equations (2.2), (2.3), (2.4) and (2.5) are the equation of motion, the induction equation, the $\mathrm{Ampère's}$ law, and $\nabla\cdot\boldsymbol{B}$ cleaning introduced by Dedner et al. (2002), respectively. The parameters c_p^2 and c_h^2 are the advection and diffusion coefficients, respectively and fixed at 0.1 and 0.04. The non-dimensional resistivity η is given by

$$\eta = \eta_0 + \eta_1\frac{|\boldsymbol{j}\times\boldsymbol{B}||\boldsymbol{v}|^2}{|\boldsymbol{B}|^2}, \tag{2.6}$$

where η_0 and η_1 are fixed at 5.0×10^{-5} and 1.0×10^{-3} in non-dimensional units. The second term is introduced to accelerate the relaxation to the force-free state.

The velocity field at each grid was adjusted at each time step below in order to avoid becoming large value. When the value of v^* becomes larger than the value of $v_{\rm max}$,

$$\boldsymbol{v} \rightarrow \frac{v_{\rm max}}{v^*}\boldsymbol{v}, \tag{2.7}$$

where $v^* = |\boldsymbol{v}|/|\boldsymbol{v_A}|$, and $v_{\max} = 0.1$.

In previous NLFFF calculations, the potential field has been used as initial guess for the 3D magnetic field structure. We chose linear force free field as an initial condition including a potential field, which satisfies $\nabla \times \boldsymbol{B} = \alpha_0 \boldsymbol{B}$, where α_0 is a constant. We examined different 5 initial conditions $\alpha_0 = [0, \pm 1.2, \pm 2.3] \times 10^{-8}\mathrm{m}^{-1}$ for NOAA 11692 and 12 initial conditions $\alpha_0 = [0, \pm 0.70, \pm 1.2, \pm 2.3, \pm 4.6, \pm 7.0, -12] \times 10^{-8}\mathrm{m}^{-1}$ for NOAA11967. We used the equations of Alissandrakis (1981) for the calculations of the linear force-free field and the resulting initial conditions are shown in Figures 2.2 and 2.3. Although the case $\alpha_0 = +12 \times 10^{-8}\mathrm{m}^{-1}$ for NOAA 11967 was also calculated, the calculation did not converge. Therefore, we do not include it in the results in this thesis. The numerical domain is set to $(0,0,0) < (x,y,z) < (1.0, 0.7, 0.7)$ resolved by $360 \times 252 \times 252$ nodes for NOAA11692 and $(0,0,0) < (x,y,z) < (1.5, 1.0, 0.5)$ resolved by $540 \times 360 \times 180$ nodes for NOAA 11967. In order to set the same top boundary for all calculations, the initial conditions above $z = 0.417$ are set to the potential field.

The magnetic field at the top was fixed with the initial state (potential field) and the normal component of the magnetic field on the bottom boundary was also fixed. The side boundary was periodic. We varied the transverse component on the bottom boundary $\boldsymbol{B}_{\mathrm{BC}}$ as follows,

$$\boldsymbol{B}_{\mathrm{BC}} = \gamma \boldsymbol{B}_{\mathrm{obs}} + (1-\gamma)\boldsymbol{B}_{\mathrm{intial}}, \tag{2.8}$$

where $\boldsymbol{B}_{\mathrm{obs}}$ and $\boldsymbol{B}_{\mathrm{initial}}$ are the transverse component of the observational and initial bottom boundary, respectively. We increased $\gamma = \gamma + d\gamma$ when $\int |\boldsymbol{j} \times \boldsymbol{B}|^2 dV$ dropped below a critical value. In this study we set $d\gamma = 0.1$. When γ becomes equal to 1, $\boldsymbol{B}_{BC}$ is consistent with the observed field. The number of calculation steps were set to 24000 steps for NOAA 11692 and 25000 steps for NOAA 11967

Spatial derivatives are calculated by the second-order central differences and temporal derivatives are integrated by the Runge-Kutta-Gill method to fourth order accuracy.

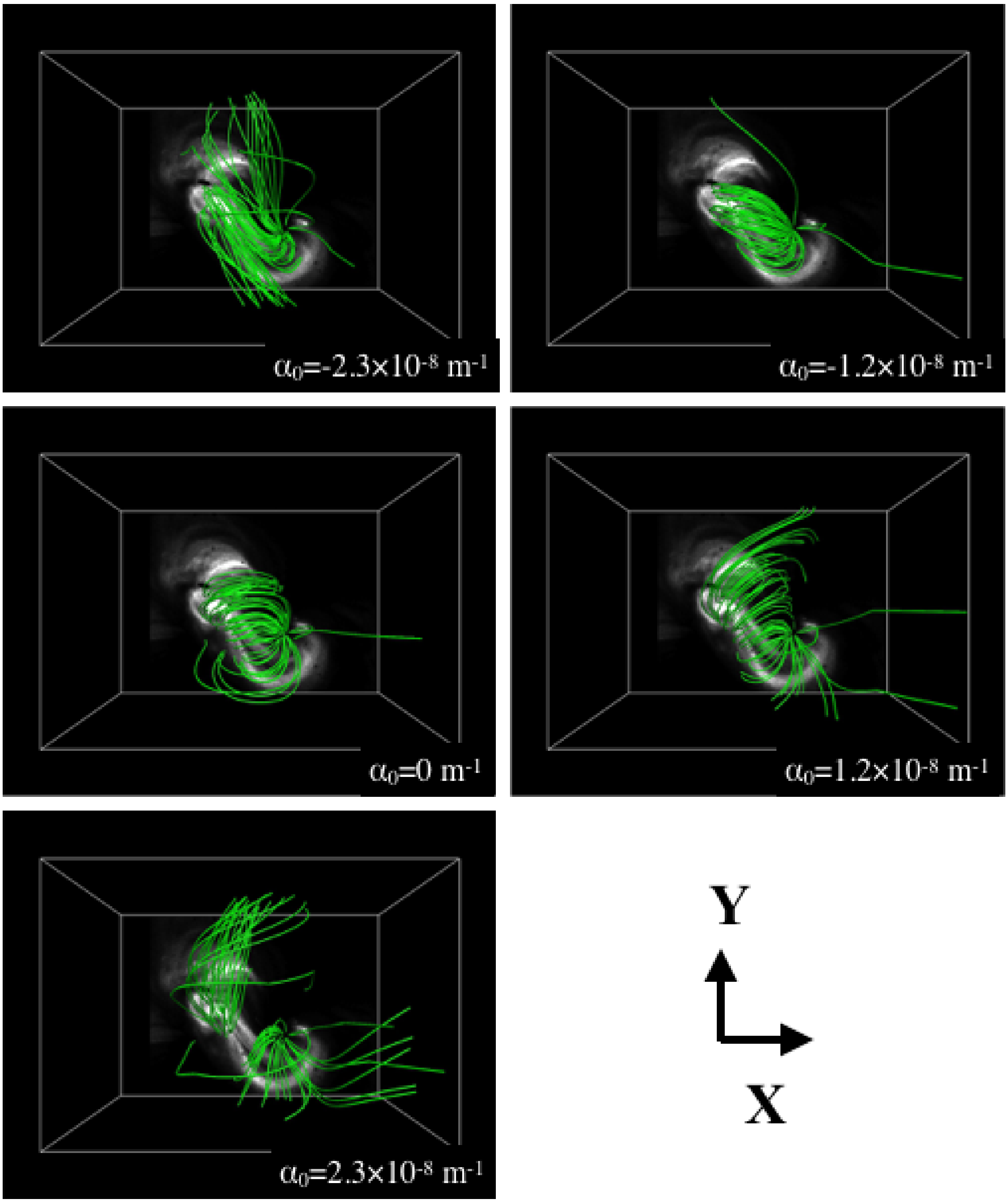

Figure 2.2: The morphology of magnetic field lines (green solid lines) in NOAA 11692 at the initial condition for the NLFFF extrapolation. The background grayscale image is soft X-ray images observed with *Hinode*/XRT.

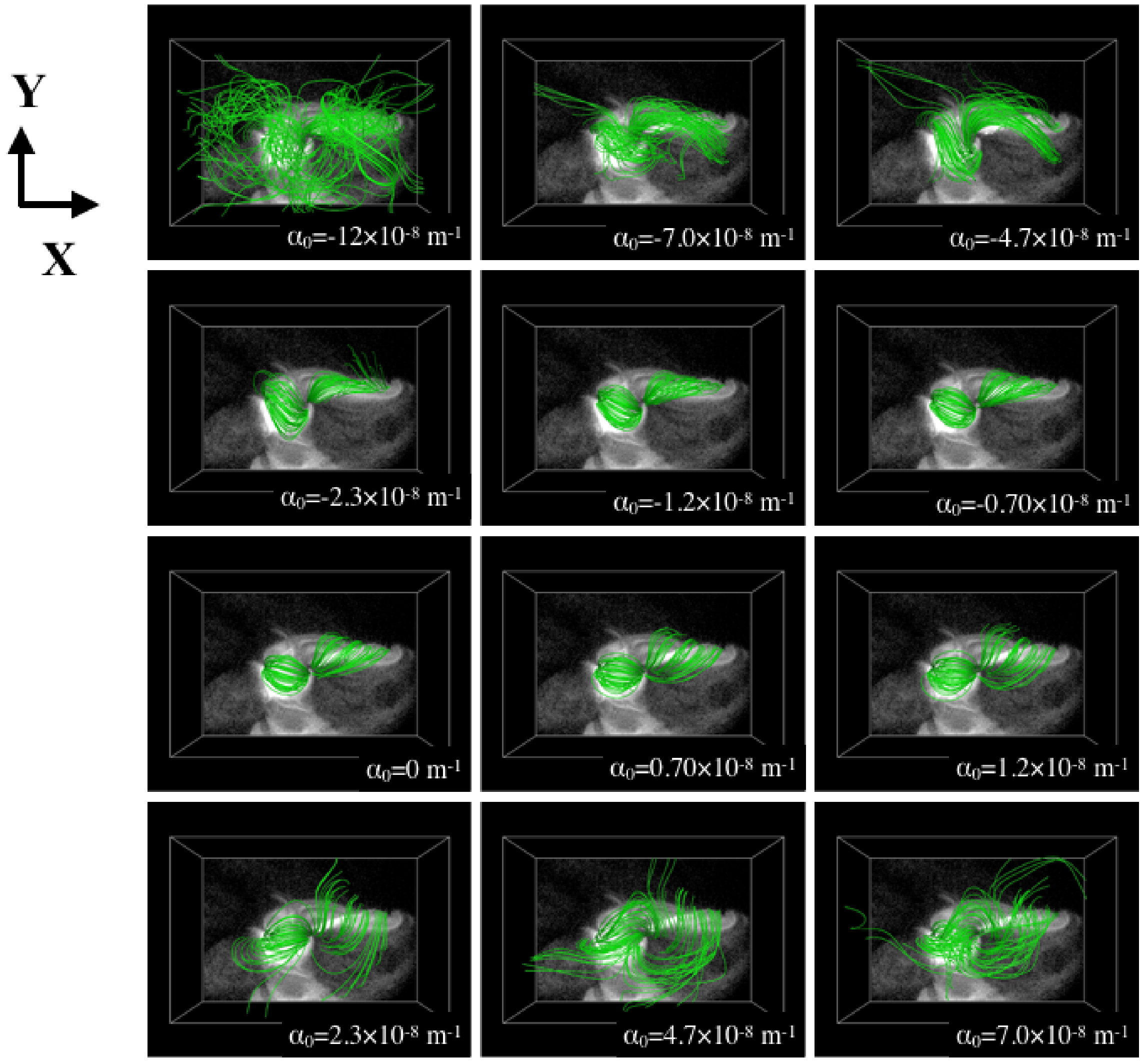

Figure 2.3: The morphology of magnetic field lines (green solid lines) in NOAA 11967 at the initial condition for the NLFFF extrapolation.The background grayscale image is soft X-ray images observed with *Hinode*/XRT.

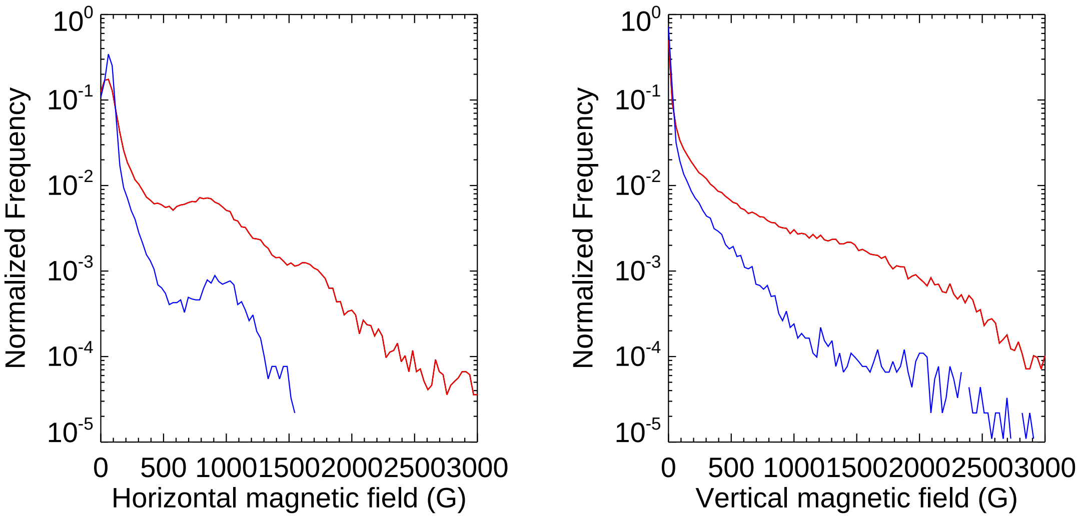

Figure 2.4: The histogram of the horizontal magnetic field (left panel) and vertical magnetic field (right panel) for NOAA 11692 (blue solid line) and NOAA 11967 (red solid line)

2.4 Results

2.4.1 Properties of the Active Regions

In this Section, the property of two active regions in the photosphere are summarized. Figure 2.4 shows the histogram of the horizontal magnetic field (left panel) and vertical magnetic field (right panel) for NOAA 11692 (blue solid line) and NOAA 11967 (red solid line). For both horizontal and vector magnetic field, NOAA 11967 has larger frequency at larger magnetic field. While 6.3 $\%$ of the horizontal magnetic field in the FOV is larger than 1000 G for NOAA 11967, 0.49 $\%$ is larger than 1000 G for NOAA 11692. Regarding the vertical magnetic field, the ratios of $B_z > 1000$G are 7.5 $\%$ and 0.47 $\%$ for NOAA 11967 and NOAA 11692, respectively. The vertical magnetic flux of NOAA 11967 is 8.4×10^{22} Mx, which is 2.3 times larger than that of NOAA 11692, 3.7×10^{22} Mx.

The force-freeness of the active regions from Equations (1.16), (1.17), and (1.18) are listed in Table 2.1. The values of $|F_x|/F_p$, $|F_y|/F_p$, and $|F_z|/F_p$ of NOAA 11967 are sufficiently small, i.e., the active region satisfies the necessary condition of the force-free field. On the other hand , the absolute value of the force-freeness of NOAA 11692 is slightly larger than 0.1 in $|F_y|/F_p$ and $|F_z|/F_p$. However, this value is not so large and not far from 0.1 compared to other active regions reported in the previous studies (Metcalf et al., 1995; Moon et al., 2002; Liu et al., 2013). Therefore, the two active region NOAA 11692 and NOAA 11967 are comparatively appropriate regions applying to the assumption of the force-free modeling.

Table 2.1: Force-freeness of the active regions derived from Eqns (1.16), (1.17), and (1.18)

	NOAA 11692	NOAA 11967
$\|F_x\|/F_p$	0.053	0.029
$\|F_y\|/F_p$	0.128	0.0089
$\|F_z\|/F_p$	0.17	0.089

2.4.2 Morphology of Field Lines from NLFFF

Figure 2.5 shows the magnetic field lines (green solid lines) in NOAA 11692 as a result of the NLFFF extrapolation with 5 different initial conditions. The magnetic field lines are chosen randomly around the region where the sigmoidal structure is identified. Back ground gray scale images are X-ray images observed with the XRT. As clearly seen, the 3D morphology of the magnetic field lines strongly depends on the initial condition. In other words, the morphology of magnetic field lines from the NLFFF extrapolation is not far from that of the initial condition. When we use the potential field as an initial condition ($\alpha_0 = 0$ case), which is usually chosen, the field lines are potential-like and the sigmoidal structure can not be correctly reproduced. On the other hand, when we choose appropriate initial condition (e.g. $\alpha_0 = -2.3 \times 10^{-8}$ m^{-1} in Figure 2.5), many magnetic field lines from the NLFFF extrapolation are almost parallel to the direction of the sigmoidal structure in the X-ray image. The value $\alpha_0 = -2.3 \times 10^{-8}$ m^{-1} is larger than the global alpha estimated from the photospheric magnetic field, $\alpha_g = -1.0 \times 10^{-8}$ m^{-1}. Figure 2.6 shows a side view of the magnetic field lines. Only the cases of $\alpha_0 = -2.3 \times 10^{-8}$, 0, and 2.3×10^{-8} m^{-1} are shown. The height of the field lines are at around $100 - 200$ Mm. Not only long loop lines whose loop top is located at more than 100 Mm, the short field lines whose loop top is located below 100 Mm are also different among different solutions.

Figure 2.7 shows the magnetic field lines (green solid lines) in NOAA 11967 as a result of the NLFFF extrapolation with 12 different initial conditions. Compared to NOAA 11692, the results are less dependent on the initial condition. When we use large $|\alpha_0|(> 7.0 \times 10^{-8}$ m^{-1}) as an initial condition, the result shows a bit different morphology. The result of $\alpha_0 = -1.2 \times 10^{-8}$ m^{-1} does not seem to converge to the reasonable solution. As shown in Figure 2.8, the height of the field lines is around 30 Mm.

2.4.3 Total Magnetic Energy, Total Free Energy, and Extrapolation Metrics

To evaluate the difference due to the initial condition quantitatively, we focus on the total magnetic energy, total free energy and extrapolation metrics, as shown in Table 2.2 for NOAA 11692 and Table 2.3 for NOAA 11967. The first column shows the constant force-free alpha α_0, which is used for the initial condition of the NLFFF extrapolation. The second, third and fourth columns show the magnetic energy of the initial condition $E_{\rm init}$, the magnetic energy of the NLFFF E, and the free magnetic energy $E_{\rm free}$. The third and fourth columns are normalized by the magnetic energy of the potential field $E_{\rm pot}$. For NOAA 11692, when we choose the potential field as an initial condition, the resulting magnetic energy of the NLFFF becomes almost potential. As larger the magnetic energy of the initial condition, the resulting magnetic energy of the NLFFF becomes larger. However the magnitude of the difference of $E/E_{\rm pot}$ among the different initial condition is not so large compared to that of $E_{\rm init}$. The ratios of maximum total magnetic

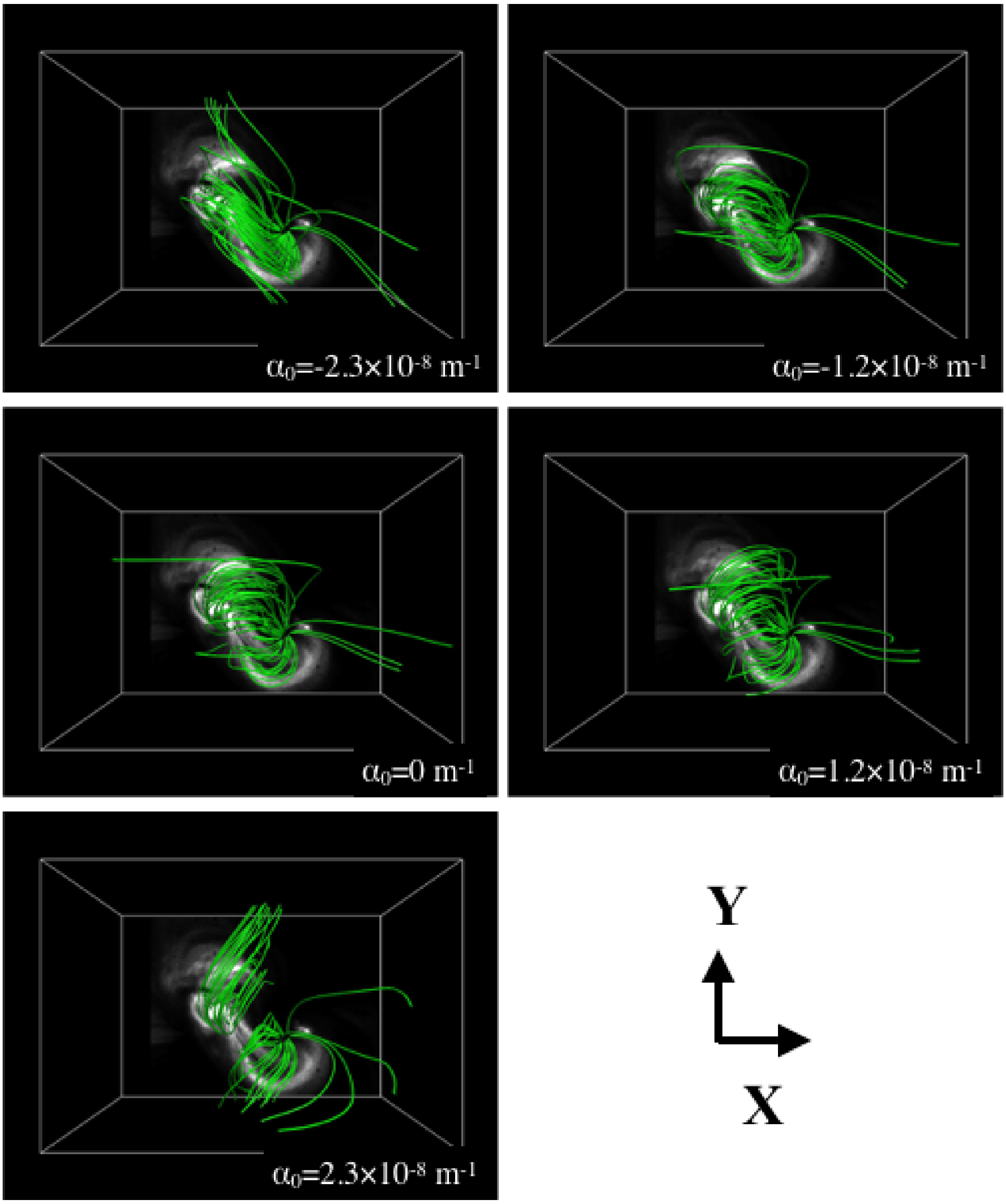

Figure 2.5: The morphology of magnetic field lines (green solid lines) in NOAA 11692 as a result of the NLFFF extrapolation. The background grayscale image is soft X-ray images observed with *Hinode*/XRT.

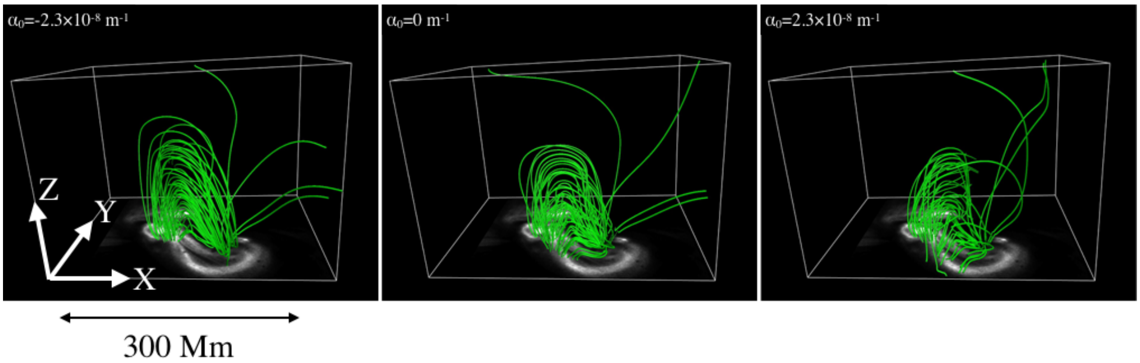

Figure 2.6: A side view of the magnetic field lines in NOAA 11692, obtained by the NLFFF extrapolation with three initial conditions. The background grayscale image projected on the bottom surface are a soft X-ray image observed with *Hinode*/XRT.

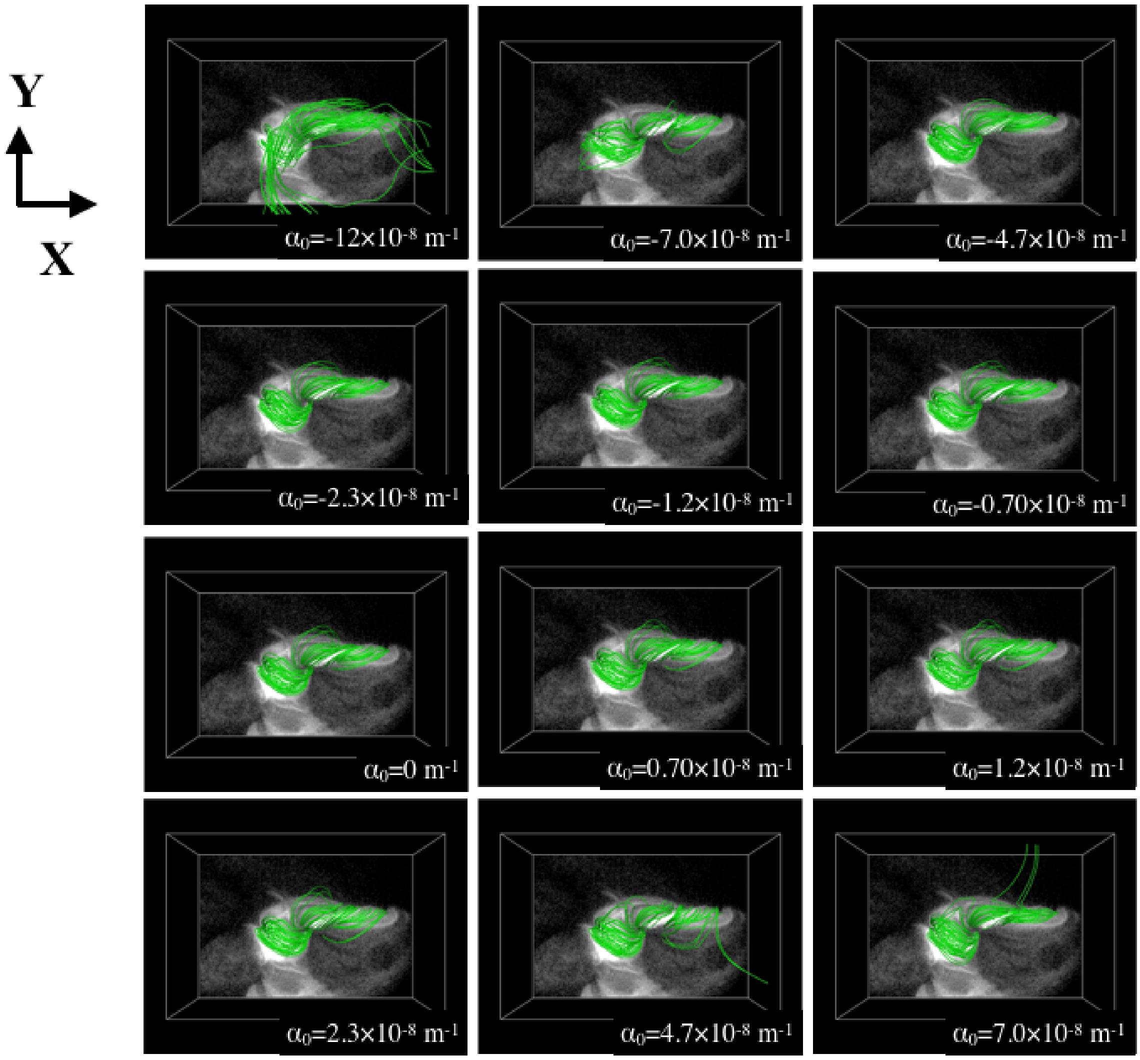

Figure 2.7: The morphology of magnetic field lines (green solid lines) in NOAA 11967 as a result of the NLFFF calculation. The background grayscale image is a soft X-ray image observed with *Hinode*/XRT.

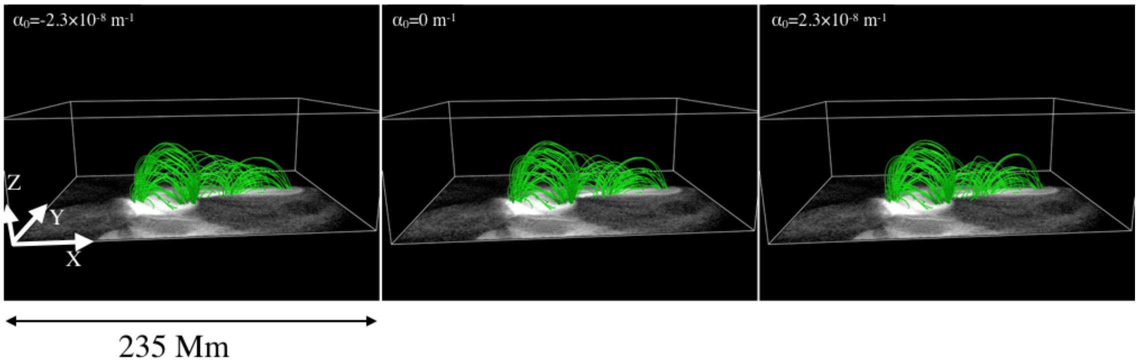

Figure 2.8: A side view of the magnetic field lines in NOAA 11967, obtained by the NLFFF extrapolation with three initial conditions. The background grayscale image projected on the bottom surface are a soft X-ray image observed with *Hinode*/XRT.

energy and free energy (-2.3×10^{-8} m^{-1}) to minimum ones ($\alpha_0 = 0$ m^{-1}) are 1.08 and 2.64, respectively. NOAA 11967 has larger magnetic energy and free energy than NOAA 11692 does as shown in Tables 2.2 and 2.3. As mentioned in Section 2.4.2, the result from $\alpha_0 = -12 \times 10^{-8}$ m^{-1} does not seem to be physically reasonable. Therefore we focus on the results except $\alpha_0 = -12 \times 10^{-8}$ m^{-1} for NOAA 11967. Even when we choose the potential field as an initial condition, the resulting NLFFF has $E_{\text{free}}/E_{\text{pot}} = 0.14$. The notable result for NOAA 11967 is in spite of the large initial constant α_0 such as $|\alpha_0| > 2.3 \times 10^{-8}$ m^{-1}, the resulting magnetic field energy and free energy do not show large difference among the different initial conditions. The ratios of maximum total magnetic energy and free energy ($\alpha_0 = -7.0 \times 10^{-8}$ m^{-1}) to minimum ones (0 m^{-1}) are 1.03 and 1.28, respectively.

The fifth column shows $\langle \mathrm{CW} \sin\theta \rangle$, the mean sine of the angle θ between $\boldsymbol{j}$ and $\boldsymbol{B}$ weighted by $\boldsymbol{j}$, which is defined as follows,

$$\langle \mathrm{CW} \sin\theta \rangle = \frac{\sum |\boldsymbol{j} \sin\theta|}{\sum |\boldsymbol{j}|}. \tag{2.9}$$

The metric is based on the property of the force-free field that the electric current is parallel to the magnetic field. Therefore $\langle \mathrm{CW} \sin\theta \rangle$ represents how force-free an obtained NLFFF solution is. When the solution is close to the force-free state, $\langle \mathrm{CW} \sin\theta \rangle$ is close to zero. For NOAA 11692, the $\langle \mathrm{CW} \sin\theta \rangle$ has the smallest value when $\alpha_0 = -2.3 \times 10^{-8}$ m^{-1}, while it has the largest value when $\alpha_0 = 0\,\mathrm{m}^{-1}$. For NOAA 11967, the magnitude of $\langle \mathrm{CW} \sin\theta \rangle$ is larger than that of NOAA 11692. Similar to NOAA 11692, the $\langle \mathrm{CW} \sin\theta \rangle$ tends to have smaller value when the $|\alpha_0|$ becomes larger.

The sixth column shows the fractional flux ratio $\langle |f_i| \rangle$

$$
\begin{aligned}
f_i &= \frac{\int_{\Delta S} \boldsymbol{B} \cdot d\boldsymbol{S}}{\int_{\Delta S} |\boldsymbol{B}| dS} \\
&= \frac{(\nabla \cdot \boldsymbol{B}) \times (\Delta x)^3}{|\boldsymbol{B}| \times 6(\Delta x)^2} \\
&= \frac{(\boldsymbol{\nabla} \cdot \boldsymbol{B}) \Delta x}{6|\boldsymbol{B}|},
\end{aligned} \tag{2.10}
$$

where ΔS and Δx are the small discrete surface and the grid spacing. From Equation 1.10, the divergence of the magnetic field must vanish in the calculation box. The $\langle |f_i| \rangle$ represents how divergence-free an obtained NLFFF solution is. When the condition of $\boldsymbol{\nabla} \cdot \boldsymbol{B} \ll 0$ is satisfied in the results of the NLFFF extrapolation, the $\langle |f_i| \rangle$ becomes close to zero. For NOAA 11692, the $\langle |f_i| \rangle$ has the smallest value, when the initial condition is $\alpha_0 = -2.3 \times 10^{-8}$ m^{-1}. As shown in Section 2.4.2, the field lines of the NLFFF from $\alpha_0 = -2.3 \times 10^{-8}$ m^{-1} are almost parallel to the direction of the sigmoidal structure in the X-ray image. On the other hand, for NOAA 11967, while the morphology of the field lines are not so different among the NLFFF results, each solution has the different $\langle |f_i| \rangle$ value. The $\langle |f_i| \rangle$ has the smallest value, when the initial condition is $\alpha_0 = 1.2 \times 10^{-8}$ m^{-1} and tends to have large value when the $|\alpha_0|$ is large.

Table 2.2: NLFFF metrics for NOAA 11692

Initial α_0 [10^{-8} m^{-1}]	E_{init} [10^{32} erg]	E/E_{pot}	$E_{\mathrm{free}}/E_{\mathrm{pot}}$	$\langle$CWsin$\theta\rangle$	$\langle\lvert f_i\rvert\rangle[\times 10^{-5}]$
-2.3	8.12	1.14	0.14	0.38	5.58
-1.2	6.46	1.06	0.06	0.54	7.36
0 (potential)	6.27	1.05	0.05	0.58	7.90
1.2	6.54	1.06	0.06	0.57	8.09
2.3	8.39	1.14	0.14	0.39	6.35

First column: The constant force-free alpha α_0 used for the initial condition of the NLFFF extrapolation. Second column:The magnetic energy of the initial condition E_{init}. Third column:the magnetic energy of the NLFFF E. Fourth column: The free magnetic energy E_{free}. Fifth Column: The mean sine of the angle θ between $\boldsymbol{j}$ and $\boldsymbol{B}$ weighted by $\boldsymbol{j}$, which represents force-freeness of the NLFFF extrapolation. Sixth Column: The fractional flux ratio, which represents the divergence-freeness of the NLFFF extrapolation.

Table 2.3: NLFFF metrics for NOAA 11967

Initial α_0 [10^{-8} m^{-1}]	$E_{\rm init}$ [10^{33} erg]	$E/E_{\rm pot}$	$E_{\rm free}/E_{\rm pot}$	$\langle$CWsin$\theta\rangle$	$\langle\|f_i\|\rangle$[$\times10^{-5}$]
-12	20.0	1.31	0.31	0.19	8.26
-7.0	7.17	1.18	0.18	0.23	7.60
-4.7	4.41	1.16	0.16	0.25	5.82
-2.3	3.20	1.14	0.14	0.25	7.42
-1.2	3.05	1.14	0.14	0.26	5.66
-0.70	3.03	1.14	0.14	0.27	5.16
0 (potential)	3.02	1.14	0.14	0.27	4.50
0.70	3.03	1.14	0.14	0.27	4.07
1.2	3.06	1.14	0.14	0.27	3.97
2.3	3.22	1.14	0.14	0.27	5.07
4.7	4.38	1.15	0.15	0.26	5.89
7.0	7.19	1.17	0.17	0.24	6.16

The definition of each column is the same as Table 2.3.

2.4.4 Comparison of Solutions at Each Height

Figure 2.9 shows the global alpha derived at each height from the NLFFF results. The global alpha was calculated by Equation (2.1). Different color shows the results from different initial condition. For both NOAA 11692 and NOAA 11967, the global alpha shows larger deviation among the calculations at the higher layer than at the lower. For NOAA 11692, the global alpha is -1.0×10^{-8} m^{-1} at the photospheric height and depending on the initial condition, the global alpha deviates to the positive and negative values as the height increases. For NOAA 11967, the global alpha is -5.0×10^{-8} m^{-1} at the photospheric height. Independent of the initial condition, the global alpha increases as the height increases and beyond 20 Mm, the global alpha starts to show the deviation

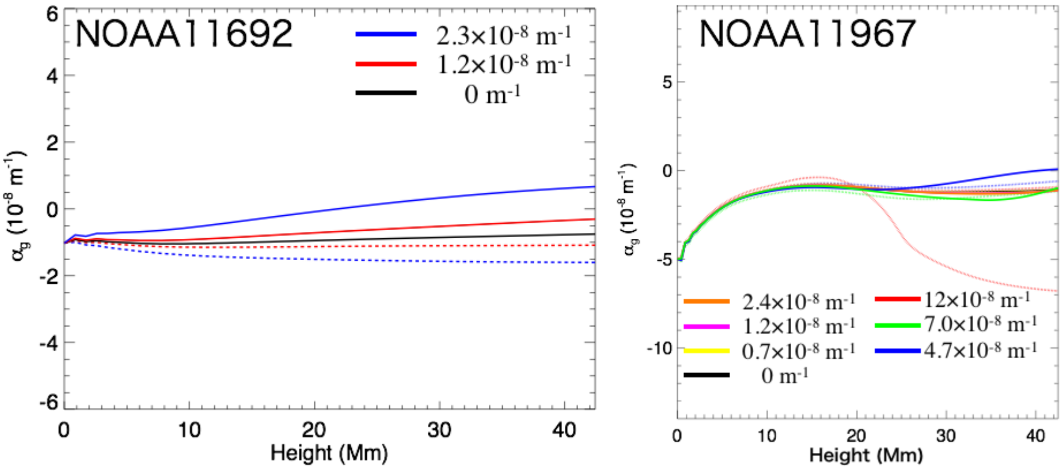

Figure 2.9: Height variation of global alpha. Each color shows each initial condition and solid (dotted) lines show positive (negative) α_0.

depending on the initial condition.

The spatial distributions of vector magnetic field in NOAA 11692 at 2.6 Mm and 26 Mm height are shown in Figures 2.10 and 2.11. The grayscale color shows the vertical magnetic field and green arrows show the horizontal magnetic field. The horizontal magnetic field in the negative spot is less dependent on the initial condition at 2.6 Mm. In the region between positive and negative polarities, however, the horizontal magnetic field is a bit different between results from the different initial conditions. This tendency can be clearly seen at the higher height as shown in Figure 2.11. The horizontal magnetic field around the polarity inversion line in case of $\alpha_0 = 2.3 \times 10^{-8}\ \mathrm{m}^{-1}$ is completely different from that in case of $\alpha_0 = -2.3 \times 10^{-8}\ \mathrm{m}^{-1}$. On the other hand, the vertical magnetic field distribution shows the simple two polarity configuration and is similar to each other. Figure 2.12 shows the number density distribution in vector magnetic field with different initial condition for NOAA 11692 at the height of 2.6 Mm and 26 Mm. The result with $\alpha_0 = 0\ \mathrm{m}^{-1}$ is compared with that with $\alpha_0 = -2.3 \times 10^{-8}\ \mathrm{m}^{-1}$. As seen in the difference between Figures 2.10 and 2.11, the dispersion is larger in 26 Mm compared to in 2.6 Mm. While the correlation coefficients, C are 0.96 and 0.95 for B_x and B_y at 2.6 Mm, respectively, those at 26 Mm are 0.82 and 0.60, respectively. The dispersion also can be seen at

2.6 Mm in the regions with small magnetic field (~ 100G). In the number density distribution of B_y, some pixels have large B_y in $\alpha_0 = -2.3 \times 10^{-8}$ m^{-1}, while have small B_y in $\alpha_0 = 0$ m^{-1} This distribution reflects the horizontal magnetic field distribution around the polarity inversion line, as described above.

The spatial distributions of vector magnetic field in NOAA 11967 at 2.6 Mm and 26 Mm height are shown in Figures 2.13 and 2.14. The grayscale color shows the vertical magnetic field and green arrows show the horizontal magnetic field. The spatial distribution of vector magnetic field is quite similar at 2.6 Mm among NLFFF results from different initial conditions. At 26 Mm, there exist difference not only in horizontal magnetic field but also in vertical magnetic field. Figure 2.15 shows the number density distribution in vector magnetic field of NOAA 11967 with different initial condition at the height of 2.6 Mm and 26 Mm. The result of $\alpha_0 = 0$ m^{-1} is compared to that with $\alpha_0 = -2.3 \times 10^{-8}$ m^{-1}. At the 2.6 Mm height, the vector magnetic field shows strong correlation even though the initial condition is quite different. The correlation coefficients,C are 0.99, 0.99, and 1.00 for B_x, B_y, and B_z, respectively, at 2.6 Mm These coefficients of NOAA 11967 are larger than those of NOAA 11692. Similar to NOAA 11692, the small deviation can be seen in the weak magnetic field (< 200 G) region. At 26 Mm, the number density distributions do not show strong correlation, suggesting that the NLFFF results are affected by the initial condition, although the correlation coefficients are larger than those of NOAA 11692.

2.4.5 Convergence in Each Calculation

The volume integral of the Lorentz force must vanish in the force-free condition. However, it does not strictly vanish in numerical NLFFF computations. Non-zero Lorentz force may be caused by the non-force-freeness at the bottom boundary and the inconsistency of the setting of the top boundary and side boundary. For the reasons mentioned above, the Lorenz force often appears near the boundary of the calculation box. There-

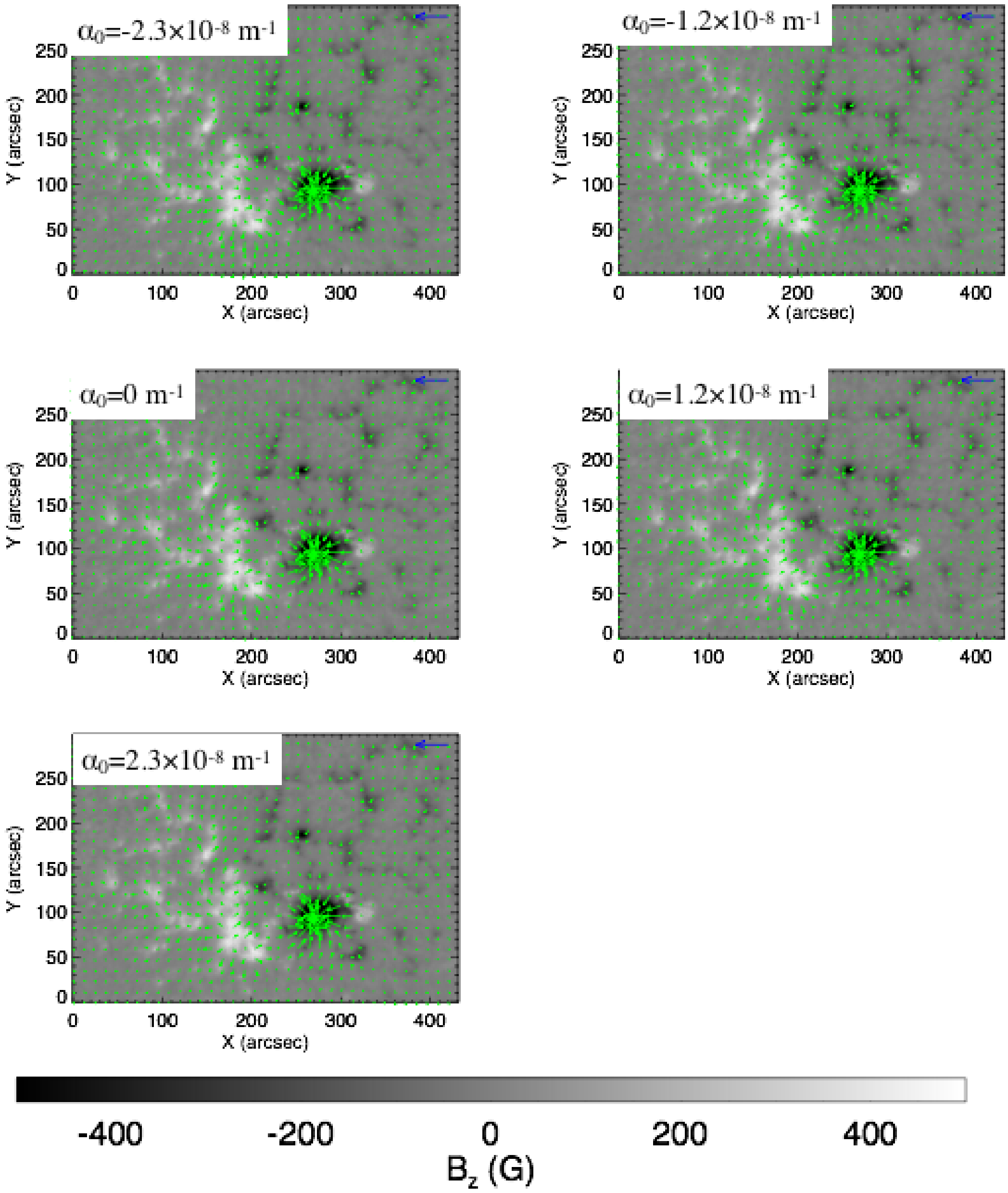

Figure 2.10: The spatial distributions of vector magnetic field for each solution in NOAA 11692 at 2.6 Mm height. The grayscale color shows the vertical magnetic field and green arrows show the horizontal magnetic field. The length of the blue arrow shows the field strength of 1000 G.

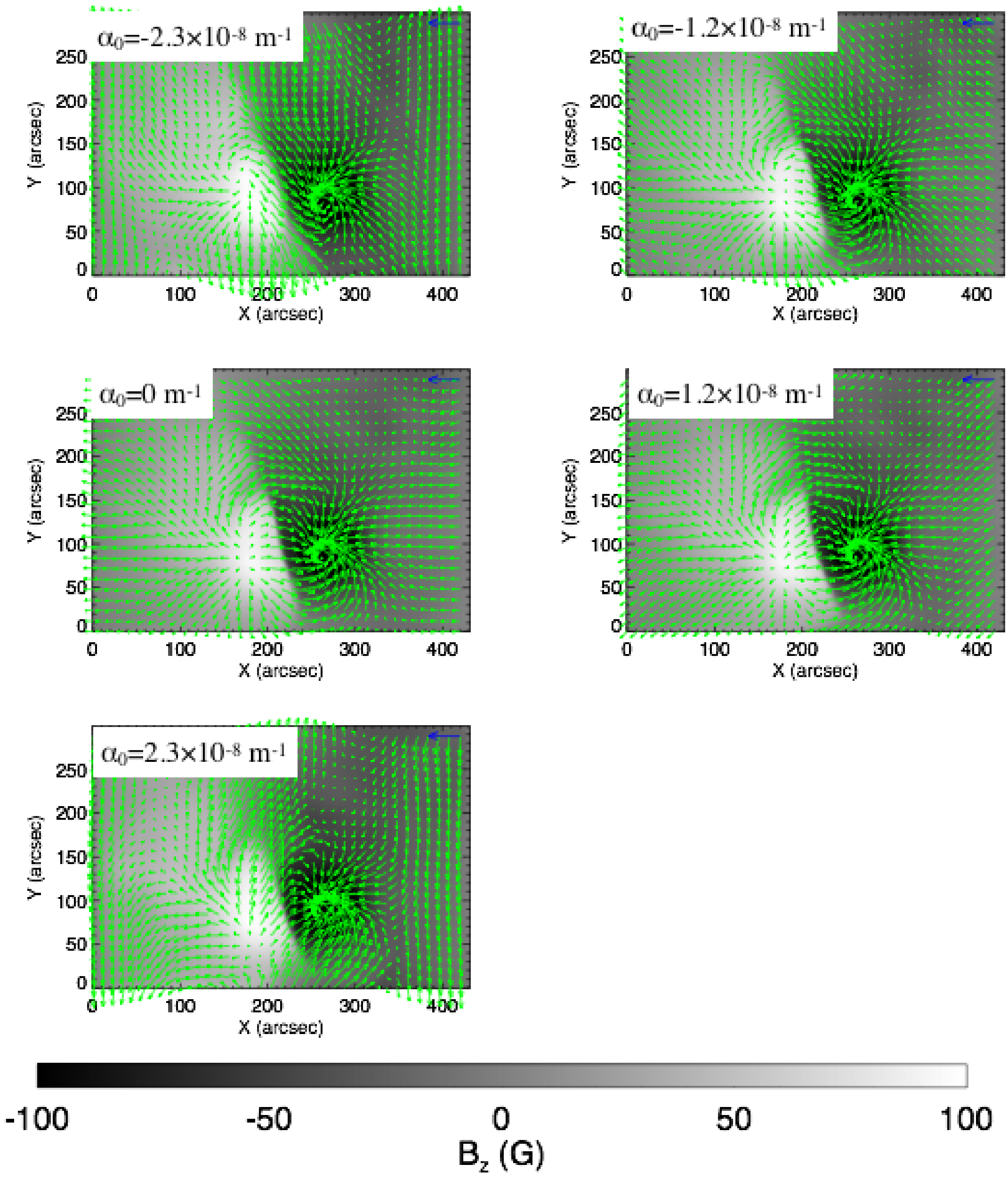

Figure 2.11: Similar as Figure 2.10, but at 26 Mm. The length of the blue arrow shows the field strength of 200 G.

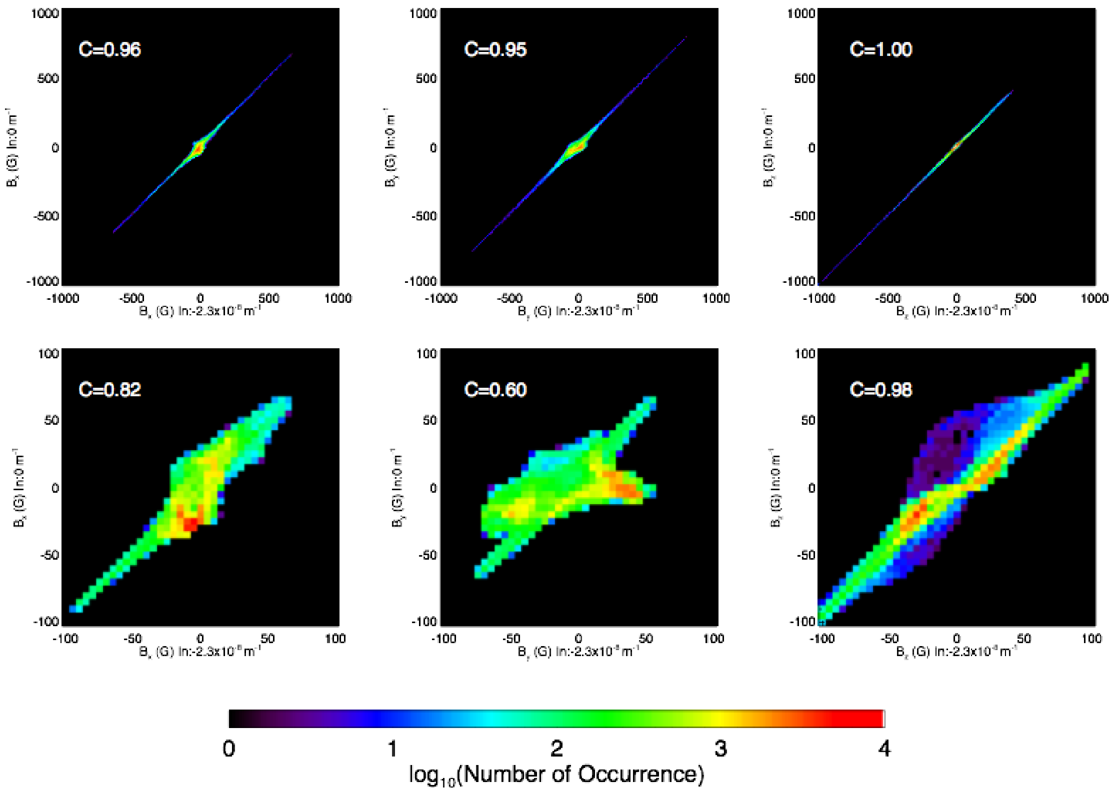

Figure 2.12: All panels show the number density distribution in vector magnetic field from different initial conditions at 2.6 Mm (upper) and 26 Mm (lower) height. Comparisons between $\alpha_0 = 0\ \mathrm{m}^{-1}$ and $\alpha_0 = -2.3 \times 10^{-8}\ \mathrm{m}^{-1}$ in NOAA 11692.

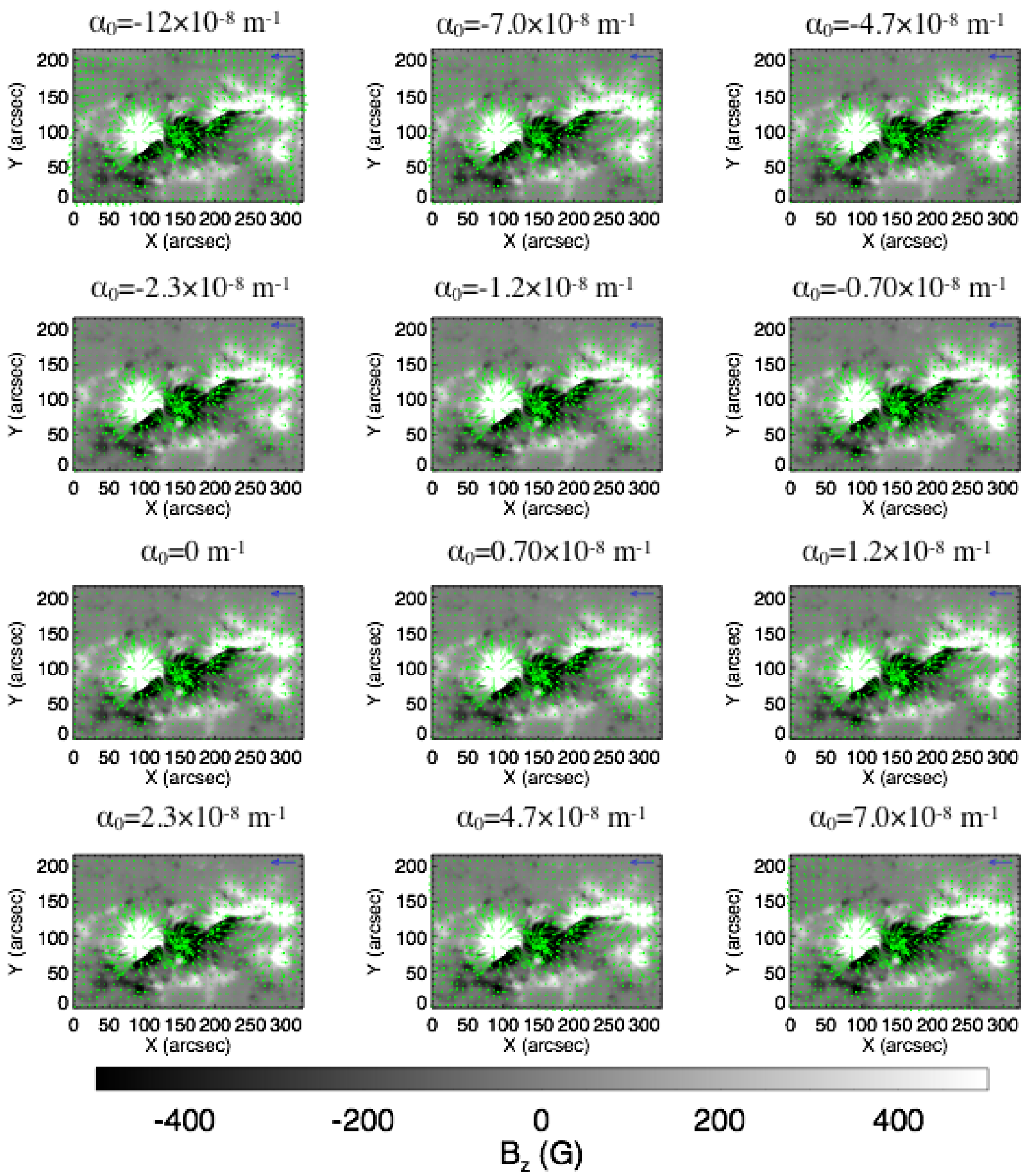

Figure 2.13: Similar as Figure 2.10, the spatial distributions of vector magnetic field for each solution in NOAA 11967 at 2.6 Mm height. The length of the blue arrow shows the field strength of 1500 G.

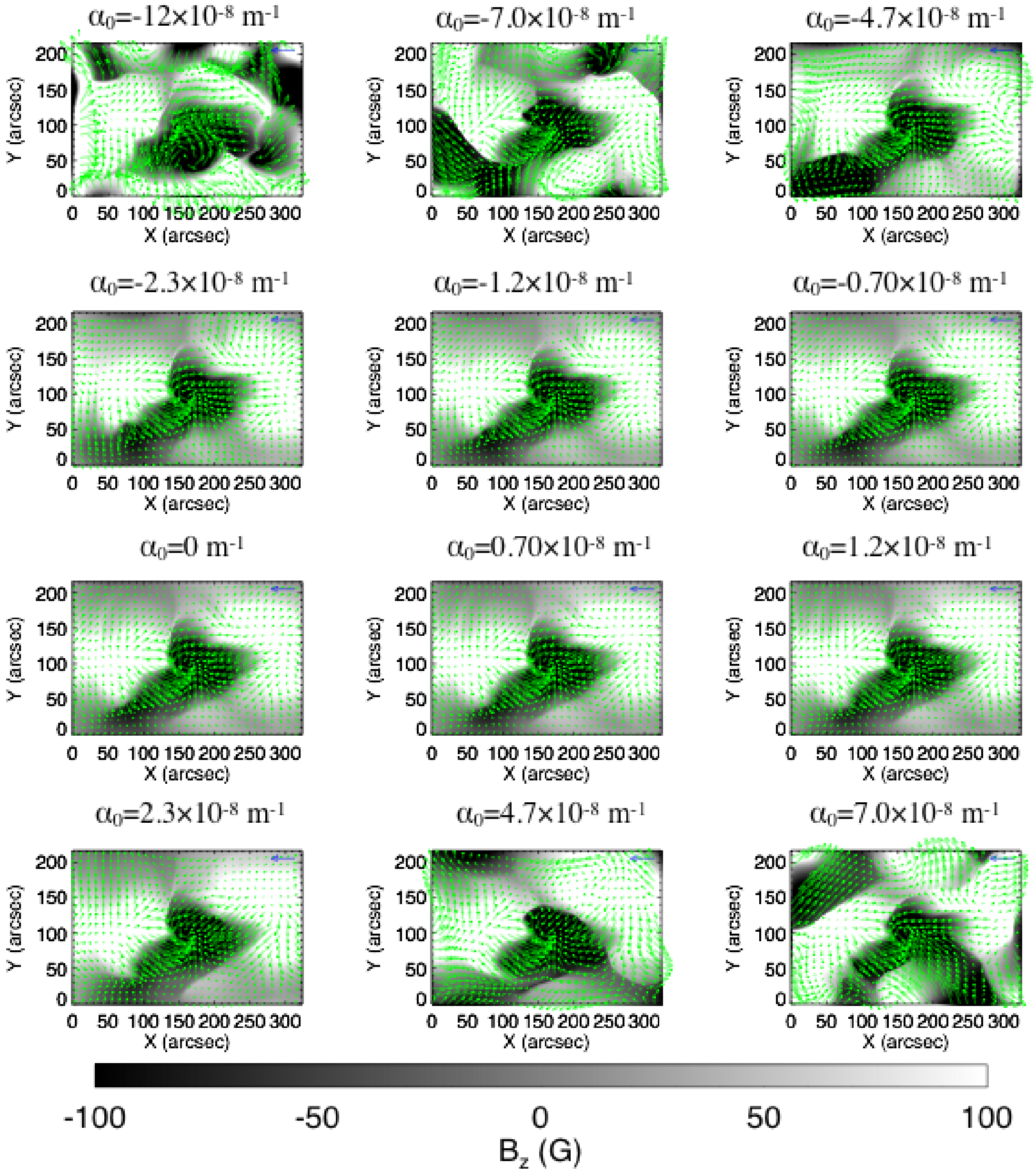

Figure 2.14: Similar as Figure 2.13, but at 26 Mm. The length of the blue arrow shows the field strength of 300 G.

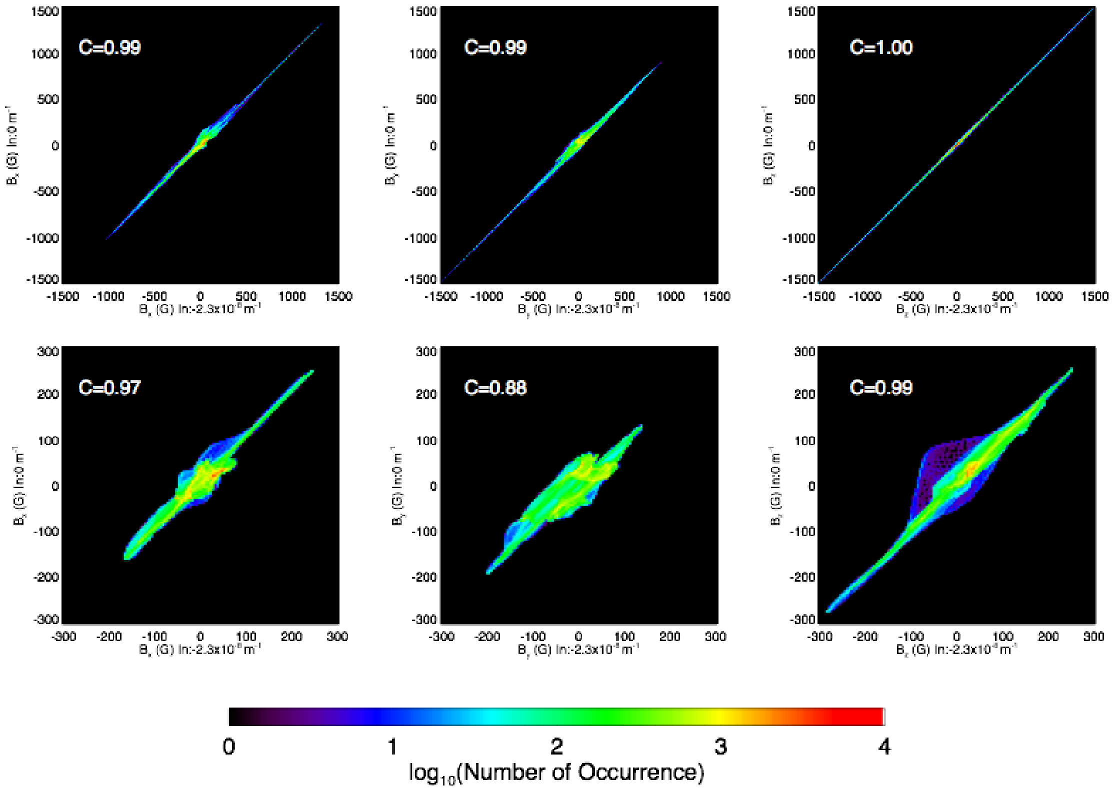

Figure 2.15: All panels show the number density distribution in vector magnetic field from different initial conditions at 2.6 km (upper) and 26 Mm (lower) height. Comparison between $\alpha_0 = 0\ \mathrm{m}^{-1}$ and $\alpha_0 = -2.3 \times 10^{-8}\ \mathrm{m}^{-1}$ in NOAA 11967.

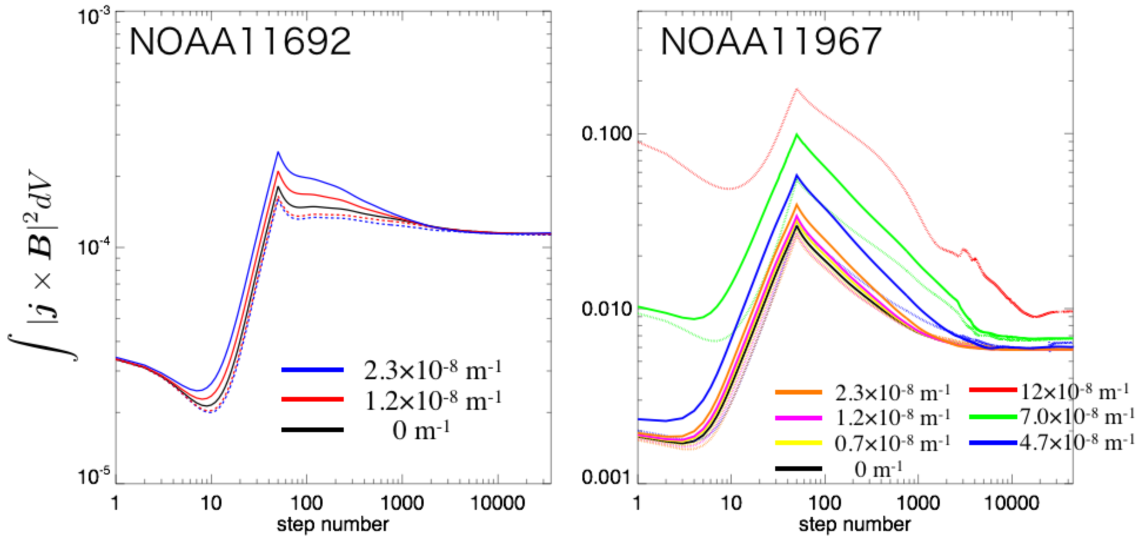

Figure 2.16: The volume integral of the Lorenz force at each time step. Each color of the lines shows the initial absolute value of the constant force-free alpha. Solid lines correspond to the initial positive force-free alpha and dotted lines correspond to negative one.

fore, we usually stop the relaxation process when the volume integral of the Lorentz force converges to a certain value. Figure 2.16 shows the evolution of the volume integral of the Lorenz force as a function of time step. The Lorentz force is normalized by the values described in Section 2.3. Each color of the lines shows the initial absolute value of the constant force-free alpha. Solid lines correspond to the initial negative force-free alpha, whereas dotted lines correspond to positive one. The Lorentz force increases between 10 and 100 step number because the electric current is transported from the bottom boundary according to Equation 2.8. For both active regions, the convergence speed becomes faster for negative value in comparison with the opposite value in the same absolute α_0. For NOAA 11692, the volume integral of the Lorentz force converges to a similar value for all initial conditions. For NOAA 11967, when the absolute value of initial constant alpha has a smaller value, e.g., black, yellow, purple, orange, and blue lines in Figure 2.16, the volume integral of the Lorentz force tends to smaller at the same time step compared to the large initial force-free alpha, e.g., green and red lines.

Although the volume integral of the Lorentz force looks converging, there is a possibility that the magnetic field has not yet converged at the higher region because the Lorentz force may be mostly concentrated at the lower height in the calculation box. We investigate the height distribution of the Lorentz force. The panels (a) and (c) of Figure 2.17 shows the height distribution of the Lorentz force for NOAA 11692, which is averaged at each height for $\alpha_0 = 0 \ \mathrm{m}^{-1}$ and $\alpha_0 = -2.3 \times 10^{-8} \ \mathrm{m}^{-1}$, respectively. This is the result at 24000 step. As expected, the Lorentz force is mainly concentrated at the lower height for both solution. The panels (b) and (d) of Figure 2.17 show the Lorentz force, which is normalized by the square of the magnetic field strength and is averaged at each height for (a) $\alpha_0 = 0 \ \mathrm{m}^{-1}$ and (b) $\alpha_0 = -2.3 \times 10^{-8} \ \mathrm{m}^{-1}$. For both $\alpha_0 = 0 \ \mathrm{m}^{-1}$ and $\alpha_0 = -2.3 \times 10^{-8} \ \mathrm{m}^{-1}$, the normalized Lorentz force is also mainly concentrated at the lower height. Below 10 Mm, the normalized Lorentz force is of the order of 10-100, while above 10 Mm, the normalized Lorentz force is of the order of 1-10. The panels (e) and (f) show the difference of the height distribution of Lorentz force between (a) and (c), and (b) and (d), respectively. Red asterisks show (a)>(c) or (b) $>$(d), while blue asterisks show (c)>(a) or (d) $>$(b). The difference of the Lorentz force is around 10^{-4}. The Lorentz force of $\alpha_0 = -2.3 \times 10^{-8} \ \mathrm{m}^{-1}$ is larger above 20 Mm. At most of the height, the normalized Lorentz force of $\alpha_0 = -2.3 \times 10^{-8} \ \mathrm{m}^{-1}$ is smaller than that of $\alpha_0 = 0 \ \mathrm{m}^{-1}$. Although the difference of the normalized Lorentz force is larger at the lower height, the ratio to the normalized Lorentz force is smaller compared to the higher region. At the lower height, the difference of the normalized Lorentz force is of order of 0.1-1, while the normalized Lorentz force is of order of 10-100. The ratio of the difference is 1% at the lower height. On the other hand, at the higher region, the difference of the normalized Lorentz force is of order of 0.1, while the normalized Lorentz force is of order of 1. The ratio of the difference is 10% at the higher region. The panels (g) and (f) show the height distribution of the absolute value of the force-free alpha, which is averaged at each height for $\alpha_0 = 0 \ \mathrm{m}^{-1}$ and $\alpha_0 = -2.3 \times 10^{-8} \ \mathrm{m}^{-1}$, respectively. Note that the force-free alpha and the normalized Lorentz force have the same unit. The force-free alpha shows similar distribution with the Lorentz force. At the lower height, the force-free alpha is of order of 10-100, while at the higher region, the force-free alpha is of order 1-10. The force-free alpha is smaller than the normalized Lorentz force at the lower height, while larger at the higher region. This result indicates that the normalized Lorentz force is sufficiently small at the higher region, while at the lower height, there exists the significant normalized Lorentz force.

The panels (a) and (c) of Figure 2.18 show the Lorentz force and the normalized Lorentz force distribution at 2600 km height for NOAA 11692 for $\alpha_0 = 0 \mathrm{~m}^{-1}$ (left) and $\alpha_0 = -2.3 \times 10^{-8} \mathrm{~m}^{-1}$ (right). The panels (b) and (d) show the Lorentz force and the normalized Lorentz force distribution at 26 Mm height for NOAA 11692 for $\alpha_0 = 0 \mathrm{~m}^{-1}$ (left) and $\alpha_0 = -2.3 \times 10^{-8} \mathrm{~m}^{-1}$ (right). At 2600 km height, the strong Lorentz force is concentrated around the negative sunspot because the strong magnetic field is concentrated. The normalized Lorentz force is small in the strong magnetic field region such as negative spot umbra, while the normalized Lorentz force is large in the spot penumbra and weak magnetic field region. At 2600 km height, there are little difference between the distribution of $\alpha_0 = 0 \mathrm{~m}^{-1}$ and $\alpha_0 = -2.3 \times 10^{-8} \mathrm{~m}^{-1}$. At 26 Mm height, the distribution of the Lorentz force and the normalized Lorentz force are similar. This indicates that the magnetic field is more uniformly distributed at the higher region. The Lorentz force is concentrated in the polarity inversion line. At 26 Mm, the Lorentz force shows a slight different distribution between $\alpha_0 = 0 \mathrm{~m}^{-1}$ and $\alpha_0 = -2.3 \times 10^{-8} \mathrm{~m}^{-1}$. The NLFFF of $\alpha_0 = 0 \mathrm{~m}^{-1}$ has the stronger Lorentz force in the polarity inversion line compared to that of $\alpha_0 = 0 \mathrm{~m}^{-1}$.

The panels (a) and (b) of Figure 2.19 show the height distribution of the Lorentz force and the normalized Lorentz force for NOAA 11692, which is averaged at each height. These are the results of $\alpha_0 = 0 \mathrm{~m}^{-1}$. Colors show each time step at 20 (black),100 (yellow), 500 (red), 900 (green), 24000 (blue), and 60000 (orange) step, respectively. The panels (c) and (d) show the temporal variation of the height distribution of the Lorentz force and the normalized Lorentz force. Colors show the time interval between 20 and 100 step (yellow), 100 and 500 step (red), 500 and 900 step (green), 900 and 24000 step (blue),

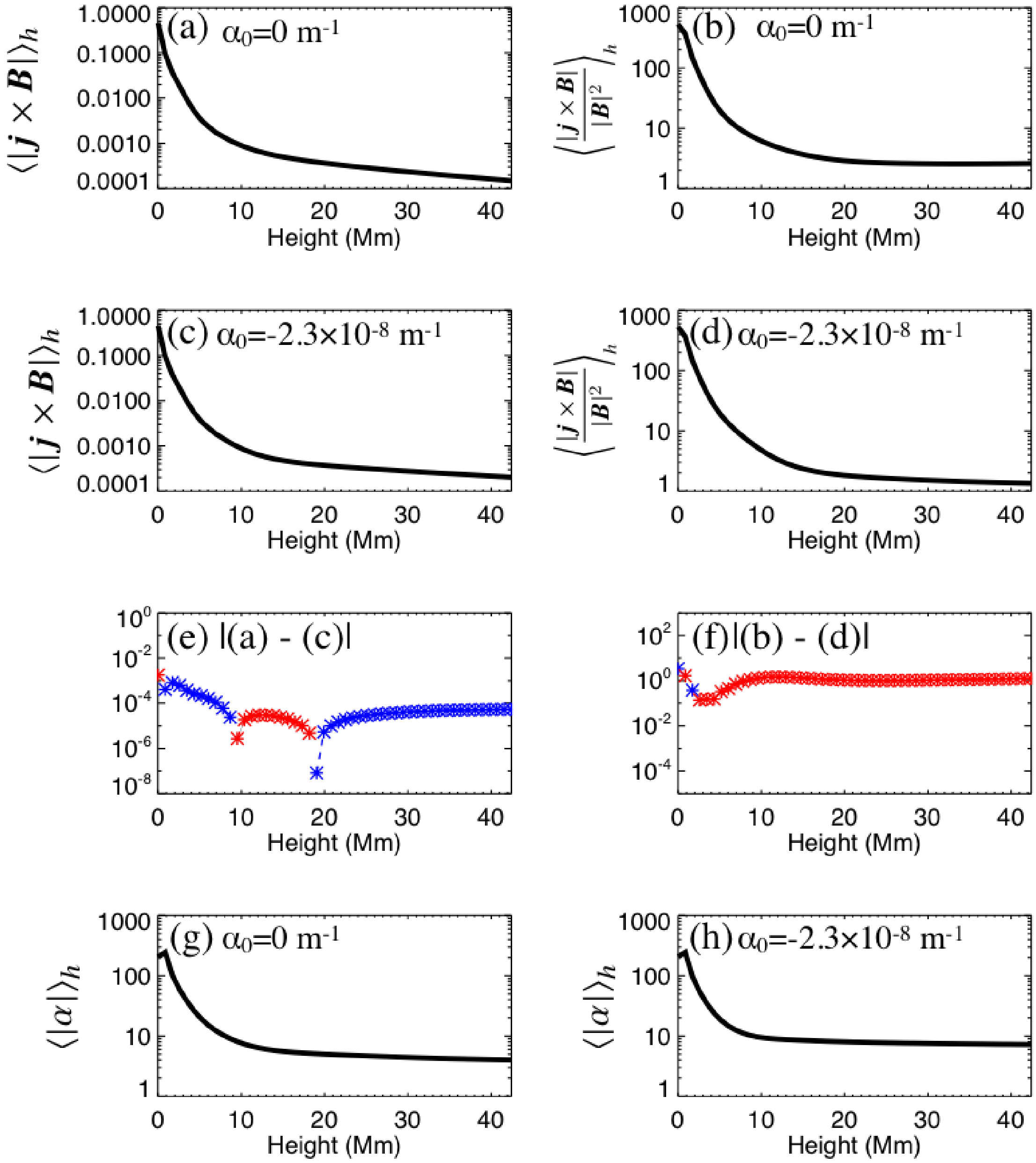

Figure 2.17: (a) and (c): The height distribution of the Lorentz force for NOAA 11692, which is averaged at each height for $\alpha_0 = 0\,\mathrm{m}^{-1}$ and $\alpha_0 = -2.3\times10^{-8}\,\mathrm{m}^{-1}$, respectively. This result is at 24000 step. (b) and (d): The height distribution of the normalized Lorentz force. (e) and (f): The difference of the height distribution of the Lorentz force and the normalized Lorentz force between (a) and (c), and (b) and (d), respectively. Red asterisks show (a)>(c) or (b)>(d), while blue asterisks show (c)>(a) or (d)>(b). (g) and (h): The height distribution of the absolute value of the force-free alpha, which is averaged at each height for $\alpha_0 = 0\ \mathrm{m}^{-1}$ and $\alpha_0 = -2.3 \times 10^{-8}\ \mathrm{m}^{-1}$, respectively.

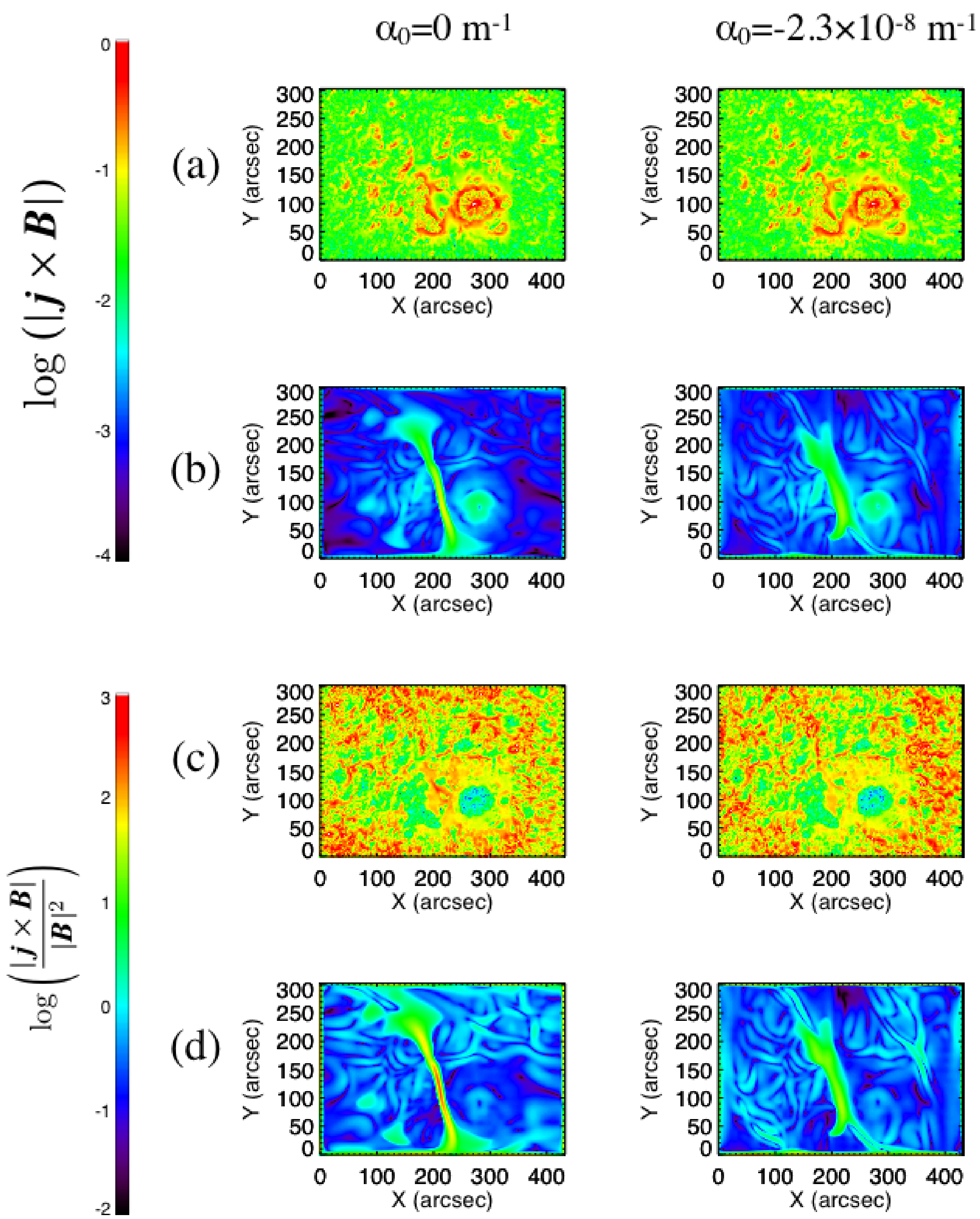

Figure 2.18: (a) and (c): The Lorentz force and the normalized Lorentz force distribution at 2600 km height for NOAA 11692 for $\alpha_0 = 0\ \mathrm{m}^{-1}$ (left) and $\alpha_0 = -2.3 \times 10^{-8}\ \mathrm{m}^{-1}$ (right), respectively. (b) and (d): The Lorentz force and the normalized Lorentz force distribution at 26 Mm height for NOAA 11692 for $\alpha_0 = 0\ \mathrm{m}^{-1}$ (left) and $\alpha_0 = -2.3 \times 10^{-8}\ \mathrm{m}^{-1}$ (right), respectively.

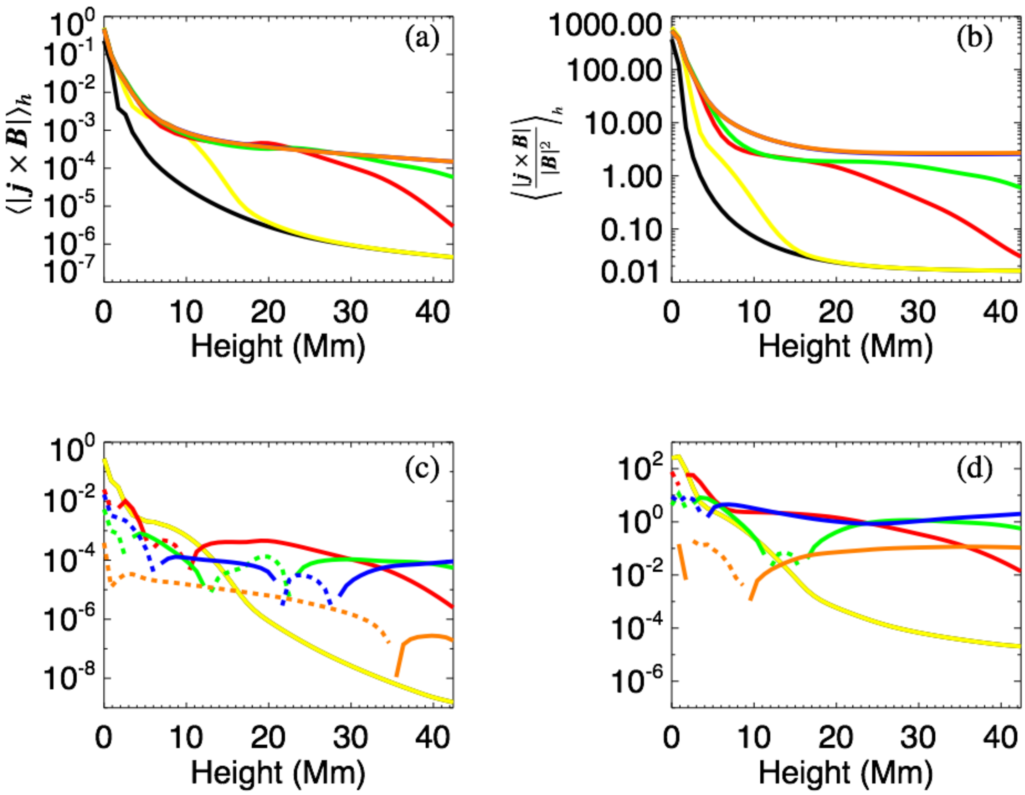

Figure 2.19: (a) and (b):Solid lines show the height distribution of the Lorentz force and the normalized Lorentz force for NOAA 11692, which is averaged at each height, respectively. This is the result of $\alpha_0 = 0\ \mathrm{m}^{-1}$. Colors show each time step at 20 (black),100 (yellow), 500 (red), 900 (green), 24000 (blue), and 60000 (orange) step, respectively. (c) and (d): The temporal variation of the height distribution of the Lorentz force and the normalized Lorentz force. Colors show the time interval between 20 and 100 step (yellow), 100 and 500 step (red), 500 and 900 step (green), 900 and 24000 step (blue), and 24000 and 60000 step (orange), respectively. Solid lines show the increase, while the dashed lines show the decrease.

and 24000 and 60000 step (orange), respectively. Solid lines show the increase, while the dashed lines show the decrease. Both the Lorentz force and the normalized Lorentz force show the similar behavior. As clearly seen, the Lorentz force and the normalized Lorentz force are transported from the lower height to the higher region with increasing the calculation step. Between the step of 24000 (blue) and 60000 (orange), the Lorentz force and the normalized Lorentz force show little change, which means that the magnetic field does not change significantly during this steps.

Figure 2.20 shows the temporal evolution of the normalized Lorentz force distribution

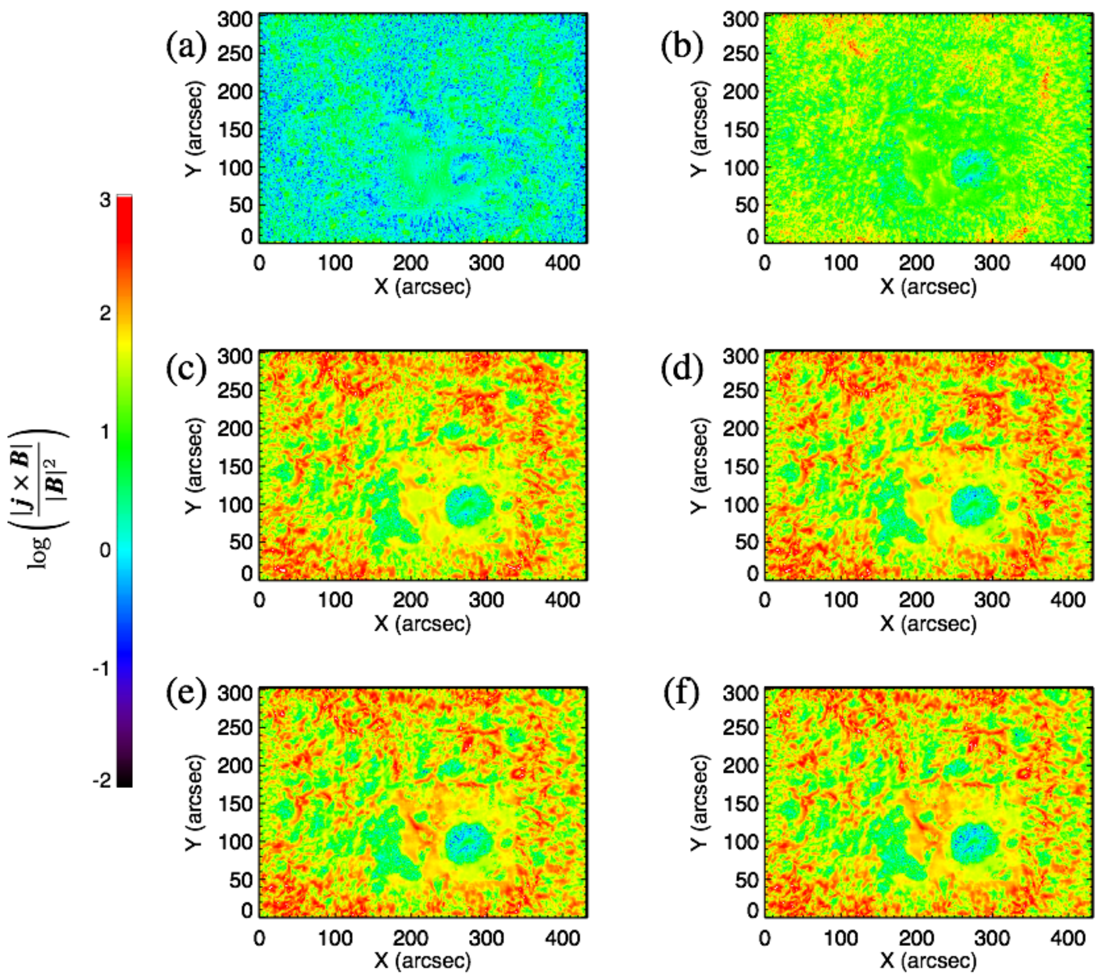

Figure 2.20: The temporal evolution of the normalized Lorentz force distribution at 2600 km for NOAA 11692. This is the normalized Lorentz force of $\alpha_0 = 0\ \mathrm{m}^{-1}$. Each panel shows each time step at (a) 20 step, (b)100 step, (c) 500 step, (d) 900 step, (e) 24000 step, and (f) 60000 step, respectively.

at 2600 km for NOAA 11692. This is the result of the normalized Lorentz force of $\alpha_0 = 0\ \mathrm{m}^{-1}$. Each panel shows each time step at (a) 20 step, (b)100 step, (c) 500 step, (d) 900 step, (e) 24000 step, and (f) 60000 step, respectively. The normalized Lorentz force at 2600 km increases between 20 and 500 steps, while the distribution of the Lorentz force does not change significantly after 500 steps. This result indicates that the magnetic field at the lower height does not change significantly from early calculation step, although the normalized Lorentz force remains to a certain amount.

Figure 2.21 shows the temporal evolution of the normalized Lorentz force distribution

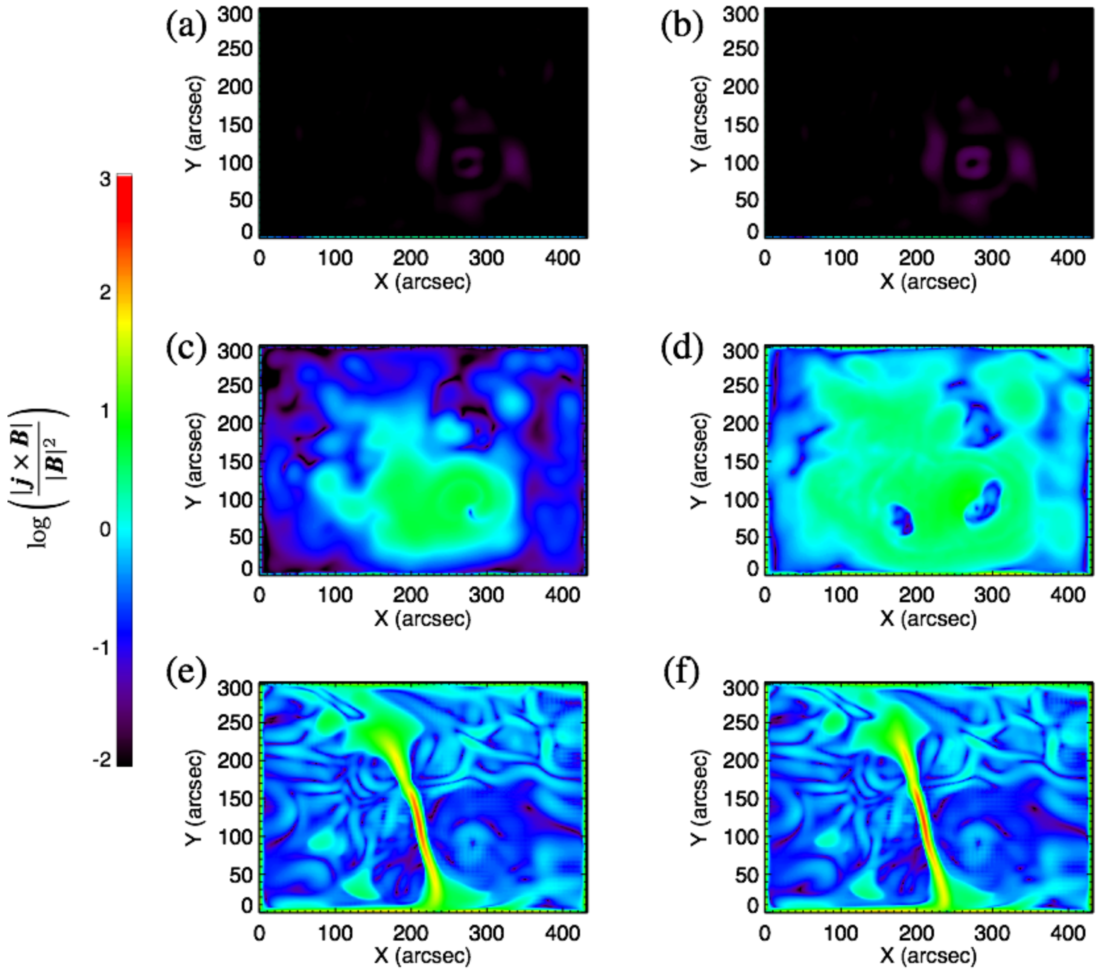

Figure 2.21: The temporal evolution of the normalized Lorentz force distribution at 26 Mm for NOAA 11692. Each panel shows each time step at (a) 20 step, (b)100 step, (c) 500 step, (d) 900 step, (e) 24000 step, and (f) 60000 step, respectively.

at 26 Mm for NOAA 11692. Each panel shows each time step at (a) 20 step, (b)100 step, (c) 500 step, (d) 900 step, (e) 24000 step, and (f) 60000 step, respectively. At the time step of 20 step and 100 step, there is little normalized Lorentz force because the normalized Lorentz force has not been transported from the bottom boundary as seen in Figure 2.19. After 500 step, the normalized Lorentz force increases at 26 Mm and the distribution of the normalized Lorentz force does not change significantly after 24000 step.

Figures 2.22, 2.23, 2.24, 2.25, and 2.26 show the results of the analysis of the Lorentz force for NOAA 11967 in the same way with NOAA 11692. The results are similar as those of NOAA 11692.

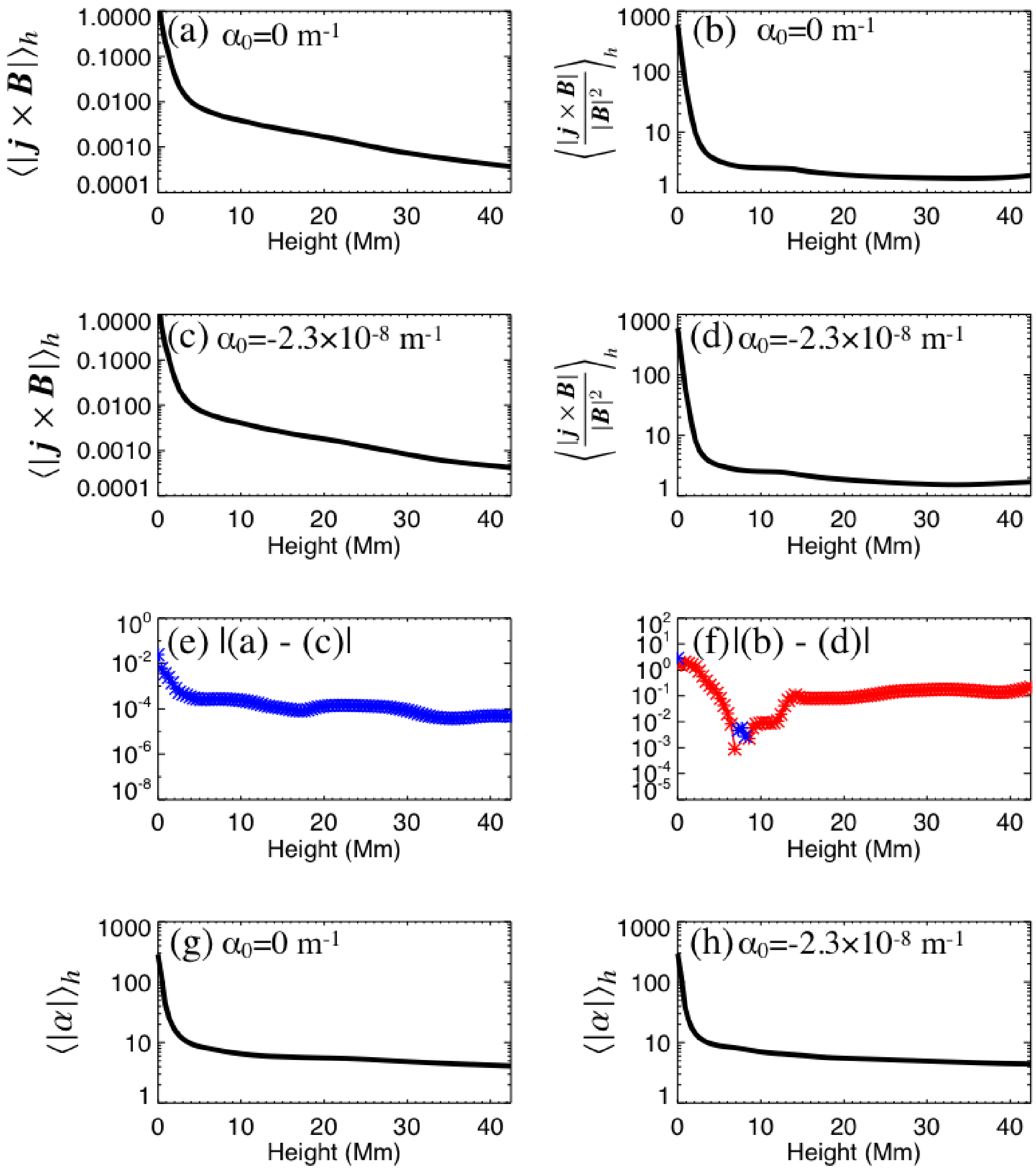

Figure 2.22: (a) and (c): The height distribution of the Lorentz force for NOAA 11967, which is averaged at each height for $\alpha_0 = 0\ \mathrm{m}^{-1}$ and $\alpha_0 = -2.3 \times 10^{-8}\ \mathrm{m}^{-1}$. This is the result at 25000 step. (b) and (d): The height distribution of the normalized Lorentz force. (e) and (f): The difference of the height distribution of the Lorentz force and the normalized Lorentz force between (a) and (c), and (b) and (d), respectively. Red asterisks show (a)>(c) or (b)>(d), while blue asterisks show (c)>(a) or (d)>(b).

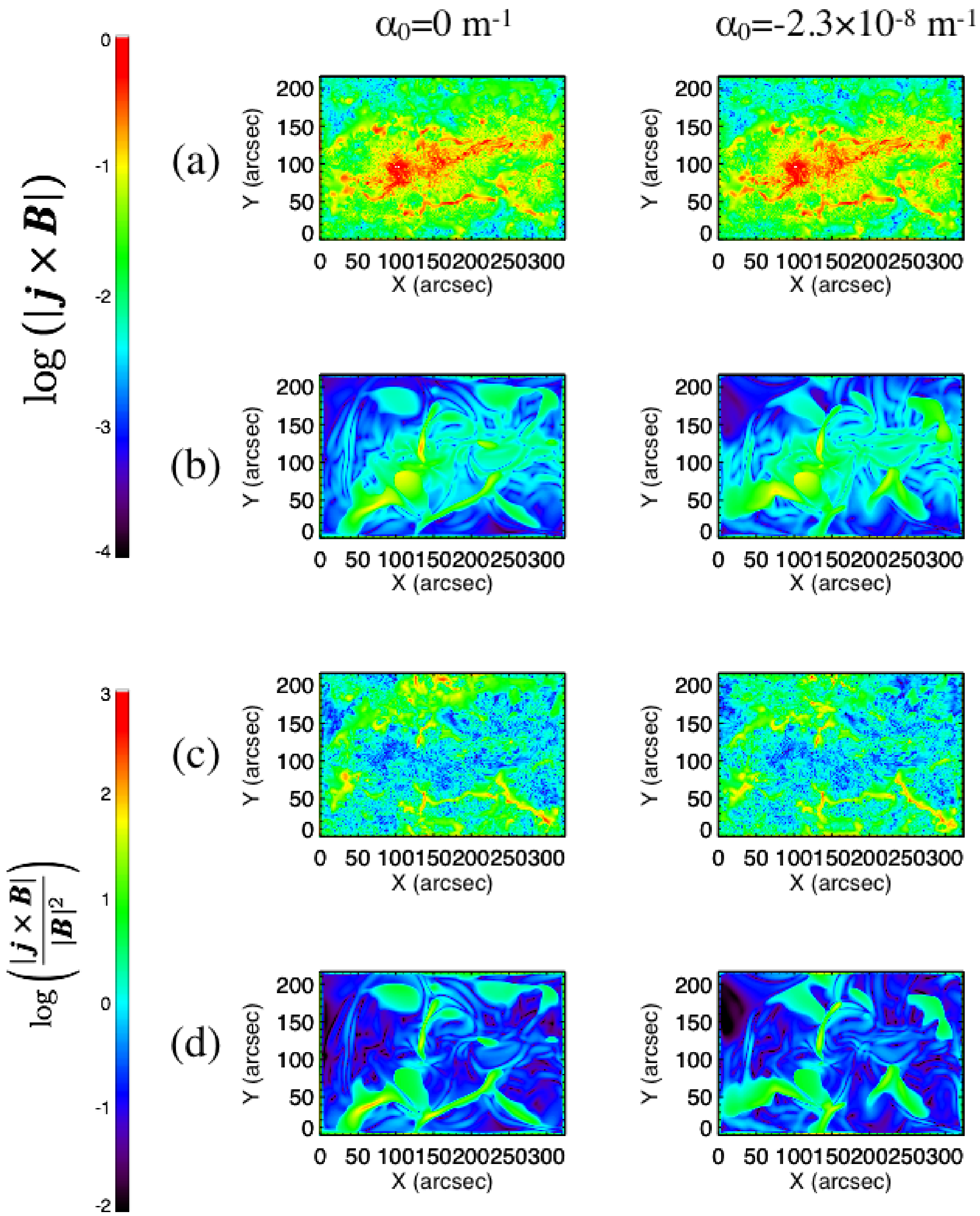

Figure 2.23: (a) and (c): The Lorentz force and the normalized Lorentz force distribution at 2600 km height for NOAA 11967 for $\alpha_0 = 0\ \mathrm{m}^{-1}$ (left) and $\alpha_0 = -2.3 \times 10^{-8}\ \mathrm{m}^{-1}$ (right), respectively. (b) and (d): The Lorentz force and the normalized Lorentz force distribution at 26 Mm height for NOAA 11967 for $\alpha_0 = 0\ \mathrm{m}^{-1}$ (left) and $\alpha_0 = -2.3 \times 10^{-8}\ \mathrm{m}^{-1}$ (right), respectively.

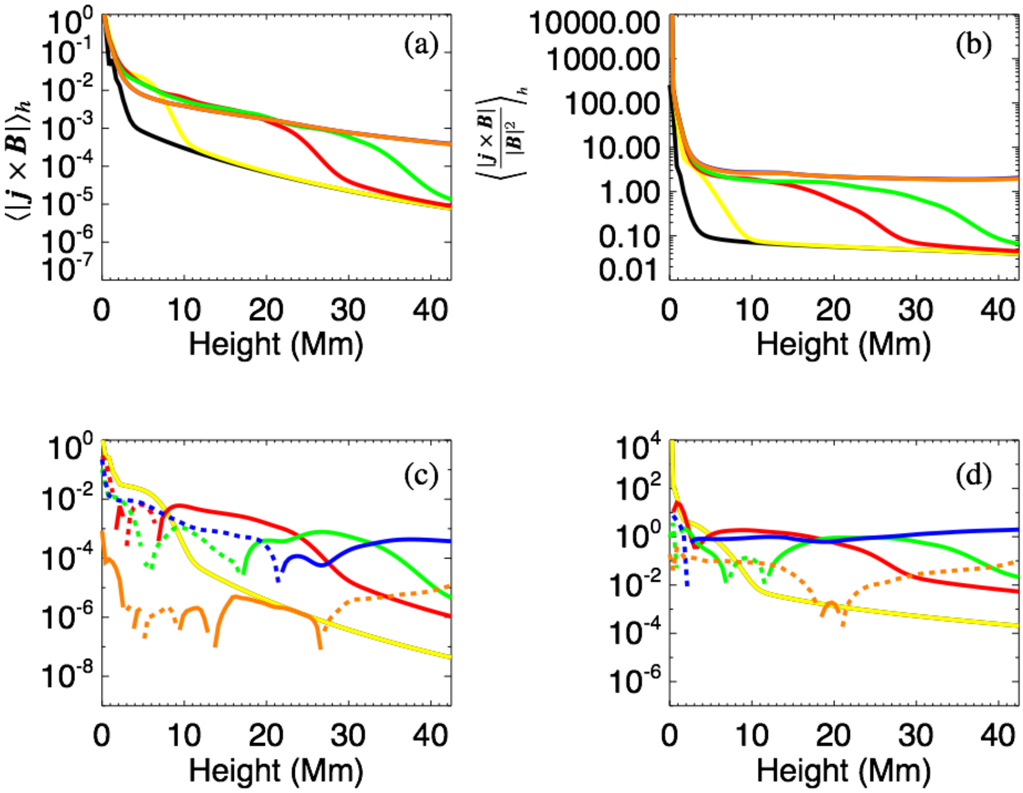

Figure 2.24: (a) and (b):Solid lines show the height distribution of the Lorentz force and the normalized Lorentz force for NOAA 11967, which is averaged at each height. This is the result of $\alpha_0 = 0\ \mathrm{m}^{-1}$. Colors show each time step at 20 (black), 100 (yellow), 500 (red), 900 (green), 25000 (blue), and 45000 (orange) step, respectively. (c) and (d): The temporal variation of the height distribution of the Lorentz force and the normalized Lorentz force. Colors show the time interval between 20 and 100 step (yellow), 100 and 500 step (red), 500 and 900 step (green), 900 and 25000 step (blue), and 45000 step (orange), respectively. Solid lines show the increase, while the dashed lines show the decrease.

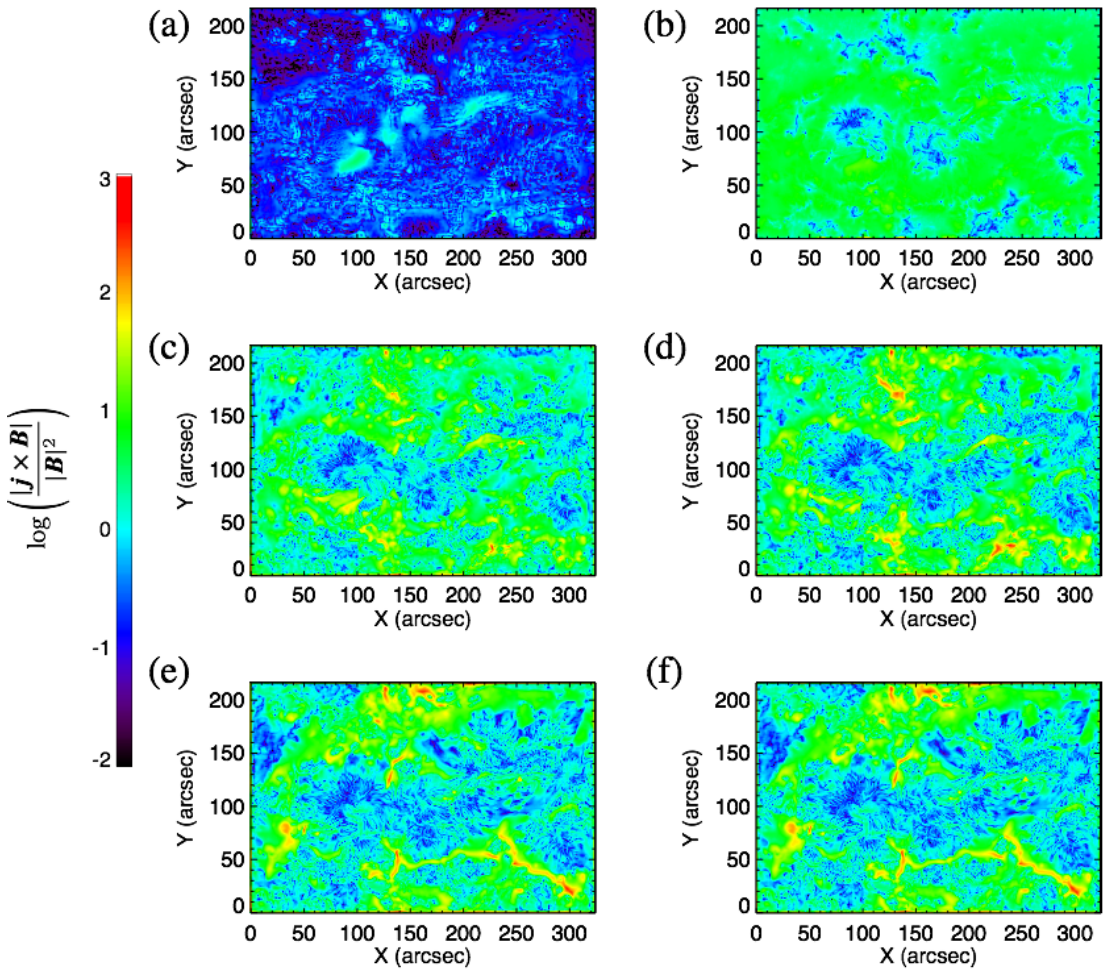

Figure 2.25: The temporal evolution of the normalized Lorentz force distribution at 2600 km for NOAA 11967. This is the result of $\alpha_0 = 0\ \mathrm{m}^{-1}$. Each panel shows each time step at (a) 20 step, (b)100 step, (c) 500 step, (d) 900 step, (e) 25000 step, and (f) 45000 step, respectively.

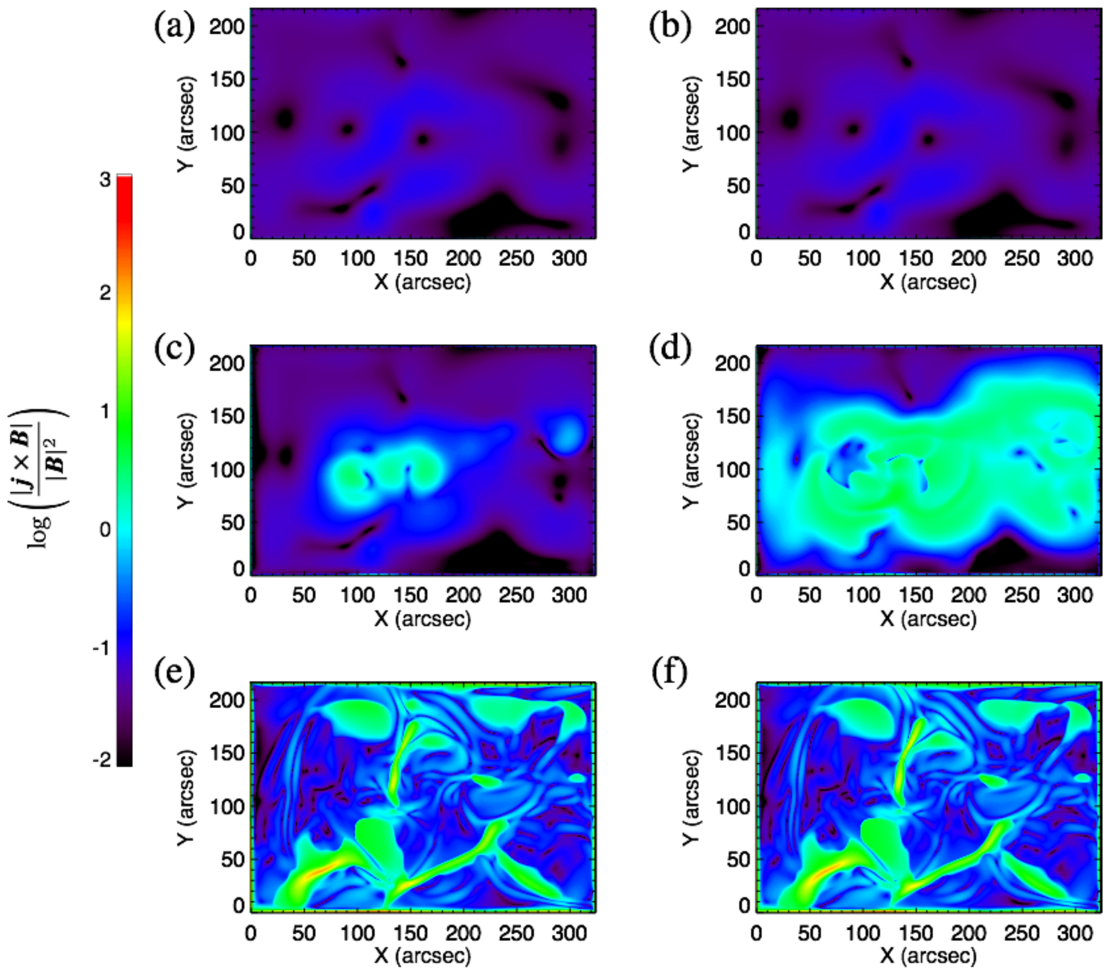

Figure 2.26: The temporal evolution of the normalized Lorentz force distribution at 26 Mm for NOAA 11967. This is the result of $\alpha_0 = 0\ \mathrm{m}^{-1}$. Each panel shows each time step at (a) 20 step, (b)100 step, (c) 500 step, (d) 900 step, (e) 25000 step, and (f) 45000 step, respectively.

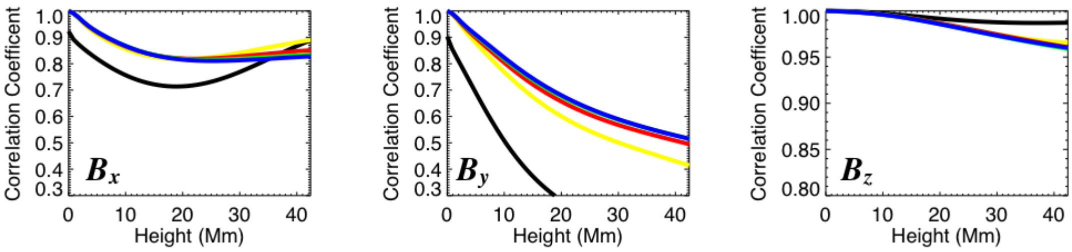

Figure 2.27: The height variation of the correlation coefficient between the vector magnetic field of the NLFFF result with $\alpha_0 = 0\ \mathrm{m}^{-1}$ and $\alpha_0 = -2.3 \times 10^{-8}\ \mathrm{m}^{-1}$ for NOAA 11692. The left, middle, and right panels show the correlation coefficients for B_x, B_y, and B_z, respectively. Colors show the iteration steps at the initial condition (black),12000 steps (yellow), 24000 steps (red), 36000 steps (green), 60000 steps (blue).

We investigated the height variation of the correlation coefficient between the NLFFF calculated with different initial condition as shown in Figures 2.27 and 2.28. By investigating the correlation coefficient, we try to reveal whether the initial condition dependency in the higher region will vanish by increasing the step number. In other words, we try to answer whether the different NLFFF solution shown in Figures 2.11 and 2.14 will converge to the unique solution by increasing the step number. Same as Section 2.4.4, the result with $\alpha_0 = 0\ \mathrm{m}^{-1}$ is compared with that with $\alpha_0 = -2.3 \times 10^{-8}\ \mathrm{m}^{-1}$.

Figure 2.27 shows the height variation of the correlation coefficient for NOAA 11692. The left, middle, and right panels show the correlation coefficients for B_x, B_y, and B_z, respectively. Colors show the iteration steps at the initial condition (black),12000 steps (yellow), 24000 steps (red), 36000 steps (green), 60000 steps (blue). At the initial condition, the correlation coefficient of B_y is smaller compared with B_x and B_y because the difference of the force-free alpha around the polarity inversion line affect the y component. As the iteration steps increases, the correlation coefficient also increases for the horizontal magnetic field. However, between 36000 (green) and 60000 (blue) steps, the correlation coefficient does not change at all. Therefore increasing the iteration steps more than 60000 may not change the NLFFF result any more.

Figure 2.28 shows the height variation of the correlation coefficient for NOAA 11967. Colors show the iteration steps at the initial condition (black), 8000 (yellow), 25000 (red),

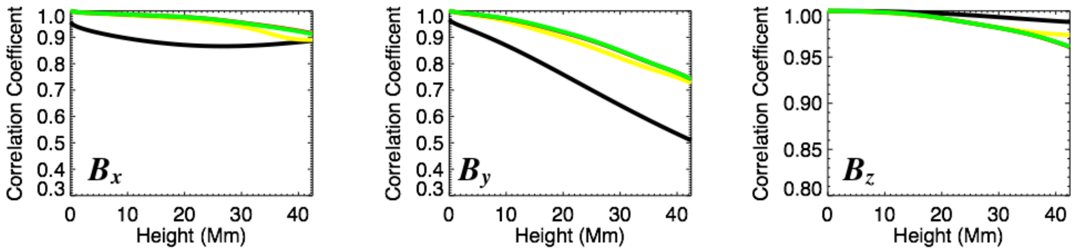

Figure 2.28: The height variation of the correlation coefficient between the vector magnetic field of the NLFFF result with $\alpha_0 = 0\,\mathrm{m}^{-1}$ and $\alpha_0 = -2.3 \times 10^{-8}\,\mathrm{m}^{-1}$ for NOAA 11967. The left, middle, and right panels show the correlation coefficients for B_x, B_y, and B_z, respectively. Colors show the iteration steps at the initial condition (black), 8000 (yellow), 25000 (red), and 45000 (green).

45000 (green). Similar to the correlation coefficients for NOAA 11692, as the iteration steps increases, the correlation coefficient also increases for the horizontal magnetic field and the correlation coefficient does not change any more between 25000 (red), and 45000 (green) steps. For NOAA 11967, iterating more steps may also not change the NLFFF results.

2.5 Discussions

We calculated NLFFF with 5 and 12 different initial conditions for NOAA 11692 and 11967, respectively. Summary of our results is as follows.

1. According to the comparison with the soft X-ray image, the NLFFF shows better correspondence in the simple active region NOAA 11692, when the initial constant force-free alpha is the same sign with the global alpha calculated from the photospheric magnetic field, as shown in Figure 2.5. On the other hand, in the complex multi-pole active region NOAA 11967, the results of the NLFFF extrapolations are less dependent on the initial condition, as shown in Figure 2.7.

2. Total magnetic energy of the NLFFF extrapolation does not strongly depend on the initial condition as shown in Tables 2.2 and 2.3. The dependence of the free energy is larger compared to the total magnetic energy.

3. The solution of NLFFF at the region where the strong magnetic field exists, e.g., magnetic field in the lower height, tends to be less affected by the initial condition, as shown in Figure 2.9. On the other hand, the region in the weak magnetic field around the polarity inversion line, tends to be affected by the initial condition.

4. Except for the case $\alpha_0 = -12 \times 10^{-8}\mathrm{m}^{-1}$ in NOAA 11967, the NLFFF extrapolation is considered to be converged, as shown in Figure 2.16. The increase of the calculation steps may not affect the results in this study.

From Figures 2.9, 2.27, and 2.28, the magnetic field in the lower height region tends to be less affected by the initial condition, while the magnetic field at the higher region is strongly affected by the initial condition. There is a possibility that this result is caused by the convergence problem of the NLFFF modeling. We discuss following two possible reasons.

The first possible reason is that the information of the bottom boundary has not reached at the higher region yet. In the MHD relaxation method, the NLFFF is achieved by the propagation of the disturbance as psuedo-Alfvén wave, which is produced by the artificial change of the bottom boundary according to Equation (2.8). Because we assume $\rho = |\boldsymbol{B}|$ in the MHD calculation, the Alfvén velocity is $B/\sqrt{4\pi\rho} \sim \sqrt{B}$. At the higher region and weak magnetic field region, there is a possibility that the psuedo-Alfvén wave has not reached yet. This possibility is rejected by the result in Figures 2.19 and 2.24, which show that the Lorentz force is transported to the higher region.

The second possibility is the difference of the convergence speed among each height. We used the resistivity defined as Equation (2.6), which becomes large when the Lorentz force or the velocity becomes large. Because the Lorentz force and the velocity tends to become large at the lower height, the resistivity tends to be larger in the lower region than in the higher region. The large resistivity allows the magnetic field to be relaxed faster at the lower height. For the second possibility, it is unlikely that the magnetic field at the higher region converges to one unique solution by increasing iteration steps. As shown in

Figures 2.27, and 2.28, the correlation coefficient between the results of different initial condition does not change significantly by increasing the iteration steps. This result shows that the different NLFFF solution in the higher region does not converge to the unique solution by just increasing the iteration number. Regarding the convergence of the NLFFF results, from the result in Figure 2.21 and 2.26, the distribution of the Lorentz force does not significantly change after 24000 step for NOAA 111692 and 25000 step for NOAA 11967. This result indicates that the current scheme can not reduce the Lorentz force at the higher region any more.

From above discussions, we conclude that our NLFFF results converge in the sense that the remaining Lorentz force does not change any more. Therefore, our results suggest that the current scheme of the NLFFF modelings, including our MHD relaxation method, allow the different result (initial condition dependency) at the higher region. In other words, there exist several local minimums for the force-free equilibrium at the higher region. Because the initial condition is modified based on the information of the bottom boundary, larger degree of freedom is allowed at the higher region compared to the lower region. For example, in our MHD relaxation method, the information of the bottom boundary is transported by the propagation of the psuedo-Alfvén wave as mentioned above. The region which is far from the boundary tends to be less affected by the psuedo-Alfvén wave and remain almost unchanged from the initial equilibrium state (potential-like or LFFF-like). Note that this possibility does not prove that the degree of freedom of the NLFFF solution is mathematically larger at the higher region because certain amount of the Lorentz force remains in our calculaiton. To solve this problem, we suggest that additional observational limitation should be given to the current NLFFF modeling such that the magnetic field at the higher region can converge to the NLFFF result, which is consistent with X-ray and/or EUV imaging observations. The future prospects of the improvement of the current NLFFF modeling is discussed in Section 4.2.

We have to note that although the magnetic field at the lower height is less affected by the initial condition, certain amount of the Lorentz force remains, as shown in Figures

2.17 and 2.22. The main reason of the remaining Lorentz force in the calculation box may be due to the non-force-freeness of the photospheric magnetic field at the bottom boundary. Since the photospheric magnetic field is not ideally force-free, the non-zero Lorentz force will be produced in the current NLFFF scheme. Therefore, strictly speaking, we do not obtain ideal force-free solution in the current NLFFF scheme. We investigate how this non-force-freeness at the bottom boundary affect the accuracy of the NLFFF modeling by comparing the NLFFF and chromospheric observations in Chapter 3. This problem should be solved by using more force-free bottom boundary, such as chromospheric magnetic field, which is also discussed in Section 4.2.

We compared NLFFF results with coronal loops observed with *Hinode*/XRT. For NOAA 11967, 3D magnetic field configuration is similar to each other and looks consistent with X-ray observation when the absolute value of initial force-free alpha is smaller. On the other hand, NOAA 11692 shows strong initial condition dependence in Figure 2.5. The clear difference between NOAA 11967 and 11692 is the complexity of the photospheric magnetic field. Our results suggest that the NLFFF result of NOAA 11967 is less affected by the initial condition than that of NOAA 11692. Because we analyze only two active region, we can not determine the cause of this result. Therefore, we discuss the candidates of the cause of difference in terms of the property of two active region. There are five possibilities to explain this cause. Firstly, our results show that the strong field region tends to be less affected by the initial condition as discussed above. NOAA 11967 has more magnetic flux, 8.4×10^{22} Mx, than that of NOAA 11692, 3.7×10^{22} Mx. This means that there are more strong magnetic field region above the photosphere. Second possibility is magnetic flux unbalance at the photospheric height. In the NLFFF modeling, magnetic flux unbalance at the bottom boundary may produce inconsistent results and may be related to the initial condition dependence. The net vertical magnetic flux normalized by the total magnetic flux is -0.03 for NOAA 11692 and 0.17 for NOAA 11967. This shows that the magnitude of unbalance of vertical magnetic flux is larger in NOAA 11967 than in NOAA 11692. Because the NLFFF results of NOAA 11967 are less affected by the initial condition, the flux unbalance in this study may not affect the initial condition dependence. Thirdly, there is a difference of the horizontal field distribution between the two active regions. As shown in Figure 2.1, strong horizontal magnetic field occupies a large part of the FOV of NOAA 11967 for all four polarities. On the other hand, in NOAA 11692, while the horizontal magnetic field can be seen in the negative sunspot, there is no strong horizontal magnetic field in the positive polarity. As shown in Figure 2.4, while 6.3 $\%$ of the horizontal magnetic field in the FOV is larger than 1000 G for NOAA 11967, 0.49 $\%$ is larger than 1000 G for NOAA 11692. This suggests that the limitation of the connectivity from the bottom boundary may become strong due to the strong horizontal magnetic field and result in the less initial condition dependence. Fourth possibility is the difference in the force-freeness at the photospheric height. Although force-freeness of the both active regions is relatively small, that of NOAA 11967 ($|F_z|/F_p = 0.089$) is smaller than that of NOAA 11692 ($|F_z|/F_p = 0.17$). The large value of the force-freeness may affect the dependence of the initial condition on the NLFFF result. Fifth possibility is the length scale of the field lines. While the height of the loop top in NOAA 11692 is around 100 Mm as shown in Figure 2.6, that in NOAA 11967 is around 30 Mm as shown in Figure 2.8. This result means that the coronal loops identified in the soft X-ray images are different between NOAA 11692 and 11967. Our result shows that the magnetic field in the higher region tends to be affected more strongly by the initial condition than that in the lower region. Therefore, in comparison with the soft X-ray image in NOAA 11692, we compared the field lines, which tend to be affected by the initial condition. However, as shown in Figures 2.12 and Figures 2.15, NOAA 11692 is more dependent on the initial condition than NOAA 11967 even in the same height. This result indicates that only the difference of the length scale is not the cause of the difference of the dependence between the two active regions.

As shown in Tables 2.2 and 2.3, the total magnetic energy does not strongly depend on the initial condition. On the other hand, the free energy shows larger difference among each solution than the total magnetic energy. Since the free energy is defined as the deviation between the magnetic energy and potential magnetic energy, the small difference of the total magnetic energy becomes large difference in free energy. This ratio is smaller than previous studies focusing on other dependences, such as method dependence (De Rosa et al., 2009, total energy: 1.9 between Reg^{+} and $\mathrm{Am1}^{-1}$), instrument dependence between *Hinode* and *SDO* (Thalmann et al., 2013, total energy: ~ 2.2, free energy: ~ 2.5), spatial resolution dependence (DeRosa et al., 2015, total energy:~ 1.4, free energy: ~ 2 in magnetofrictional method). This means that the initial condition dependence of the total magnetic energy and free energy in our MHD relaxation method is comparatively small. The uniqueness of total energy and free energy can be explained by using our results. Since the magnetic energy and free energy concentrate in the lower height, they become less dependent to the initial condition.

Regarding NOAA 11692, the initial values, which produce consistent results with observations ($\alpha_0 = -2.3 \times 10^{-8}\mathrm{m}^{-1}$), are larger than the global photospheric force-free α, $-1.0 \times 10^{-8}\mathrm{m}^{-1}$. Therefore, our results offer an important suggestion that the more twisted magnetic field than that estimated from photospheric field might exist in the upper atmosphere and if we give a linear force-free field, whose α_0 is close to (or larger) the photospheric global force-free α, we may obtain more realistic twisted field lines easily. Especially, the initial condition dependence can be found around the polarity inversion line as clearly shown in Figure 2.11. The non-potentiality of the magnetic field around the polarity inversion line is important in terms of the onset mechanism of solar flares (Kusano et al., 2012; Bamba et al., 2013; Wang et al., 2017). Our results provide the improvement of the estimation of the 3D magnetic field structure around the polarity inversion lines and will help the correct understanding of the onset mechanism of solar flares.

2.6 Summary

Summarizing our findings in Chapter 2,

(1) The solution of NLFFF at the region where the strong magnetic field exists, e.g., magnetic field in the lower height (<10 Mm), tends to be less affected by the initial condition, although the Lorentz force is concentrated at the lower height.

(2) Total magnetic energy of the NLFFF extrapolation does not strongly depend on the initial condition.

(3) The NLFFF extrapolation of the complex active region NOAA 11967 is less dependent on the initial condition compared to that of NOAA 11692.

In Section 1.4.1, we proposed the problem whether completely different solutions with the same bottom boundary exist or not. We conclude that we obtain completely different 3D NLFFF structure from the different initial conditions with the same bottom boundary. However, the initial condition dependence is small (the correlation coefficient $C > 0.9$) where the the magnetic field is strong, e.g., in the lower height (<10 Mm). We also reveal that the 10-100 times larger Lorentz force, which is normalized by the square of the magnetic field strength, remains at the lower height ($<$ 10 Mm) than that at higher region ($>$ 10 Mm). The magnitude of the dependence is also different between the two active regions.

Chapter 3

Chromospheric Magnetic Field in Solar Active Regions

3.1 Introduction

In this chapter, we investigate how the magnetic field is distributed in the chromospheric height and check the reliability of the NLFFF modeling. Because the plasma beta in the upper chromosphere ($>$ 1000 km) is sufficiently small compared to the photosphere as shown in Figure 1.5, understanding the chromospheric magnetic field is quite important in terms of the improvement of the NLFFF modeling as mentioned in Chapter 1.

The magnetic field vector at the chromospheric height has been studied based on the spectropolarimetric observations with ground-based telescope. Solanki et al. (2003) determined the chromospheric vector magnetic field in small emerging active regions through the inversion of the spectropolarimetric data at He I 10830 Å. They revealed the existence of a tangential discontinuity of the magnetic field direction, which is the observational signature of an electric current sheet. The magnetic field vector at other chromospheric features has also been studied such as the active region filaments (Xu et al., 2012), superpenumbral fine structure (Schad et al., 2013, 2015), and sunspot (Joshi et al., 2017). The application of the chromospheric magnetic field to the NLFFF modeling was also investigated. Yamamoto & Kusano (2012) developed the new preprocessing method, with which we can obtain magnetic field similar to those in the chromosphere from the photospheric observations. The preprocessing method was firstly proposed by Wiegelmann et al. (2006), which minimizes the total force and torque on the bottom boundary. They added a new term concerning chromospheric longitudinal fields into the method of Wiegelmann et al. (2006). They found that some preprocessed fields show the smallest force- and torque-freeness. Yelles Chaouche et al. (2012) investigated the the three-dimensional structure of an active region filament. They performed NLFFF extrapolations based on simultaneous observations at a photospheric (Si I 10827 Å) and a chromospheric (He I 10830 Å) height. The extrapolations yield a filament formed by a twisted flux rope whose axis is located at about 1.4 Mm above the solar surface.

Although previous studies revealed many properties of the chromospheric magnetic field, the FOV of their observations was limited because the seeing made it difficult to perform the stable large FOV scanning. The comparison between the NLFFF extrapolation and the chromospheric magnetic field is difficult with the small FOV observation. By analyzing the chromospheric magnetic field in the whole active regions, we attempt to reveal the non-potential magnetic field distribution in the chromosphere through spectropolarimetric observations at He I 10830 Å and how significantly the magnetic field at the chromospheric height derived by the current NLFFF modeling with photospheric magnetic field is deviated from the measured chromospheric magnetic field. We analyze two active regions, NOAA 10969 and NOAA 11861. In terms of the force-freeness based on the Equations (1.16), (1.17), and (1.18), the former has $|F_z|/F_p > 0.1$, while the latter satisfies $|F_x|/F_p < 0.1$, $|F_y|/F_p < 0.1$, and $|F_z|/F_p < 0.1$ as shown in Table 3.1. The possibility that the force-freeness depends on the spatial scale and the FOV is discussed in Appendix A.1 and A.2.

Table 3.1: Force-freeness of the active region from Equations (1.16), (1.17), and (1.18)

	NOAA 10969	NOAA 11861
$\lvert F_x \rvert / F_p$	0.018	0.024
$\lvert F_y \rvert / F_p$	0.038	0.071
$\lvert F_z \rvert / F_p$	0.43	0.03

3.2 Observations and Data Reduction

3.2.1 Observations of NOAA 10969

NOAA active region 10969 was a simple bipolar active region as shown in the upper panels of Figure 3.1. The leading sunspot has a negative polarity and there are several positive magnetic islands to the east of the sunspot. The *Hinode*/SOT SP measured the full stokes vector of Fe I 6301.5 Å and 6302.5 Å in the period between 11:16 UT and 12:42 UT on 28 Aug 2007. The spectral sampling is 21.5 mÅ per pixel NOAA 10969 was located close to the disk center, i.e., (111 ″, -184″) in the heliocentric coordinate at that time. The black arrow shows the direction of the disk center. The black box shows the region of interest (ROI) in Figures 3.2, 3.5, and 3.6. The map has an effective pixel size of 0″.16 along slit and 0″.15 slit step with FOV of 152″×164″. The left upper panel of Figure 3.1 shows the continuum image created from the SP data.

NOAA 10969 was also observed by the Tenerife Infrared Polarimeter-2 (TIP-2; Collados et al., 2007) mounted on the German Vacuum Tower Telescope (VTT) at Observatorio del Teide, Tenerife, Spain between 10:18-10:38 UT on 28 Aug 2007. The VTT/TIP-2 measured the full stokes vector of He I triplet at 10830 Å with a spectral sampling of 11 mÅ per pixel. The exposure time was 0.25 seconds and four accumulations per modulation step were performed. The noise level of the continuum intensity was 3×10^{-3}. The image of line core of He I 10830 Å is shown in the upper middle panel of Figure 3.1.

The active region was scanned with $0.''18$ slit and steps of $0.''5$. Because the scanning was sparse raster, there might be small magnetic flux which cannot be detected in this scanning.

To investigate the coronal field lines structure, we used the EUV data at 171 Å obtained with *Transition Region and Coronal Explorer* (*TRACE*; Handy et al., 1999). This channel is sensitive to coronal plasma at a temperature around 1 MK. The EUV image was observed at 10:48 UT on 28 Aug 2007 with a spatial resolution of $1''(0''.5$ pixel$^{-1})$.

3.2.2 Observations of NOAA 11861

NOAA active region 11861 has multiple sunspots. The continuum image observed with *SDO*/HMI at 16:48 UT on 12 Oct 2013 is shown in the bottom panel fo Figure 3.1. NOAA 10969 was located close to the disk center, i.e., $(0\,'', -250'')$ in the heliocentric coordinate at that time. The black arrow shows the direction of the disk center. The black box shows the ROI in Figures 3.3, 3.8, and 3.9.

The full stokes vector of He I 10830 Å was obtained by the Facility Infrared Spectropolarimeter (FIRS; Jaeggli et al., 2010) at the Dunn Solar Telescope (DST) located on Sacramento Peak in New Mexico, USA. The FIRS scanned the active region between 16:24 and 17:16 UT on 12 Oct 2013 with a spectral sampling of 39 mÅ per pixel. The image of line core of He I 10830 Å is shown in the lower middle panel of Figure 3.1. The active region was scanned with $0.''15$ slit and steps of $0.''3$ with FOV of $132''\times66''$. The exposure time was 0.125 seconds and four accumulations per modulation step were performed. The noise level of the continuum intensity was 1×10^{-2}.

The Atmospheric Imaging Assembly (AIA; Lemen et al., 2012) aboard the *SDO* observes the full-disk EUV image of the Sun with a $1''.5$ spatial resolution. We used 171Å channel observed at 16:47 UT on 12 Oct 2013, as shown in the lower right panel of Figure 3.1.

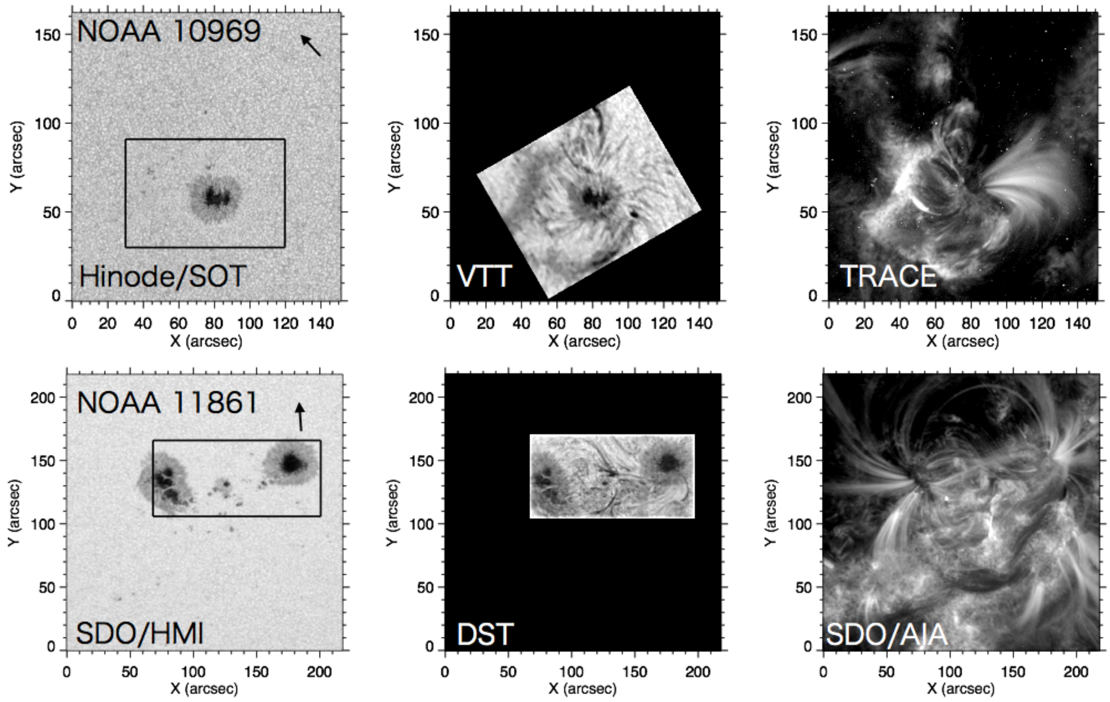

Figure 3.1: Upper left: The continuum image obtained with *Hinode*/SOT SP between 11:16 UT and 12:42 UT on 28 Aug 2007. The black arrow shows the direction of the disk center. The black box shows the region of interest (ROI) in Figures 3.2, 3.5, and 3.6. Upper middle: The line core image of He I 10830 Å obtained with VTT/TIP-2 between 10:18-10:38 UT on 28 Aug 2007. Upper right: The EUV image at 171 Å obtained with *TRACE* at 10:48 UT on 28 Aug 2007. Lower left: The continuum image obtained with *SDO*/HMI at 16:48 UT on 12 Oct 2013. The black arrow shows the direction of the disk center. The black box shows the ROI in Figures 3.3, 3.8, and 3.9. Lower middle:The line core image of He I 10830 Å obtained with DST/FIRS between 16:24 and 17:16 UT on 12 Oct 2013. Lower right: The EUV image at 171 Å obtained with *SDO*/AIA at 16:47 UT on 12 Oct 2013.

3.2.3 Data Reduction

Same as Chapter 2, for the calibration of the Hinode/SOT SP data, we used the Solarsoft routine SP_PREP (Lites & Ichimoto, 2013). After the calibration of the spectropolarimetric data, we applied a Milne-Edington inversion described in Section 2.2. The 180 degree ambiguity in the transverse magnetic field direction was solved with the minimum energy ambiguity resolution method (Metcalf, 1994; Leka et al., 2009). For the HMI data, we used the vector magnetic field data product, SHARP (Bobra et al., 2014). For the VTT data, flat field, dark current corrections, and the standard polarimetric calibration were carried out (Collados et al., 1999; Collados, 2003). The wavelength calibration was also performed by fitting observed spectrum with solar spectrum atlas (Delbouille et al., 1981). In order to improve the signal-to-noise ratio, we carried out a binning of 4 pixel in spectral domain and 4 pixel along slit direction. The resulting noise levels of stokes Q/I, U/I, and V/I are 5.3×10^{-4}, 6.3×10^{-4} and 7.8×10^{-4}, respectively. For the DST data, we carried out the basic data reduction including flat fielding, dark current corrections, and polarimetric calibration (Beck et al., 2005). The wavelength calibration was performed by fitting with solar spectrum atlas, which is the same method applied to the VTT data. Because the significant polarized fringes are found in the DST data, we performed a pattern-recognition based on two-dimensional principal component analysis (Casini et al., 2012). A binning of 2 pixels in the spectral domain and along the slit, and 4 pixels along the scanning direction were carried out. The resulting noise levels of stokes Q/I, U/I, and V/I are 1.0×10^{-4}, 7.2×10^{-5} and 5.4×10^{-4}, respectively. When we resolved the ambiguity of He I 10830 Å, we assumed that there is only 180 degree ambiguity and choose the azimuth close to the potential field. The ambiguity of the inversion results will be discussed in Section 3.5

Figure 3.2 shows the absolute peak values of Stokes Q/I, U/I, and V/I in NOAA 10969. The signal of Stokes V is strong in the leading sunspot and the magnetic islands of the positive polarities where the vertical magnetic field exists. The strong Q and U signals can be identified in the outer part of the spot and the fibril structure between the positive and negative polarities, which come from the Zeeman effect and/or the Hanle effect.

As similar to Figure 3.2, Figure 3.3 shows the absolute peak value of Stokes Q/I, U/I, and V/I in NOAA 11861. The strong Stokes V can be seen in the two large spots and small spot between them. There are strong Q and U signals in the penumbral regions.

3.2.4 Inversion of He I 10830 Å

The inversion of He I 10830 Å was performed by HAZEL (Asensio Ramos et al., 2008), which considers the joint action of the Hanle and Zeeman effects. In order to obtain physical parameters from the polarimetric observations, we need to solve the radiative transfer equation in Equation (1.6). In the most general case, we solve the radiative transfer equation considering that the solar medium varies along the ray path. Because the formation layer of He I 10830 Å is sufficiently thin as described in Section 1.5.2, we can assume the absorption medium of He I 10830 Å as a constant-property slab in which physical property is constant along the ray path. We have the analytical solution in the case of a constant-property slab as follows,

$$\boldsymbol{I} = \exp(-\boldsymbol{K}^{*}\tau)\boldsymbol{I_0} + (\boldsymbol{K}^{*})^{-1}\left[1 - \exp(-\boldsymbol{K}^{*}\tau)\right]\boldsymbol{S}, \tag{3.1}$$

where $\boldsymbol{I_0}$ is the Stokes vector illuminating the slab's bottom boundary as shown in Figure 3.4. The propagation matrix $\boldsymbol{K}^{*} = \boldsymbol{K}/\eta_I$, and the source function vector $\boldsymbol{S}$, in Equation (3.1) depend on the multipolar components of the atomic density matrix, ρ. There are eight parameters for the slab model of HAZEL. The free parameters are the magnetic field strength, the inclination and azimuth of magnetic field vector, the optical width of the slab, the height of the slab, doppler width, doppler velocity, and line damping parameter. The Inclination and azimuth angles are defined in the line-of-sight frame coordinate and they are converted to the angles in the local frame coordinate where 0 and 180 degree are defined as the vertical to the solar surface. In order to reduce the time of the calculation,

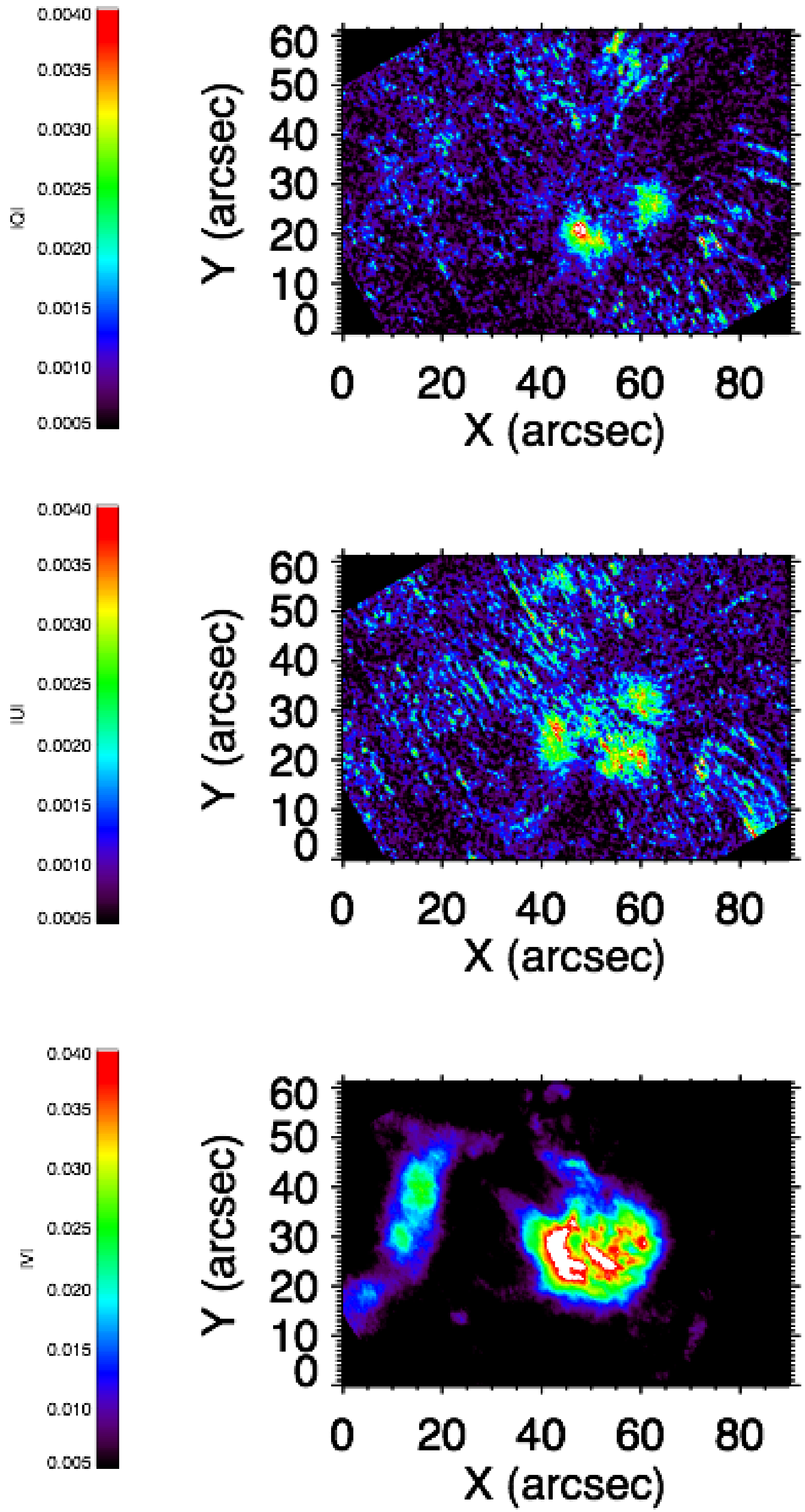

Figure 3.2: The absolute peak value of Stokes Q, U, and V of NOAA 10969 at He I 10830 Å obtained with VTT/TIP-2 between 10:18–10:38 UT on 28 Aug 2007.

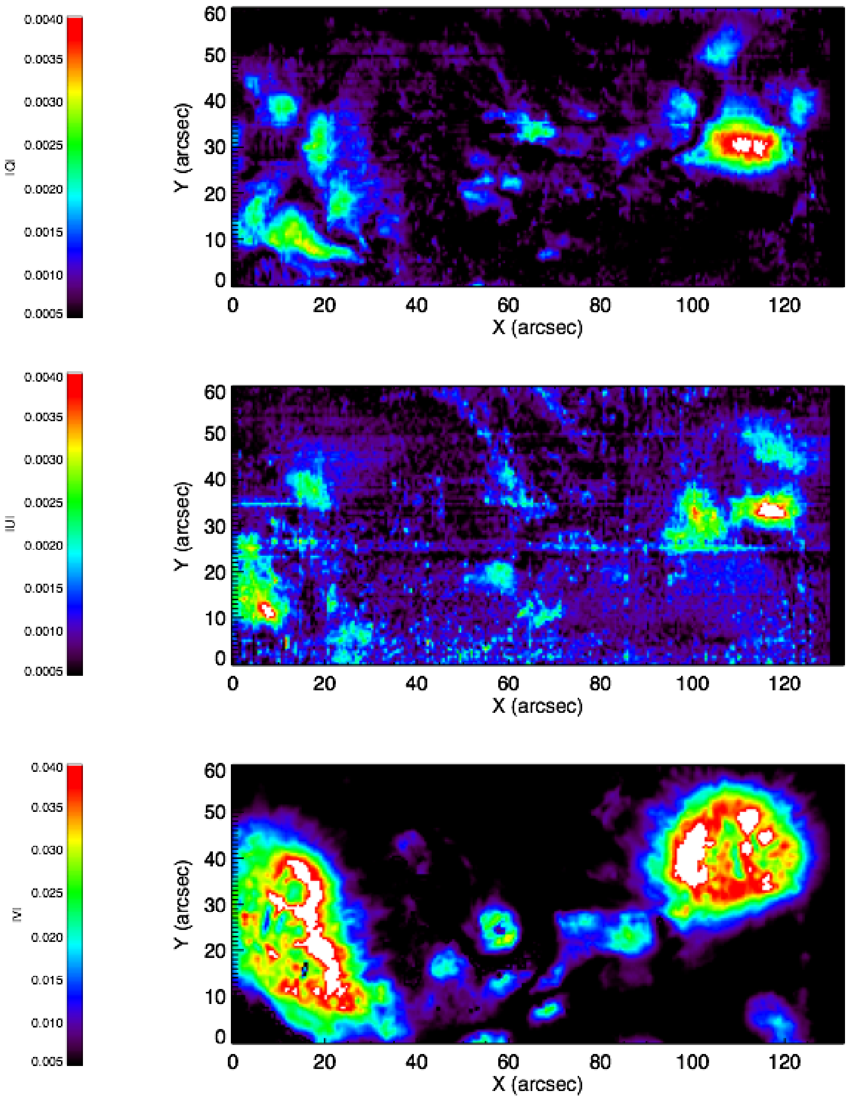

Figure 3.3: The absolute peak value of Stokes Q, U, and V of NOAA 11861 at He I 10830 Å obtained with DST/FIRS between 16:24 and 17:16 UT on 12 Oct 2013.

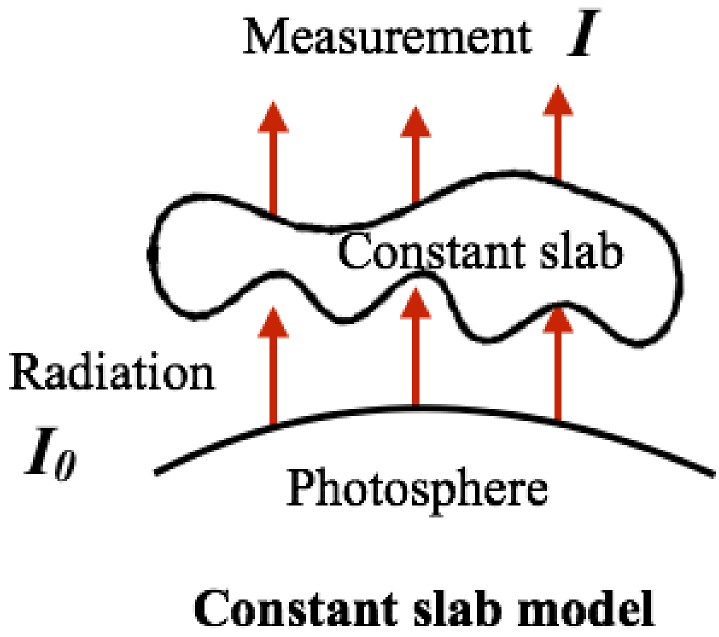

Figure 3.4: The constant slab model in the inversion code of HAZEL. The code assumes that the constant-property slab is illuminated from the photosphere.

we kept two parameters fixed. The first fixed parameter is the damping parameter. The damping parameter of the Voigt profile due to collisional and radiative damping is usually used for fitting the non-Gaussian profiles. In He I 10830 Å, however, the Doppler broadening dominates the line width and the collisional and radiative dampings are weak. In addition, Lagg et al. (2004) reported that the inclusion of the damping parameter improves the inversion results without affecting the other parameters. Because we mainly focus on the magnetic field vector in this thesis, the damping parameter was fixed to 0. The second parameter is the height of the slab. The scattering polarization and Hanle effect depend on the anisotropy of the radiation field. Because the height of the slab increases the anisotropy, the linear polarization signal is slightly affected by the height of the slab (Merenda et al., 2011). However, unphysical results often appear when we fit the height of the slab. Therefore, the height of the slab was fixed to be 2 $''\sim$ 1500 km in this study.

When we discuss the horizontal magnetic field, we examined the pixels with linear polarization signals higher than 0.12%. We judged the inversion result by $\sigma_{\rm qu}$ defined as,

$$\sigma_{\rm qu} = \frac{\frac{1}{n}\sum_{i=1}^{n}\sqrt{(Q_{\rm obs}-Q_{\rm syn})^2+(U_{\rm obs}-U_{\rm syn})^2}}{\sqrt{Q_{\rm peak}^2+U_{\rm peak}^2}}, \tag{3.2}$$

where n is wavelength point, $Q_{\rm obs}$ and $U_{\rm obs}$ are observed Stokes profiles, $Q_{\rm syn}$ and $U_{\rm syn}$ are synthesized Stokes profiles, $Q_{\rm peak}$ and $U_{\rm peak}$ are the peak values of the linear polarization. We checked some pixels and decided to discuss pixels where $\sigma_{\rm qu} < 0.08$.

3.3 NLFFF Extrapolation

NLFFF calculations were performed by the MHD relaxation method described in Chapter 2. The bottom boundary is photospheric magnetic field observed with *Hinode*/SOT SP for NOAA 10969 and *SDO*/HMI for NOAA 11861. The potential field is used as initial guess for both regions. As shown in Chapter 2, the initial condition dependence is small at the chromospheric height and we can probably neglect the initial condition dependence in this study. To eliminate the concern about the initial condition dependence, we also performed the NLFFF extrapolation by using linear force-free field as the initial guess for only NOAA 10969 and discussed the result in Section 3.4.5. The length and magnetic field were normalized by $L_0 = 110$ Mm (NOAA 10969) and $L_0 = 157$ Mm (NOAA 11861) and $B_0 = 3000$ G. The numerical domain is set to $(0,0,0) < (x,y,z) < (1.0,1.07,0.25)$ resolved by $504 \times 540 \times 504$ nodes for NOAA11692 and $(0,0,0) < (x,y,z) < (1.0,1.0,0.75)$ resolved by $432 \times 432 \times 648$ nodes for NOAA 11861. The calculation steps of the results shown in this thesis were set to 40000 steps for both NOAA 10969 and NOAA 11861. The convergence evaluation will be done in Section 3.4.5

3.4 Results

3.4.1 Vector Magnetic Field in the Photosphere and the Chromosphere

In this section, the photospheric and chromospheric magnetic field derived from spectropolarimetric observations are compared for NOAA 10969 and NOAA 11861.

The upper left and lower right panels of Figure 3.5 show vector magnetic field maps at the photospheric and chromospheric heights in NOAA 10969, respectively. The photospheric magnetic field is observed with *Hinode* SOT/SP and the chromospheric field derived from He I 10830 Å observation with VTT. The gray scale shows the magnetic field vertical to the solar surface and the green arrows show the horizontal magnetic field. When we draw the arrows of the horizontal magnetic field, the horizontal field is 12×12 binned. In He I 10830 Å data, the pixels, where the linear polarization signals are small ($< 0.12\%$) or the fitting is poor ($\sigma_{\mathrm{QU}} > 0.08$), are treated as missing data. At the photospheric height, the strong horizontal magnetic field is located in the negative sunspot. The horizontal magnetic field in the sunspot is almost radial to the center of the sunspot. On the other hand, the horizontal magnetic field uniformly distributed at the chromospheric height and the spiral structure can be seen.

To evaluate the non-potentiality at each height, we measured the shear signed angle (SSA), which is defined as,

$$\mathrm{SSA} = \tan^{-1}\left(\frac{B_y B_{xp} - B_{yp} B_x}{B_x B_{xp} + B_y B_{yp}}\right). \tag{3.3}$$

The SSA is the deviation of azimuth angle from the potential magnetic field (B_{xp} and B_{yp}). For the chromospheric magnetic field derived from He I 10830 Å, the SSA is calculated by the potential field calculated from the B_z derived from He I 10830 Å. The top and bottom panels of Figure 3.6 show the SSA at the photospheric height and chromospheric height, respectively. At the chromospheric height, the pixels where the linear polarization

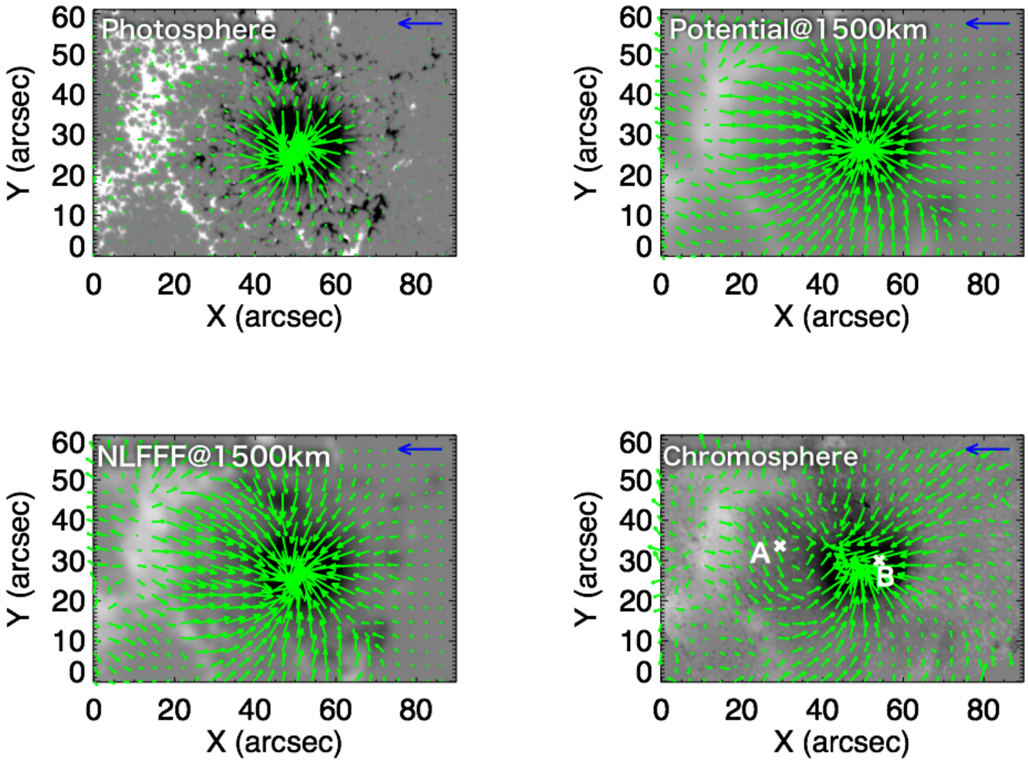

Figure 3.5: The gray scale shows the vertical magnetic field and the green arrows show the horizontal magnetic field of NOAA 10969. The length of blue arrow shows the field strength of 1500 G. Upper Left: Photospheric magnetic field observed with *Hinode*/SOT SP. Upper right: Potential field at 1500 km height. Lower left: NLFFF at 1500 km height. Lower right: Chromospheric magnetic field observed with VTT/TIP-2.

signal is weak and the inversion did not fit the profiles well were masked by black color. The threshold is described in Section 3.2.4. We focus on two region (box 1 and box 2), where the chromospheric magnetic field is accurately derived. The box 1 is the region around the polarity inversion line and the box 2 is the region in the negative sunspot. Figure 3.7 shows the histograms of the SSA in the box 1 and box 2 given in Figure 3.6. The black and red solid lines show the SSA from the chromospheric magnetic field derived from He I 10830 Å and the photospheric magnetic field, respectively. The clear deviation can be seen in the area between the positive and negative polarities in the box 1. While the SSAs in the chromosphere in the box 1 are around -50 degree, at the photospheric height, the SSAs are also around 0 degree although the distribution is broad compared to that of the NLFFF. The SSAs in the chromosphere and those in the photosphere have a similar peak around 0 degree in the histogram in the box 2 in Figure 3.7. However, while the SSAs in the chromosphere in the box 2 have broad distribution, those in the photosphere are concentrated around 0 degree. This result indicates that the chromospheric magnetic field in the box 2 has larger non-potentiality pixels than that in the photosphere.

Regarding NOAA 11861, Figure 3.8 shows the spatial distribution of the vector magnetic field. The upper left and lower right panels show the photospheric field observed with *SDO*/HMI and the chromospheric field derived from He I 10830 Å observation with DST, respectively. Similar property with NOAA 10969 can be seen in the vector magnetic field distribution in NOAA 11861. The horizontal magnetic field in the chromosphere looks more twisted compared to that in the photosphere in both negative and positive sunspots.

The non-potentiality is also evaluated for NOAA 11861 by using the SSA. The difference between photospheric and chromospheric non-potentiality can be seen in Figure 3.9. The top and bottom panel shows the SSA at the photospheric and chromospheric height, respectively. We focus on the boxes 3 and 4, which are located in the leading and following sunspots. Figure 3.10 shows the histogram of the SSA in the box 3 and box 4 given in Figure 3.9. In the box 3, the SSAs in the chromosphere have mainly positive value

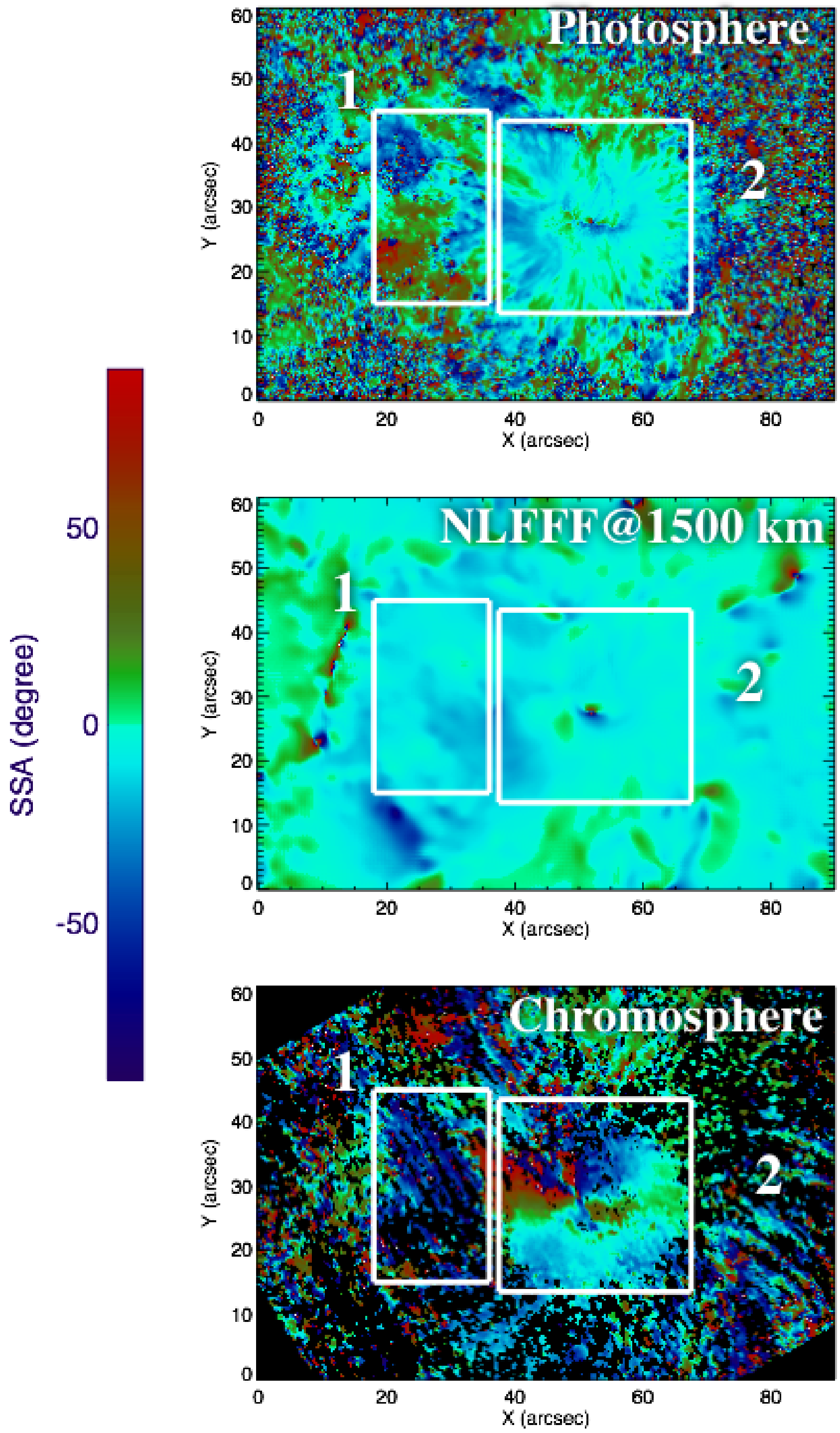

Figure 3.6: The spatial distribution of signed shear angle (SSA) for NOAA 10969. From the top to the bottom for the photosphere, NLFFF at 1500km, chromosphere (He I 10830 Å). The regions where the LP signal is weak and the inversion did not fit the profiles well were masked by black color in the bottom panels.

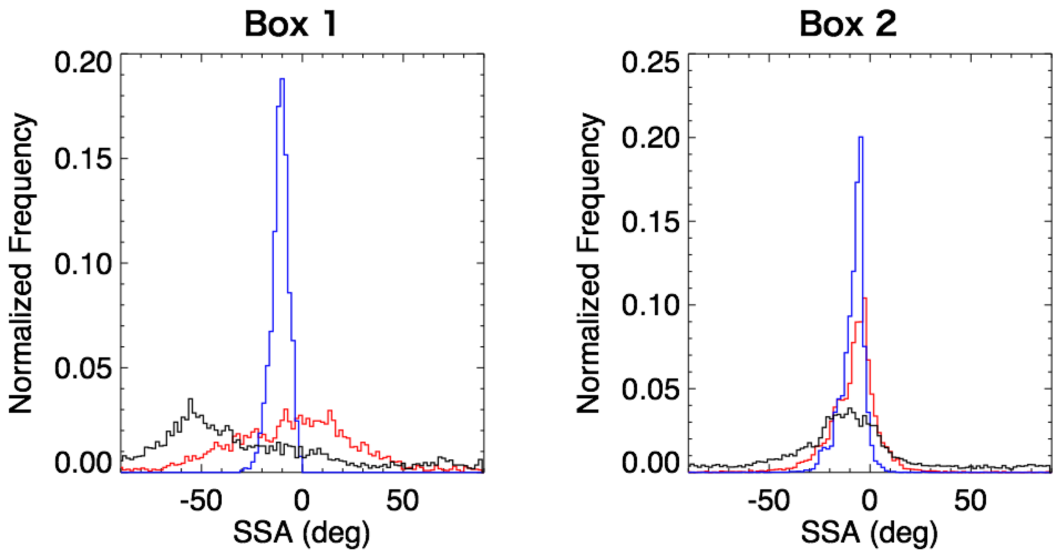

Figure 3.7: The histograms of the SSA in the box 1 and box 2 in Figure 3.6. The black, red, and blue solid lines show the SSA from the chromospheric magnetic field derived from He I 10830 Å, the photospheric magnetic field, the NLFFF at the 1500 km height, respectively.

while that in the photosphere is around 0 degree or small negative value. In the box 4, the photospheric magnetic field has less absolute value of the SSA peaked around 20 degree than the chromospheric observation peaked around 40 degree. For all 4 cases, magnetic field in the chromosphere has larger non-potentiality than that in the photosphere.

3.4.2 Comparison with Nonlinear Force-Free Field at the Chromospheric Height

In this section, for both NOAA 10969 and NOAA 11861, the chromospheric magnetic field derived from spectropolarimetric observations is compared with extrapolated magnetic field from the photosphere.

Regarding NOAA 10969, the upper right panel and lower left panel in Figure 3.5 show the potential field at the 1500 km above the photosphere derived from the observed photospheric field and the NLFFF at the 1500 km above the photosphere derived from the observed photospheric field, respectively. The result of the NLFFF at the 1500km

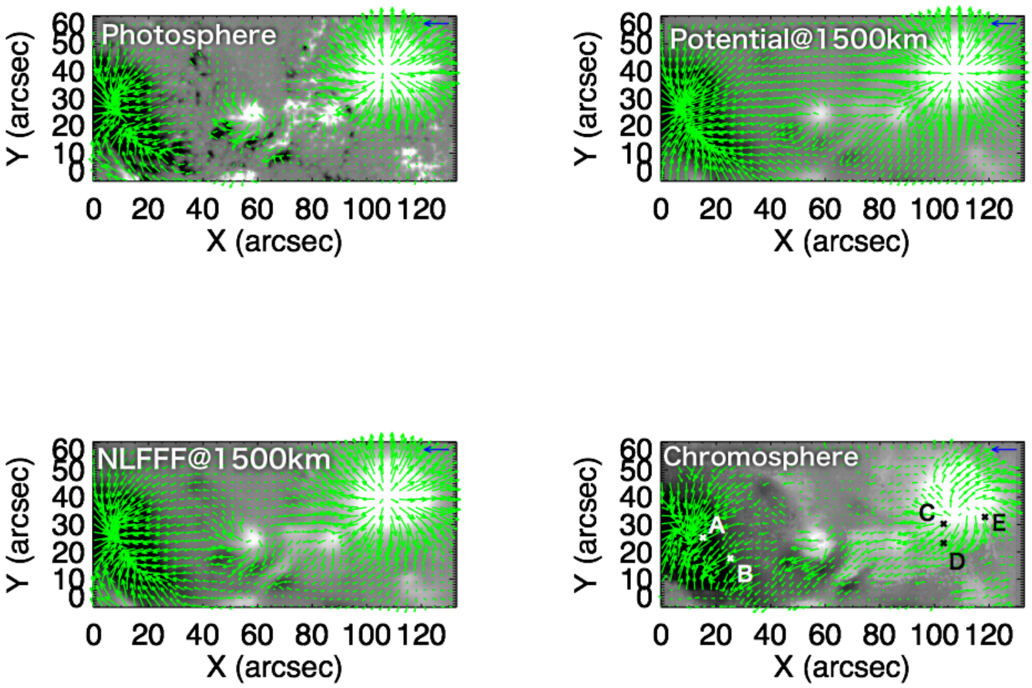

Figure 3.8: Vector magnetic field distributions in NOAA 11861. The gray scale shows the vertical magnetic field and the green arrows show the horizontal magnetic field. The length of blue arrow shows the field strength of 1500 G. Upper Left: Photospheric magnetic field observed with *SDO*/HMI. Upper right: Potential field at 1500 km height. Lower left: NLFFF at 1500 km height. Lower right: Chromospheric magnetic field observed with DST/FIRS.

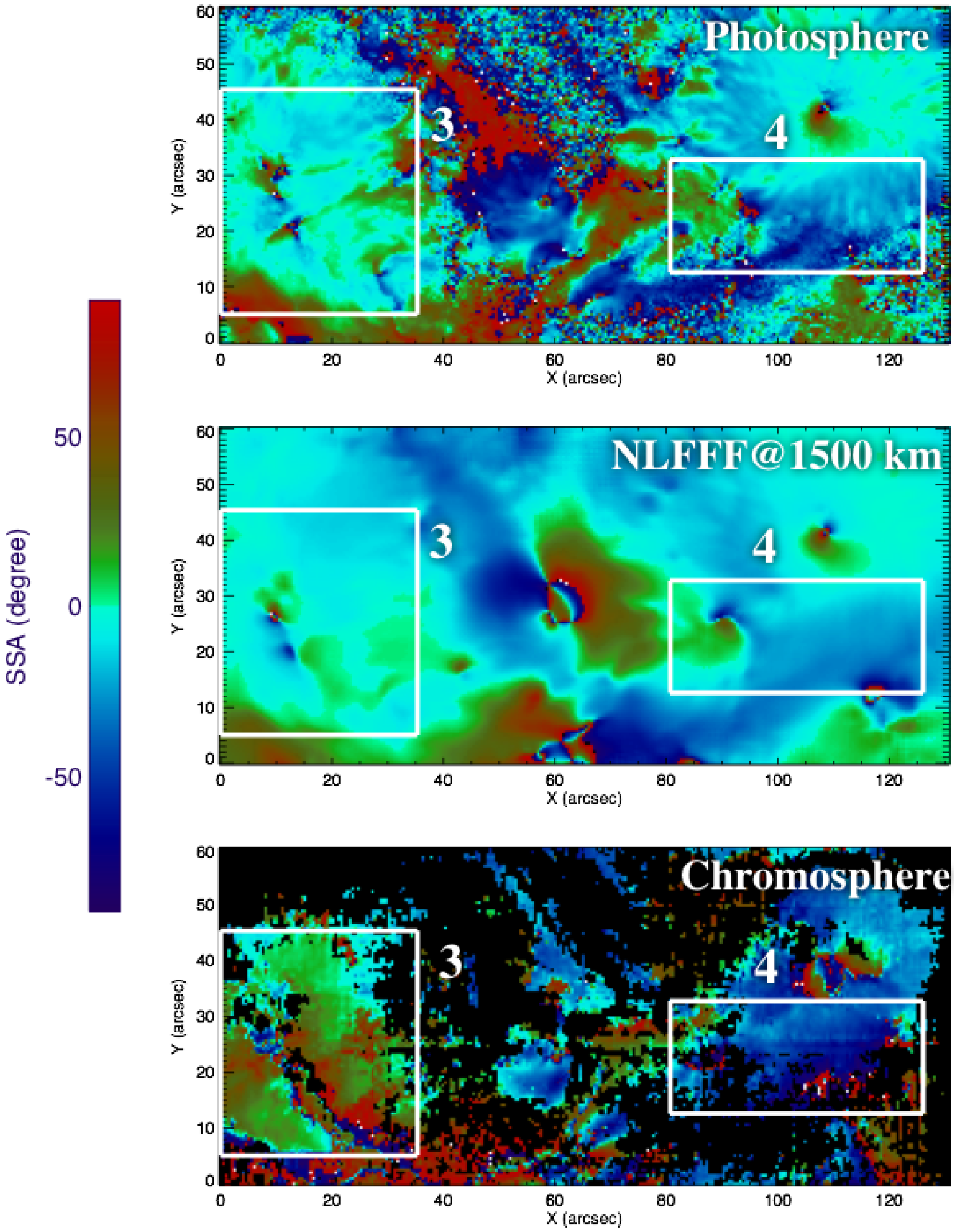

Figure 3.9: The spatial distribution of signed shear angle (SSA) for NOAA 11861. From the top to the bottom for the photosphere, NLFFF at 1500km, chromosphere (He I 10830 Å). The regions where the LP signal is weak and the inversion did not fit the profiles well were masked by black color in the bottom panels.

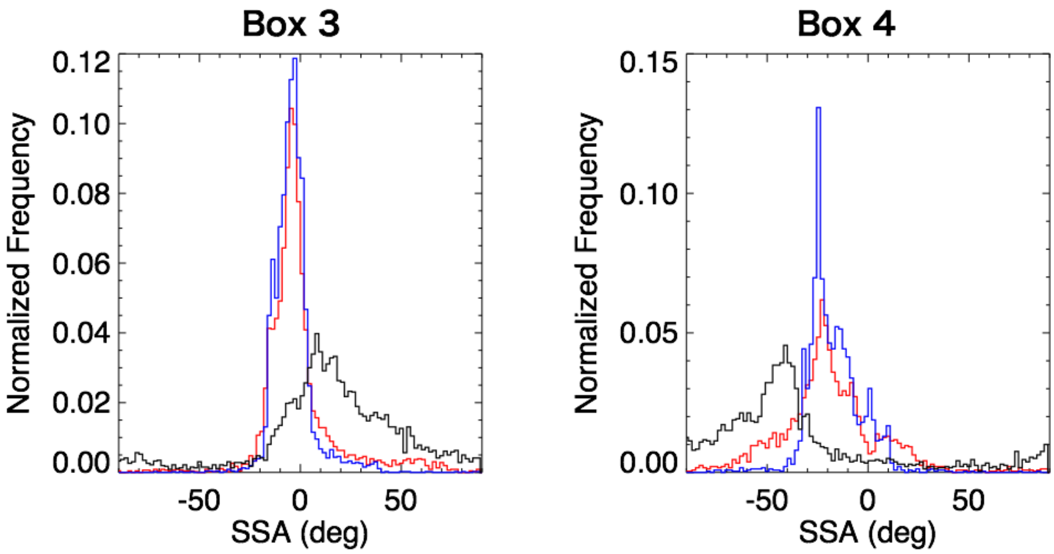

Figure 3.10: The histograms of the SSA in the box 3 and box 4 in Figure 3.9. The black, red, and blue solid lines show the SSA from the chromospheric magnetic field derived from He I 10830 Å, the photospheric magnetic field, the NLFFF at the 1500 km height, respectively.

height shows similar horizontal magnetic field as the potential field. The similarity of the NLFFF with the potential field may come from small non-potentiality at the photospheric height. However, the chromospheric magnetic field derived by inverting He I 10830 Å shows non-potential magnetic field vector especially in the region between the positive and negative polarities, which also can be seen in the comparison between EUV image and NLFFF in Section 3.4.3. Figure 3.11 shows the number density of the relation between the strength of the vector magnetic field (B_x, B_y, and B_z) from NLFFF at 1500 km height above the photosphere and chromospheric magnetic field derived from the He I 10830 Å observation. The white solid line is the line whose slope is 1. A good correlation in B_z can be seen and the Pearson correlation coefficient $C = 0.94$. The absolute values of B_z derived from the He I data are slightly smaller than that from the NLFFF. On the other hand, the horizontal magnetic field (B_x and B_y) shows comparatively weaker correlations, $C = 0.77$ and 0.69. Where B_x (from He I 10830 Å)< -500 G, the strength of B_x is larger than that from NLFFF. Similarly, where B_y (from He I 10830 Å)> 500 G, the strength of B_y is larger than that from NLFFF. The strong horizontal magnetic field

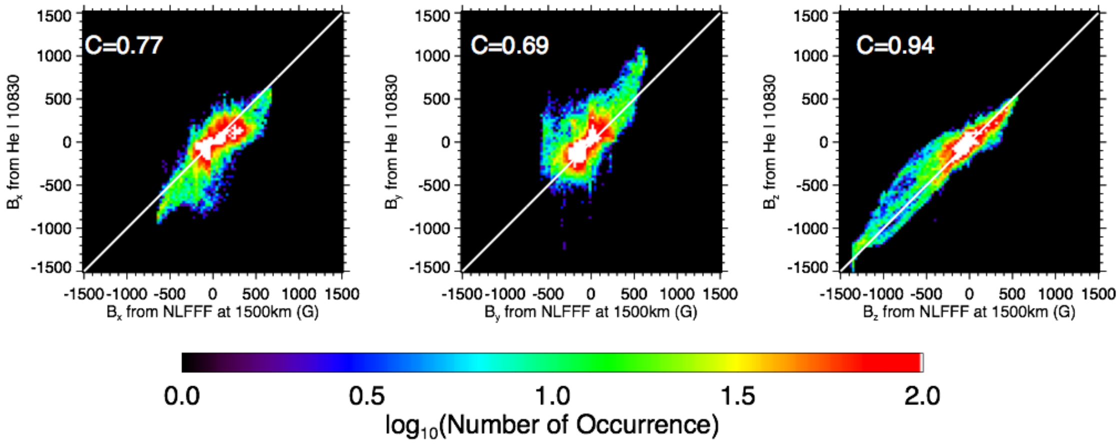

Figure 3.11: The number density plots of the relation in B_x, B_y, and B_z between NLFFF at 1500 km height and chromospheric magnetic field derived from He I 10830 Å in NOAA 10969.

(> 500 G) are located at the outer part of the sunspot. These results show that the outer part of the sunspot have the stronger horizontal magnetic field than that derived from the NLFFF modeling. Similar as Section 3.4.1, the non-potentiality of the NLFFF is evaluated by the SSA. The middle panel of Figure 3.6 shows the SSA of the NLFFF at 1500 km height. The SSA in the chromosphere derived from He I 10830 Å shows quite different distribution from that of NLFFF. The blue solid line in Figure 3.7 show the histogram of the SSA of the NLFFF at 1500 km height in the box 1 and box 2. The relation between the NLFFF at 1500 km height and chromospheric magnetic field derived from He I 10830 Å observations is similar to that between photospheric and chromospheric magnetic field. While the SSAs in the chromosphere in the box 1 are around -50 degree, the SSAs of NLFFF at the 1500 km are around -10 degree. The SSAs in the chromosphere and those of the NLFFF at 1500 km have a similar peak around 0 degree in the histogram in the box 2. While the SSAs in the chromosphere in the box 2 have broad distribution, those of the NLFFF are concentrated around 0 degree.

For NOAA 11861, the upper right panel and lower left panel in Figure 3.8 show the potential field at the 1500 km above the photosphere derived from the observed photospheric field and the NLFFF at the 1500 km above the photosphere derived from the observed photospheric field, respectively. While the NLFFF at the 1500km height shows similar horizontal magnetic field as the potential field, small deviations can be identified around the center of the ROI, $(x, y) \sim (50, 20)$. In a comparison between chromospheric field from He I 10830 Å and extrapolated field, there exists clear difference. While the positive leading spot in the west side of the FOV shows clear clockwise twist in the horizontal field from He I 10830 Å, that from NLFFF does not show the twisted distribution. Figure 3.12 shows the number density distribution in B_x, B_y, and B_z of the relation between NLFFF at 1500 km height and chromospheric magnetic field derived from He I 10830 Å. As similar to NOAA 10969, B_z shows a better correlation ($C = 0.98$) and horizontal magnetic fields show weaker correlations ($C = 0.76$ and 0.70 for B_x and B_y), respectively. In the strong vertical magnetic field region ($|B_z| > 1000$ G), the NLFFF tends to show stronger field. Regarding horizontal magnetic field, there is no systematic deviation, which is also identified in the case of NOAA 10969.

The histogram of the SSA of the NLFFF at 1500 km is shown by the blue solid line in Figure 3.10. The histogram of the NLFFF at 1500 km height is similar to that of the photospheric magnetic field. In the box 3, the SSAs in the chromosphere have mainly positive value while that of NLFFF is around 0 degree or small negative value. In the box 4, the NLFFF at 1500 km height has less absolute value of the SSA peaked around 20 degree than the chromospheric observation peaked around 40 degree.

For all 4 boxes in NOAA 10969 and NOAA 11861, the NLFFF underestimated the non-potentiality at the height of the chromosphere.

3.4.3 Comparison with NLFFF and Coronal Loop Structures

Figure 3.13 shows the qualitative comparison of coronal field lines in NOAA 10969. The upper left panel shows an EUV image of the NOAA 10969 observed with *TRACE* at 171 Å. The yellow lines in the panel are magnetic field lines manually selected by the visual inspection. The upper right panel shows the vertical magnetic field in the photosphere

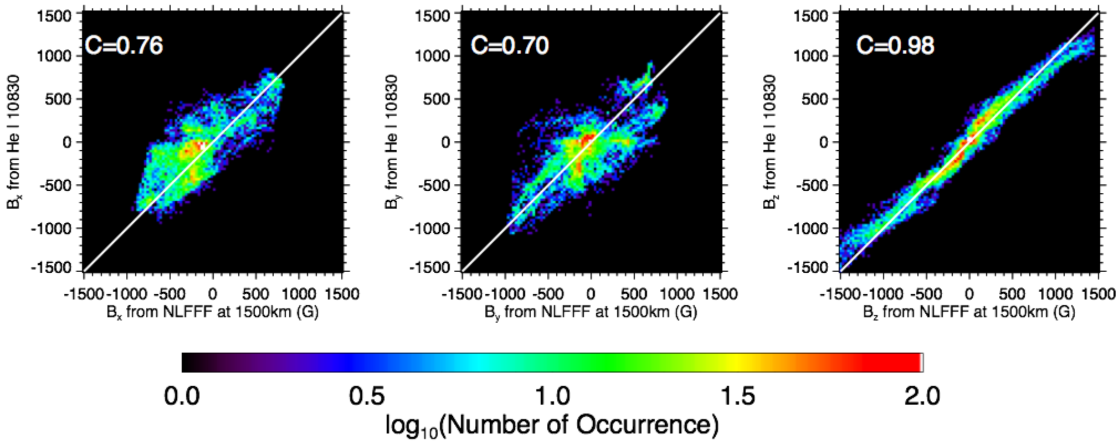

Figure 3.12: The number density distribution in B_x, B_y, and B_z of the relation between NLFFF at 1500 km height and chromospheric magnetic field derived from He I 10830 Å in NOAA 11861.

obtained with *Hinode* SOT/SP with the same FOV. The green solid lines overlaid on the *TRACE* image in the lower panels show field lines estimated from potential field (bottom left) and NLFFF (bottom right). The field lines are randomly selected in the calculation box. The field lines of NLFFF seems to show similar morphology with those of the potential field. Focusing on the field lines in the yellow box, however, the deviation can be seen between the EUV image and extrapolated fields. While the field lines of the potential field and NLFFF in the yellow box almost parallel to the X-axis, those of EUV image represented by the yellow lines are inclined with respect to X-axis. The similar deviation is clearly seen in the chromospheric height, which is shown in Section 3.4.4.

Figure 3.14 shows the qualitative comparison of coronal field lines in NOAA 11861. The upper left panel shows an EUV image of the NOAA 11861 observed with *SDO*/AIA at 171 Å. The yellow lines in the panel are two magnetic field lines manually selected by visual inspection. The upper right panel shows the vertical magnetic field in the photosphere obtained with *SDO*/HMI with the same FOV. The green solid lines overlaid on the *SDO*/AIA image in the lower panels show field lines estimated from potential field (bottom left) and NLFFF (bottom right). Unlike the case of NOAA 10969, the potential field and NLFFF of NOAA 11861 show clear difference in the yellow box. The field lines

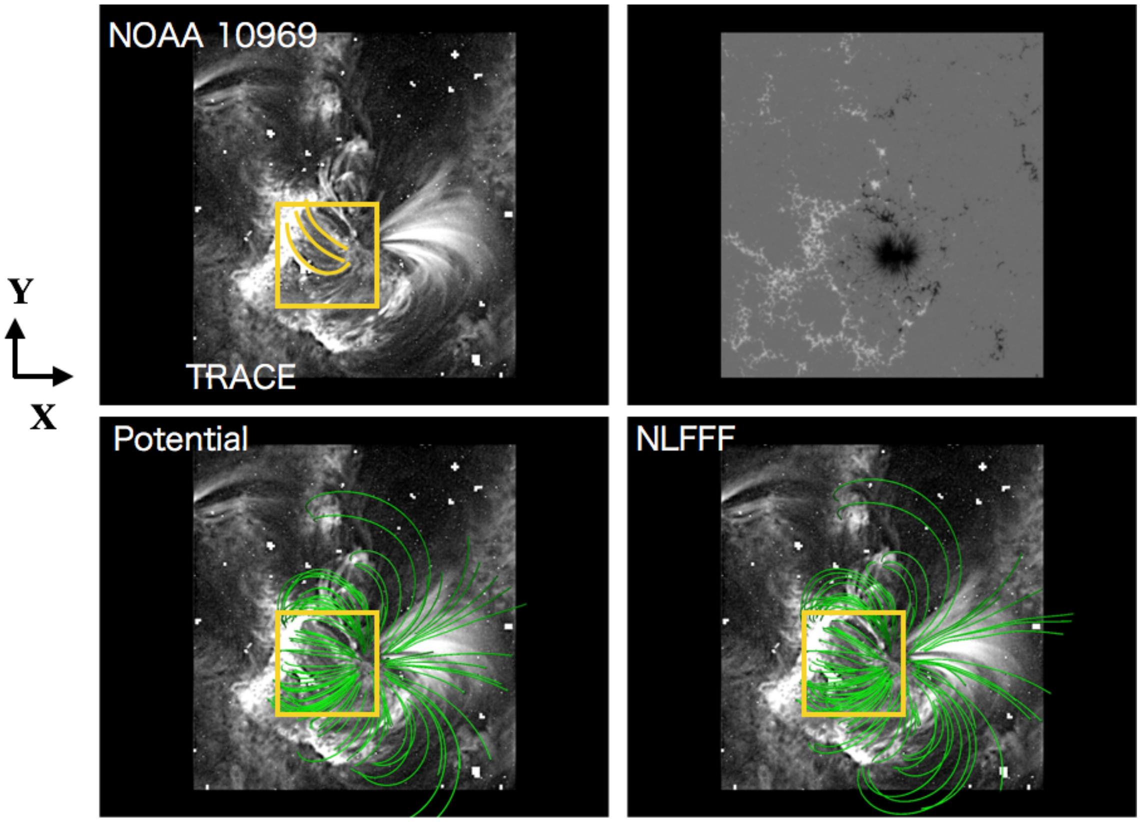

Figure 3.13: The upper left panel shows the EUV image of NOAA 10969. The yellow lines in the panel are manually selected field lines by the visual inspection. The upper right panel shows the vertical magnetic field in the photosphere obtained with *Hinode* SOT/SP with the same FOV. The green solid lines in lower panels show the field lines calculated by the potential field and NLFFF extrapolation, respectively.

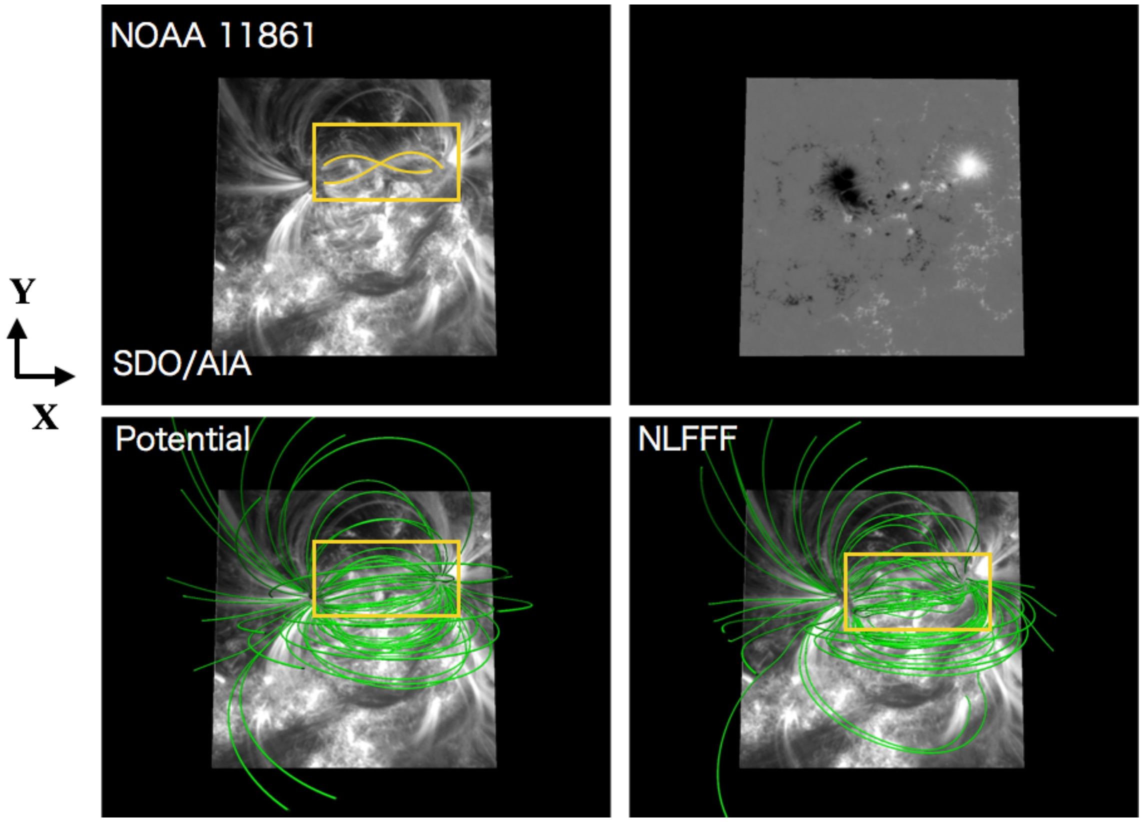

Figure 3.14: The upper left panels show the EUV images of NOAA 11861. The yellow lines in the panel are manually selected field lines by the visual inspection. The upper right panel shows the vertical magnetic field in the photosphere obtained with *SDO* HMI with the same FOV. The green solid lines in bottom panels show the field lines calculated by the potential field and NLFFF extrapolation.

of NLFFF show twisted structure in the yellow box, while those of potential field do not. As shown by the yellow lines in the upper right panel, the two field lines in the EUV image show similar twist structure. This result indicates that the NLFFF reproduces the 3D structures well in the qualitative sense.

3.4.4 Relation between Chromospheric Vector Magnetic Fields and Fibril Structures

In this section, we validate the inversion results around the region by using fibril structures, which can be seen in the line core of He I 10830 Å. As seen in the upper middle panel of Figure 3.1, dark fibril structures are found around the sunspot at the line core of He I 10830 Å. We assume that magnetic field vector is aligned with the fibril structures. Although theoretical and observational studies suggest that magnetic field vector sometimes does not align with fibril structures due to partially ionized effect (de la Cruz Rodríguez & Socas-Navarro, 2011; Martínez-Sykora et al., 2016), other observational studies show that the fibril structures are often well aligned with magnetic field (Schad et al., 2013; Asensio Ramos et al., 2017). As shown in Section 3.4.2, chromospheric magnetic field shows different azimuth angles from the results of NLFFF in the region between positive and negative polarities in NOAA 10969. Although the deviation can also be seen in other areas such as box 2, 3, and 4 in Figures 3.6 and 3.9, these regions are located around sunspots and then we focus on the box 1 region in this section. Figure 3.15 shows the relation between magnetic field vector and chromospheric features. The 2D image in the upper panel was created with peak intensity at the line core of He I 10830 Å. Four green lines show the fibril structures automatically detected by the OCCULT-2 code (Aschwanden et al., 2013). Lower four panels show the angle between the fibril structure and magnetic field vector along each fibril structure. Black lines with asterisks, blue, and red lines show angles made by fibril structures with the chromospheric magnetic field (He I 10830Å), the NLFFF at 1500 km, and the potential field at 1500 km, respectively. Except for fibril 1, magnetic field vectors derived from He I 10830 Å are well aligned to the fibril structure. However, the NLFFF and potential field are not aligned with fibrils 1, 3, and 4. In Fibril 3 and 4, misalignment is 30-50 degrees.

3.4.5 dependence of Height, Step Number and Initial Condition

Although the formation layer of He I 10830 Å is considered to be thin as described in Section 1.5.2, the formation height of He I 10830 Å may vary 800km-2000km at each location in active regions. Although the comparison was performed at 1500km height in Section 3.4.4, there is a possibility that the formation height is different from 1500km height above the photosphere and the comparison is not appropriate. Figure 3.16 shows

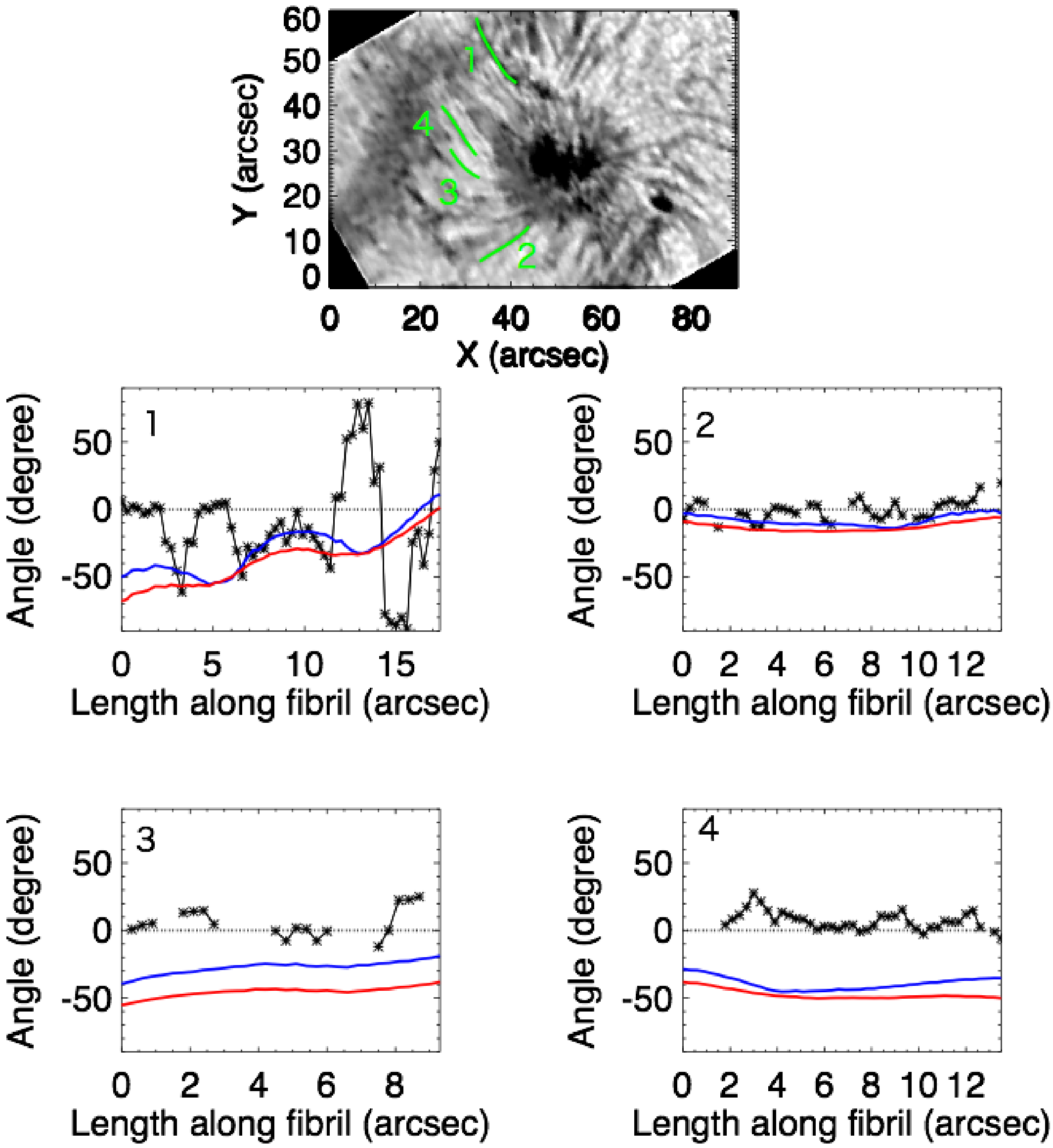

Figure 3.15: Upper panel: The line core image of He I 10830 Å. Four green lines show the fibril structures automatically detected by OCCULT-2 code (Aschwanden et al., 2013). Lower four panels: The angle between the fibril structures and magnetic field vector along the fibril structures. Black lines with asterisks, blue, and red lines show angles made by fibril structures with the chromospheric magnetic field (He I 10830Å), the NLFFF at 1500 km, and the potential field at 1500 km, respectively.

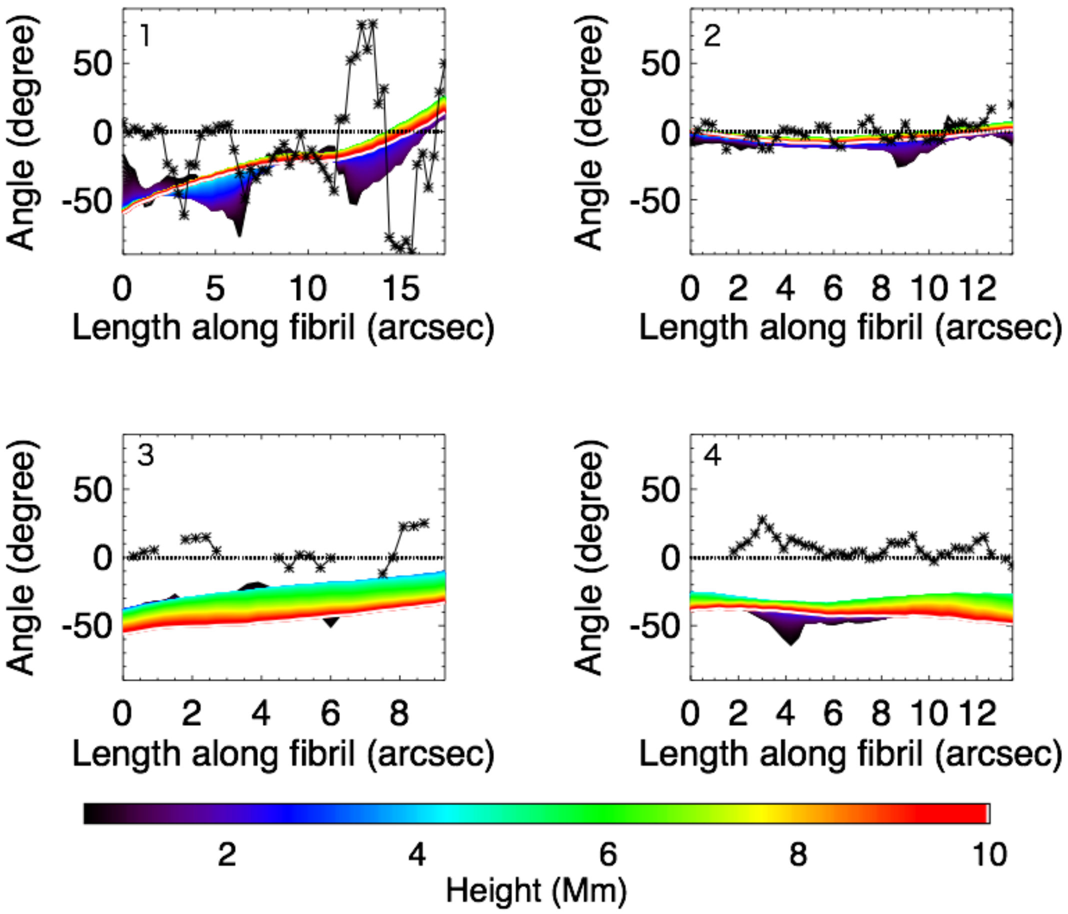

Figure 3.16: Similar to Figure 3.15, each panel shows the angle between magnetic field vector and fibril structures. Color shows the angle between NLFFF at the height of 0-10 Mm and fibril structures. Black solid lines with starts show the angle between magnetic field vector from He I 10830 Å and the fibril structures.

the comparison between fibrils and NLFFF at the height between 0 and 10 Mm. Color shows the angle between NLFFF at the height of 0-10 Mm and fibril structures. Black solid lines with asterisks show the angle between magnetic field vector from He I 10830 Å and the fibril structures. In fibrils 3 and 4, there are also deviations in the upper height, which means that the deviation is not due to the inappropriate choice of the comparison height.

Figure 3.17 shows how the NLFFF results depend on the iteration number, initial condition, top boundary, and spatial resolution dependence of the NLFFF results. Each panel shows the alignness of magnetic field vector focusing on fibril 4 in Figure 3.15. The upper left panels show the results from iteration number of 0 (potential field, black), 10000 (yellow), 20000 (red), 30000 (green), and 40000 (blue) steps. There is almost no difference between 30000 and 40000, which suggests that the calculation nearly converges. The upper right panel shows the misalignment of the NLFFF along the fibril when the different initial condition is used in the modeling. We chose the initial condition such that the magnetic field vector is well aligned to the fibril structure (black line). However, when the NLFFF calculation proceeds (from the black line to the blue line), the magnetic field vector tends to deviate from the angle of the fibril structure. The lower panel shows the dependence of the height of the top boundary and the spatial resolution on the NLFFF modeling. While the black solid line shows the result of $z_{\rm top} = 0.25$ resolved by 504 grids, the black dotted line shows the result of $z_{\rm top} = 0.50$ resolved by 504 grids. The difference between solid and dotted lines is not large (less than 10 degree).

3.4.6 Inversion Results of HAZEL

Figures 3.18, 3.19, 3.20, 3.21, 3.22, 3.23, and 3.24 show some examples of the observed Stokes profiles with HAZEL fitting results. The asterisks show the observational profiles and red solid lines show the synthesis profiles. Each pixel is located in the regions A and B in Figure 3.5, and the regions A, B, C, D, and E in Figure 3.8, which shows deviation compared to NLFFF. The inversion result shows good fits in each Stokes profile. In the linear polarization signals (Stokes Q and U), we can identify two kinds of signals. One is transverse Zeeman dominated signal at the pixel where the strong transverse magnetic field exist. When the polarization signal is dominated by the transverse Zeeman effect, Stokes Q and/or U show both negative and positive signal in the wavelength range of one spectral line, which can be seen in Figures 3.21, 3.22, and 3.24. The other signal is joint action of Zeeman and Hanle effects. In case of the joint action of Zeeman and Hanle effects, the linear polarization signal shows one signs, which can be seen in Figures 3.18,

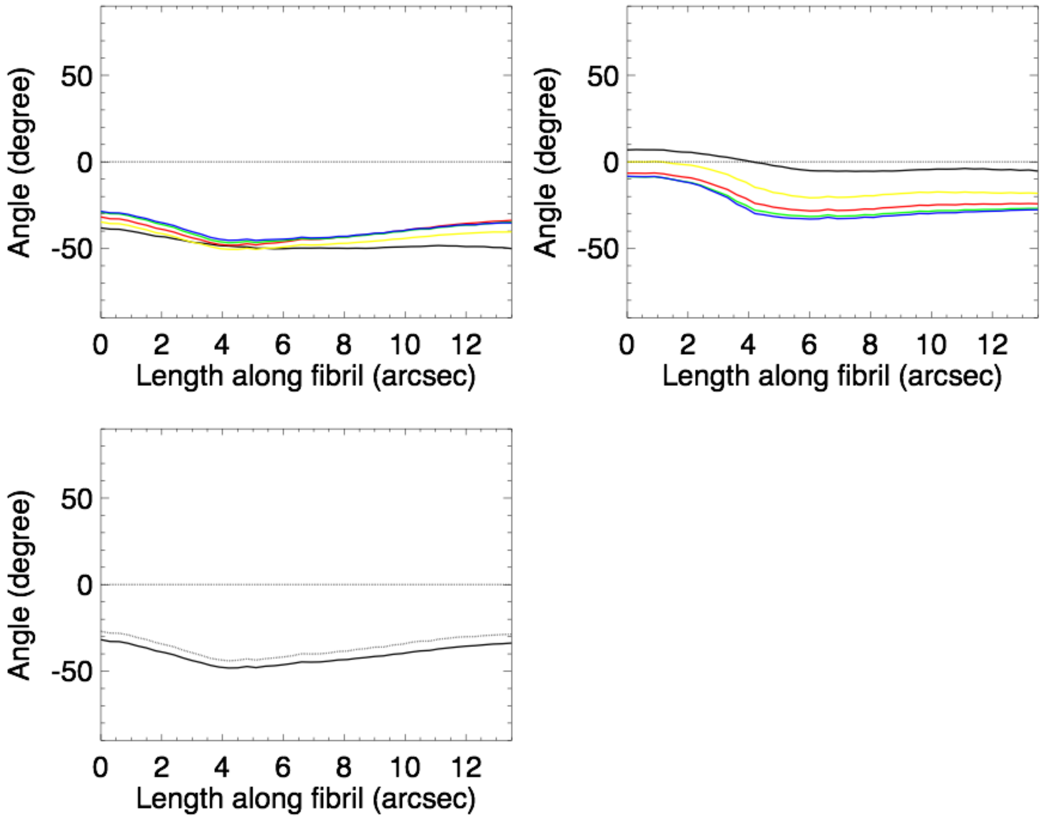

Figure 3.17: The alignness of magnetic field vector focusing on fibril 4 in Figure 3.15. Upper panels:The results from iteration number of 0 (potential field, black), 10000 (yellow), 20000 (red), 30000 (green), and 40000 (blue) steps. Upper left panel is the NLFFF modeling from the potential field and upper right panel is that from the linear force-free field. Lower: The black solid line shows the result of $z_{\rm top} = 0.25$ resolved by 504 grids and the black dotted line shows the result of $z_{\rm top} = 0.50$ resolved by 504 grids.

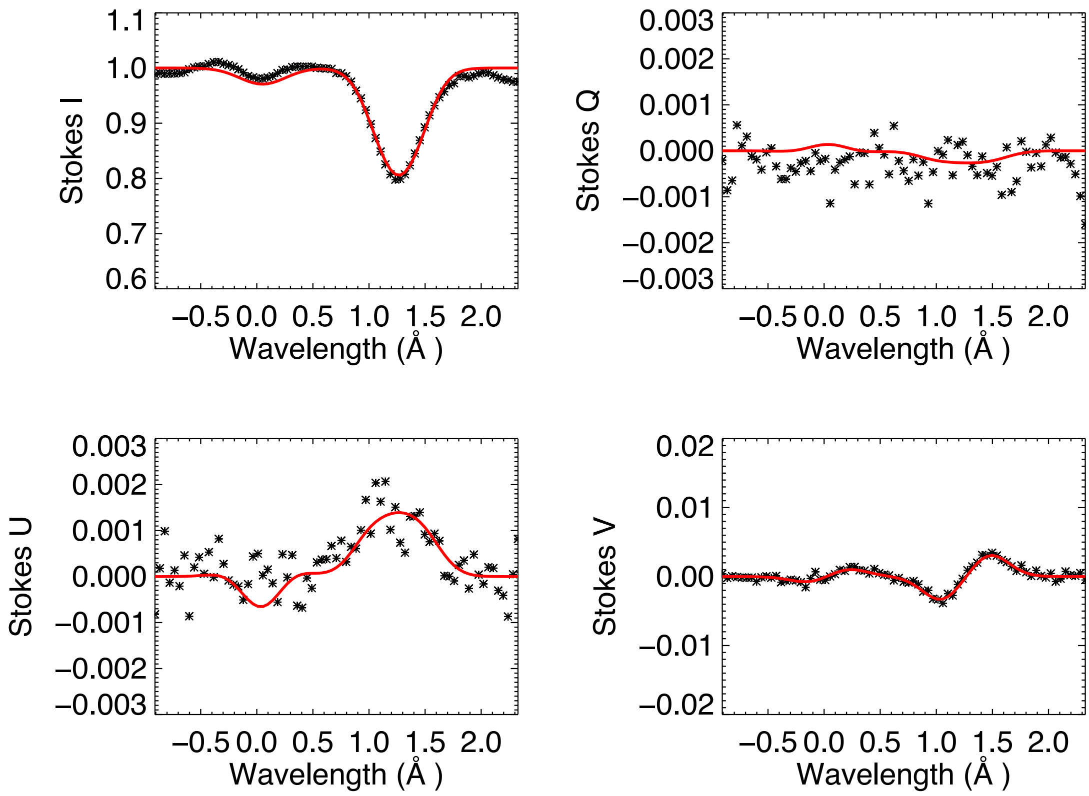

Figure 3.18: Stokes vectors of region A in Figure 3.5. Red solid lines show the result of inversion by HAZEL. The zero in the horizontal axis corresponds to 10829.0911Å.

3.19, 3.20, and 3.23. Whether the linear polarization is dominated by transverse Zeeman or joint of Zeeman and Hanle is important when we discuss the ambiguity of the transverse magnetic field. The ambiguity of our results of magnetic field vector will be discussed in Section 3.5.

3.5 Discussions

The vector magnetic field observations at both photospheric and chromospheric height in Figures 3.5, 3.8, 3.6, and 3.9 show that the observed chromospheric magnetic field may have larger non-potentiality than photospheric magnetic field. Joshi et al. (2017) also investigated photospheric and chromospheric magnetic fields of two sunspots by using Si I 10827 Å and He I 10830 Å. They analyzed vector magnetic field in both layers

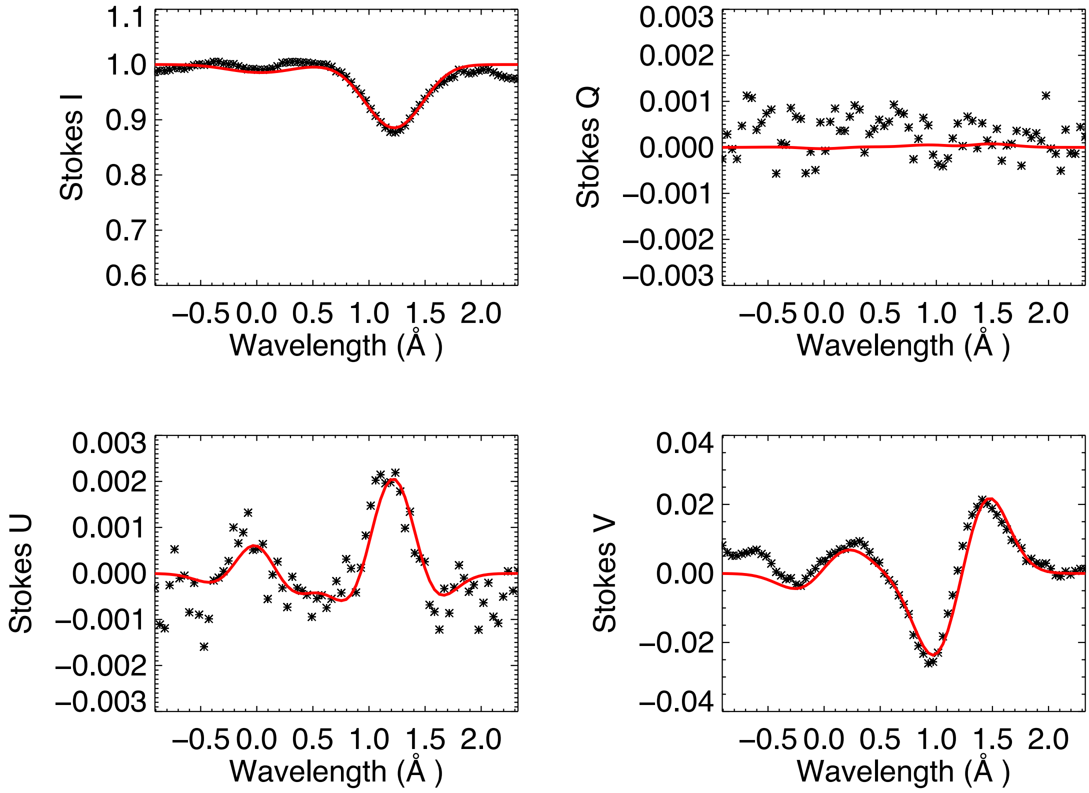

Figure 3.19: Stokes vectors of region B in Figure 3.5. Red solid lines show the result of inversion by HAZEL. The zero in the horizontal axis corresponds to 10829.0911Å.

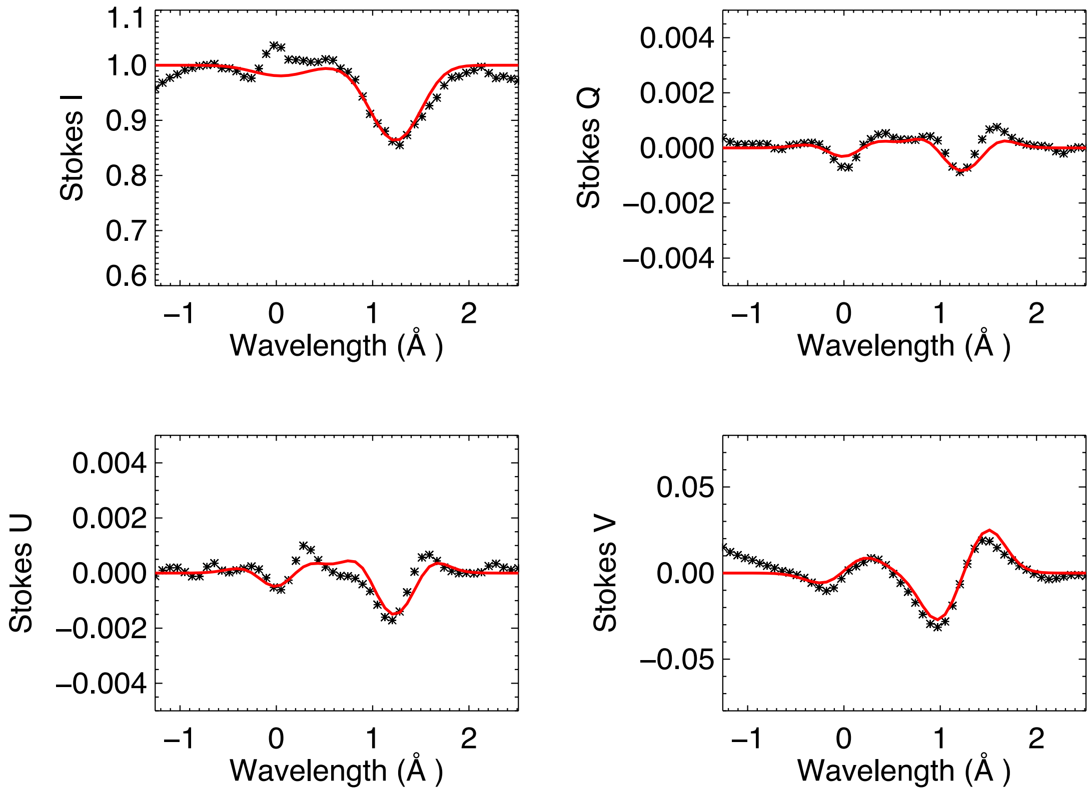

Figure 3.20: Stokes vectors of region A in Figure 3.8. Red solid lines show the result of inversion by HAZEL. The zero in the horizontal axis corresponds to 10829.0911Å.

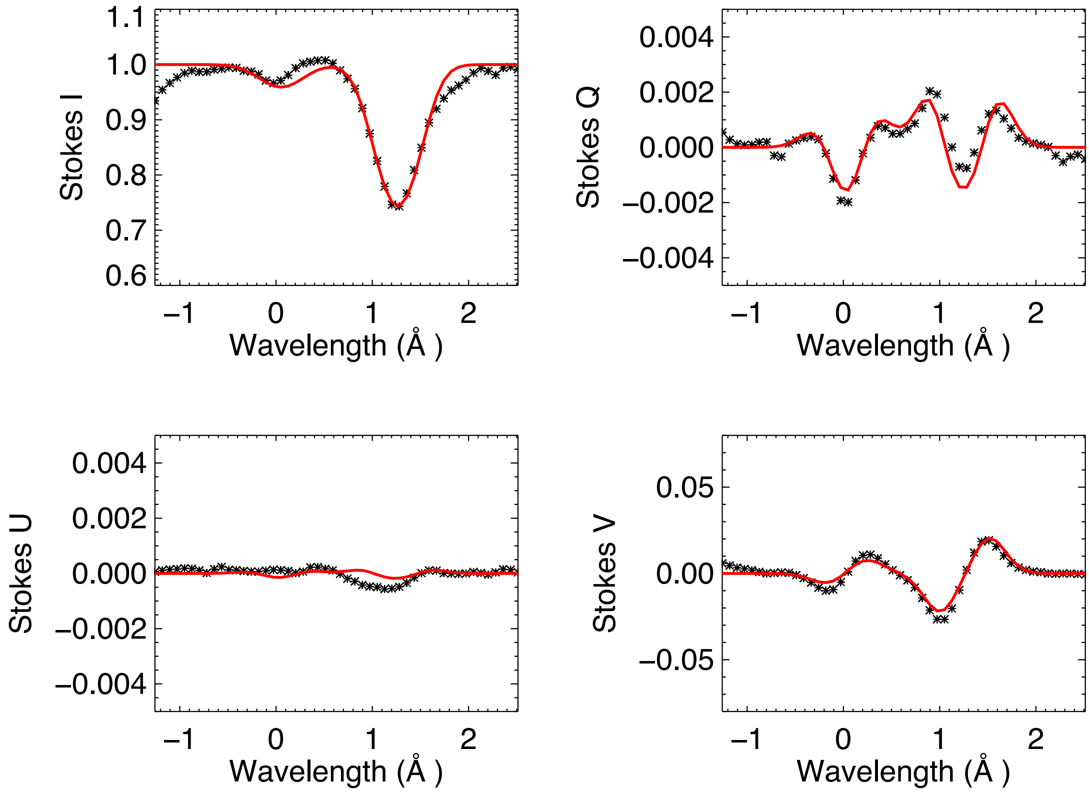

Figure 3.21: Stokes vectors of region B in Figure 3.8. Red solid lines show the result of inversion by HAZEL. The zero in the horizontal axis corresponds to 10829.0911Å.

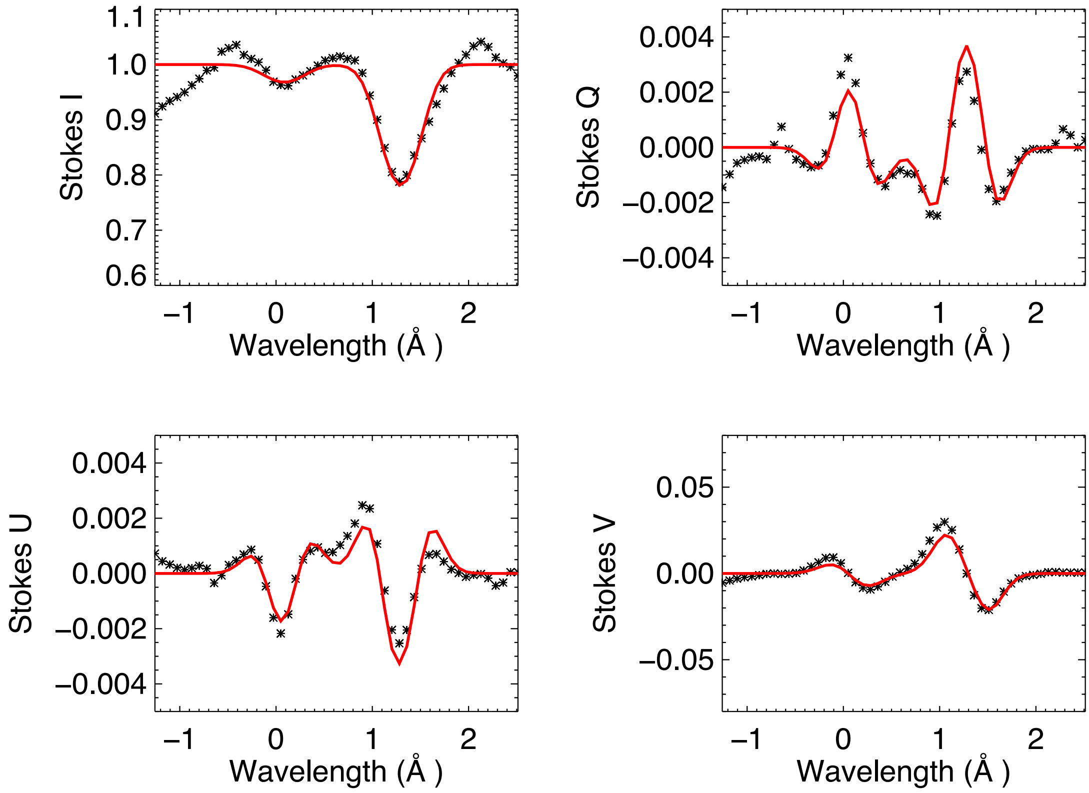

Figure 3.22: Stokes vectors of region C in Figure 3.8. Red solid lines show the result of inversion by HAZEL.

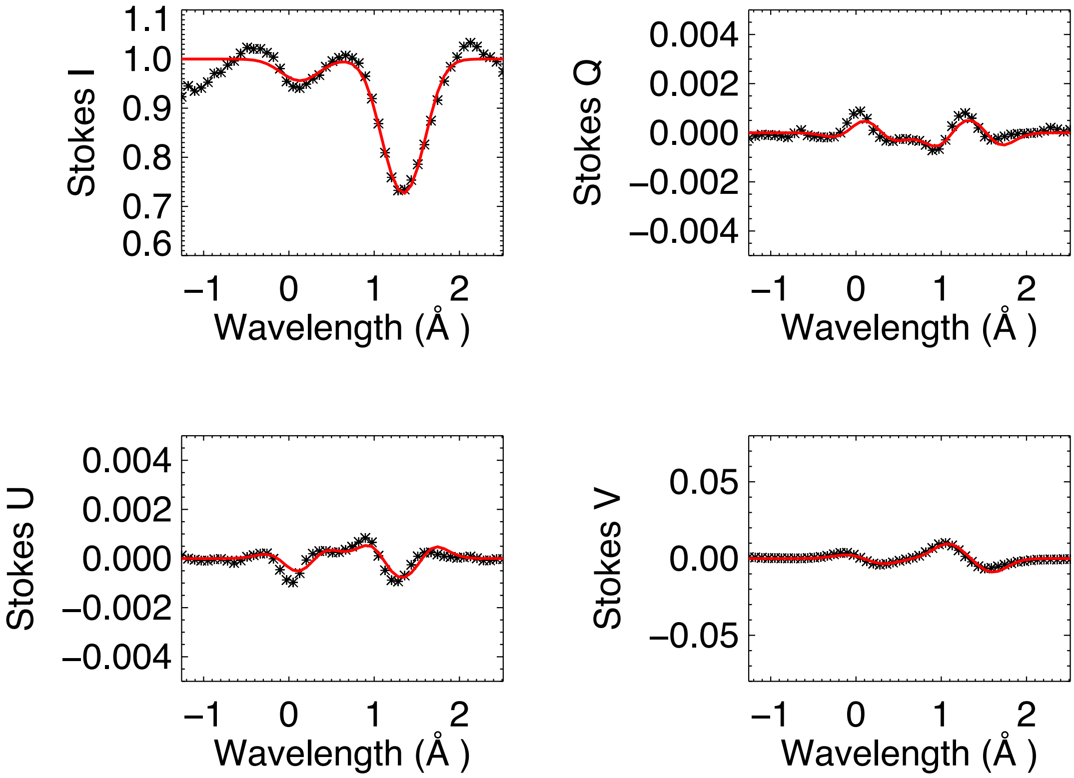

Figure 3.23: Stokes vectors of region D in Figure 3.8. Red solid lines show the result of inversion by HAZEL. The zero in the horizontal axis corresponds to 10829.0911Å.

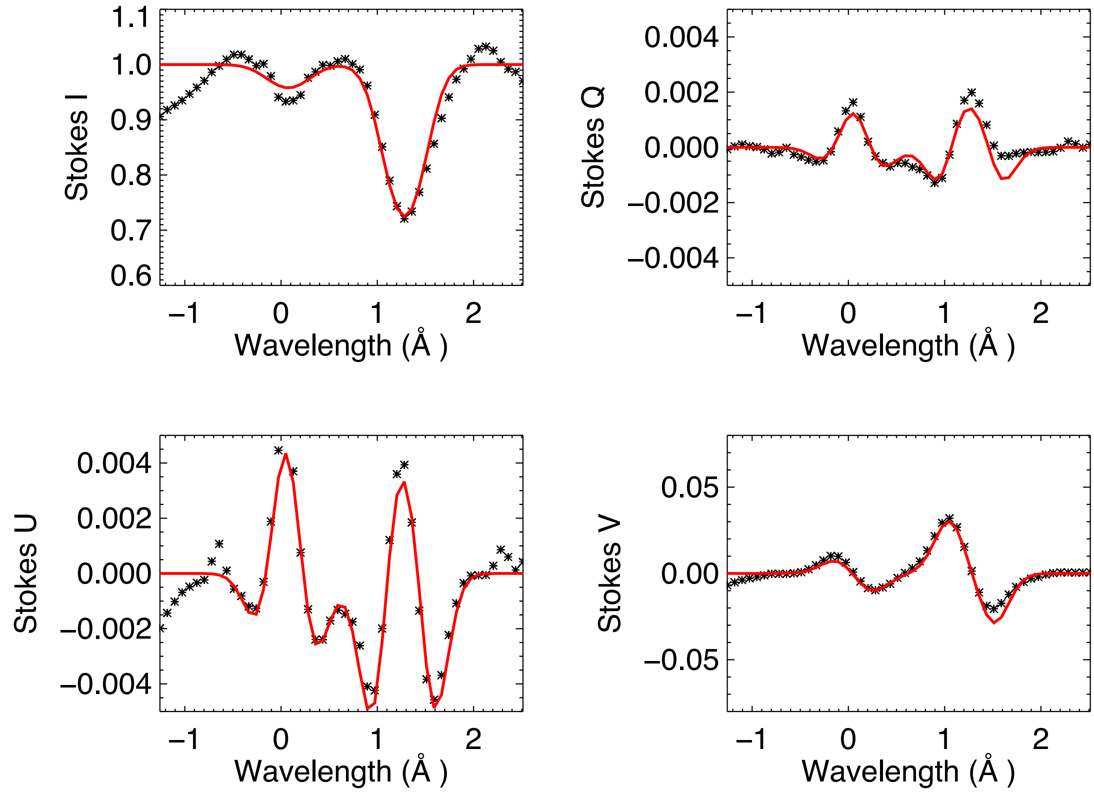

Figure 3.24: Stokes vectors of region E in Figure 3.8. Red solid lines show the result of inversion by HAZEL. The zero in the horizontal axis corresponds to 10829.0911Å.

only in two simple round sunspots and suggested a possibility that the chromospheric magnetic field has large twist compared to photospheric magnetic field. Our study has extended their view by examining the entire active regions, not restricted to a simple sunspot. Large FOV observations allow us to identify twisted structures more clearly as shown in Figures 3.5 and 3.8. Yelles Chaouche et al. (2012) tried to extrapolate the 3D magnetic field from both the photosphere and chromosphere. While they performed qualitative comparison of the 3D structure of the field lines, we quantitatively compared the non-potentiality of the magnetic field measured by the SSA between the NLFFF modeling and chromospheric magnetic field observations. Compared with the measurements of the chromospheric magnetic field, we revealed that the NLFFF modeling may underestimate the non-potentiality both in active regions NOAA 10969 and 11861, as shown in Figures 3.5, 3.8, 3.6, and 3.9.

There are two possibilities to cause the underestimation of the non-potentiality by using NLFFF modeling. One can be due to the vertical gas pressure gradient in the lower atmosphere. Parker (1974) investigated radial expansion of the magnetic flux tube due to the decrease of the gas pressure with height, as shown in Figure 3.25. The conservation of the longitudinal magnetic flux gives

$$B_{lz} r dr = B_{uz} R dR, \tag{3.4}$$

where B_{lz} and B_{uz} are the longitudinal magnetic field at the lower and upper atmosphere, respectively, and r and R are the radial distances from the axis at the lower and upper atmosphere, respectively. The conservation of the torque of the azimuthal Maxwell stress gives,

$$r(B_{l\phi} B_{lz}) r dr = R(B_{u\phi} B_{uz}) R dR, \tag{3.5}$$

where $B_{l\phi}$ and $B_{u\phi}$ are the azimuthal magnetic filed at the lower and upper atmosphere, respectively. From these two equations, we can calculate the effect on the number of the

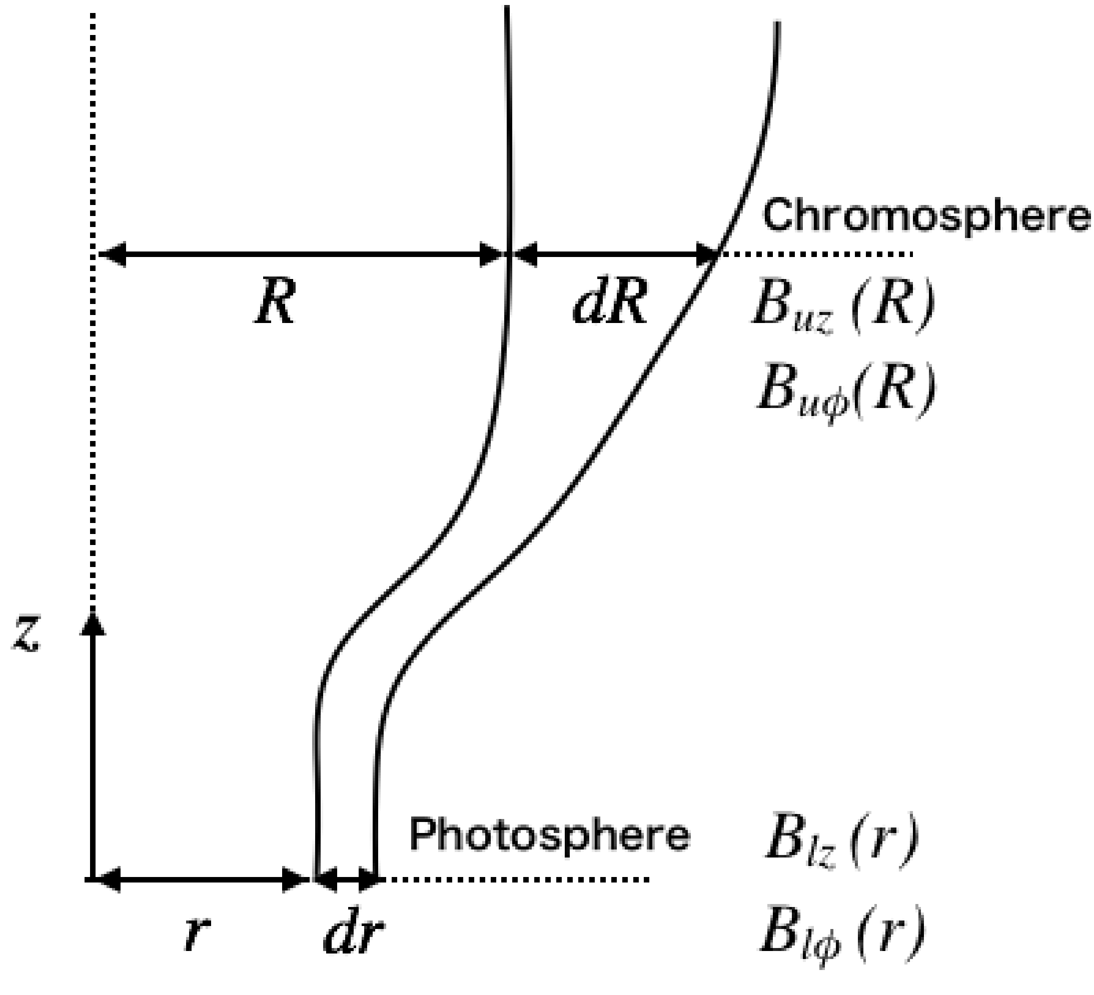

Figure 3.25: Sketch of the expansion of the magnetic flux tube. Solid lines show the magnetic field lines.

turn of the magnetic flux tube,

$$\begin{aligned} \frac{T_u}{T_l} &= \frac{B_{u\phi}/(2\pi R B_{uz})}{B_{l\phi}/(2\pi r B_{lz})}, \\ &= \frac{r}{R}\frac{dR}{dr}, \end{aligned} \tag{3.6}$$

where T_u and T_l are the number of turns per unit length for torsional equilibrium at the upper and lower atmosphere, respectively. Assuming that the expansion rate of the flux tube becomes larger at the large radius, $R/r < dR/dr$, the number of turns per unit length becomes larger at the upper atmosphere, $T_u/T_l > 1$. This means that the expansion of the flux tubes increases the non-potentiality at the chromospheric height and suggests that the gas pressure significantly affects the magnetic field even in active regions. Since NLFFF calculation is based on the photospheric magnetic field in this study, the effect of expansion of the magnetic flux tubes can not be reproduced. This is one of the reasons why the NLFFF result underestimated the chromospheric non-potentiality.

The other cause is the uncertainty in the magnetic field observation of the photospheric layer in the penumbral regions. Title et al. (1993) showed that the inclination of penumbral magnetic field has the azimuthal variation. Lites et al. (2002) reported that the magnetic field in the penumbral region has fluted structure based on the two component analysis. In our study, we inverted the photospheric lines Fe I 6301.5 Å and 6302.5 Å with one component Milne-Eddington atmosphere. This method might lead to the misunderstanding of the azimuth of the magnetic field in the penumbral region, where might have multi-component magnetic field in each pixel.

At the observational side, there is uncertainty in measurements of the chromospheric magnetic field because of insufficient photometric and polarimetry accuracy in many observations and ambiguity resolution of the field azimuth. The famous ambiguity is 180 degree ambiguity in the transverse Zeeman effect (Landi Degl'Innocenti & Landolfi, 2004). We can not distinguish 180 degree azimuthal ambiguity in the LOS reference frame from the spectropolarimetric observations with one spectral line. The second ambiguity is Van

Vleck ambiguity (Landi Degl'Innocenti & Landolfi, 2004; Asensio Ramos et al., 2008). The Van Vleck ambiguity occurs between the Hanle effect saturated regime and the transverse Zeeman dominated regime. In this regime, there appear four ambiguous solutions (two introduced by 180 degree ambiguity and two introduced by the Van Vleck ambiguity) with the measurements of Stokes Q, U, and V. The Van Vleck ambiguity will vanish when the linear polarization signals are dominated by the transverse Zeeman effect. The pixels such as in Figures 3.21, 3.22, and 3.24 are not suffered from Van Vleck ambiguity. In our analysis, we neglected the Van Vleck ambiguity in He I 10830 Å . Because we chose the azimuth which is close to the potential field, the 180 degree ambiguity dose not lead to the underestimation of the non-potentiality in our analysis at the Zeeman dominated pixels. At the pixels where the Van Vleck ambiguity may exist such as the pixel in Figure 3.18, the estimation of the non-potentiality has also ambiguity. We validated the azimuth of such pixels by comparing with fibril structures as shown in Figure 3.15.

3.6 Summary

We measured the chromospheric magnetic field by spectropolarimetric observations of He I 10830 Å. We also derived chromospheric magnetic field based on the NLFFF from the photospheric magnetic field and compared it with the chromospheric magnetic field derived from He I 10830 Å. Summarizing our findings in Chapter 3,

(1) The chromospheric magnetic field derived by the spectropolarimetric observations of He I 10830 Å shows more twisted magnetic field at some locations than the photospheric magnetic field does.

(2) The NLFFF extrapolation from the photospheric magnetic field underestimate the non-potentiality at the chromospheric height at some locations.

Chapter 4

General Discussion

In this chapter, we discuss the results shown in Chapters 2 and 3, and present their impact on the understanding of the 3D magnetic field structure in the solar active regions. We also discuss prospects of the future research.

4.1 Outcome of Thesis

Revisiting the purpose of this thesis, we attempted to reveal the distribution of non-potential field at the upper atmosphere and evaluated whether NLFFF extrapolations can predict it reasonably. The main results in Chapter 2 and 3 are (1) the initial condition dependence is small at the lower height, and (2) the chromospheric magnetic field may have larger non-potentiality than that estimated by the NLFFF extrapolation from the photosphere. Our results indicate that the NLFFF modeling underestimates the non-potentiality at the chromospheric height, even though the unique result is obtained at the lower height by the NLFFF extrapolation from the photospheric height. Since we found the underestimation of the NLFFF modeling at the chromospheric height, we propose that the non-potentiality in active regions may be larger than that previously estimated based on the NLFFF extrapolation not only in the chromosphere but also in the corona.

The quantitative estimation of the non-potentiality in the upper atmosphere is important in understanding the energy storage and the onset mechanism for solar flares. In terms of the energy storage, Sun et al. (2012) investigated the temporal evolution of the magnetic energy and free energy based on the NLFFF extrapolation from the photosphere. They showed that the magnetic free energy reaches a maximum of $\sim 2.6 \times 10^{32}$ erg, which was stored in the volume below the 6 Mm height. Because we show that the volume integral magnetic free energy does not strongly depend on the initial condition, their result is also independent on the initial condition. However, we propose that the non-potentiality derived by the NLFFF extrapolation may be underestimated. Therefore, their results may also be affected by the underestimation of the NLFFF modeling.

Regarding the onset mechanism, Kusano et al. (2012) surveyed the conditions required for the occurrence of the eruptions based on the magnetic structures by the MHD simulations. They focused on the pre-flare small magnetic reconnection between the small magnetic structure near the magnetic polarity inversion lines and overlying magnetic field. Figure 4.1 shows the relation among the magnetic flux rope eruption and the azimuth of the small magnetic structures as the disturbance source (φ_e, horizontal axis) and the overlying magnetic field (θ_0, vertical axis). The squares and diamonds show the absence and presence of the eruption at the corresponding parameter, respectively, and contours show the maximum total kinetic energy produced by the eruption. They found that two different types of small magnetic structures favor the onset of solar eruptions, i.e., opposite polarity or reversed shear to the overlying field on the PIL, $\varphi_e = 100 \sim 250$ degree. The azimuth of the overlying magnetic field affects the total kinetic energy of the eruptive flux rope. Bamba et al. (2013) verified their model by the photospheric magnetic field measurements with *Hinode*/SOT for a few flares. In the study of Bamba et al. (2013), the angle of θ_0 is defined by the mean angle of the transverse photospheric magnetic field over the flare trigger region. They showed that some solar flares were triggered by the interaction between small magnetic structures and overlying magnetic fields. As the extension of the study of Bamba et al. (2013), Bamba & Kusano (2018) statistically investigated the small magnetic structure and the precursor brightenings for 32 flare events. However, they could not clearly determine small magnetic structures, which trigger the solar flares, in

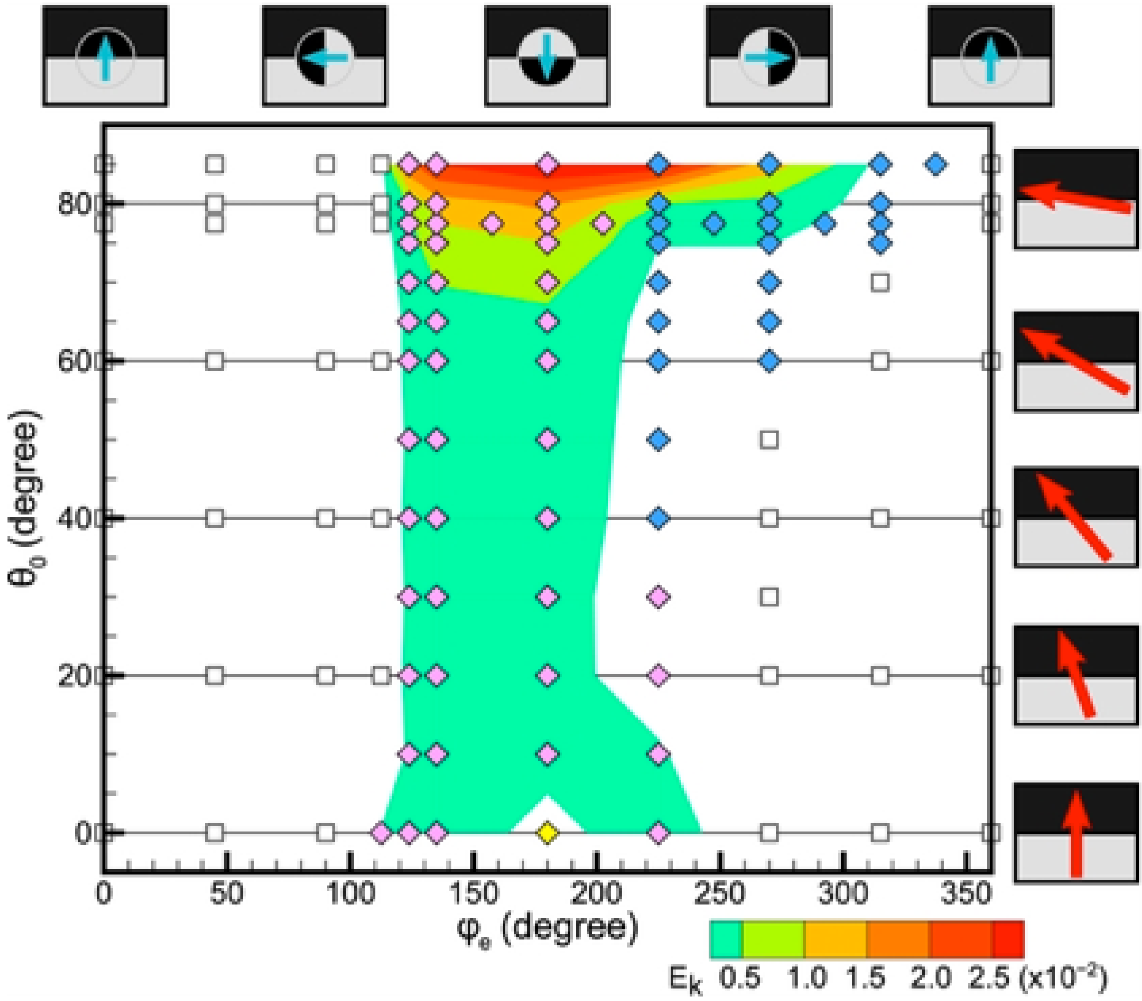

Figure 4.1: Squares (diamonds) represent the absence (presence) of the eruption, and contours show the maximum total kinetic energy produced by the eruption. The horizontal and vertical axises illustrate the azimuth of the small magnetic structures and the overlying magnetic fields, respectively. From Kusano et al. (2012).©AAS. Reproduced with permission

approximately 70% of their examined flare examples. Small pre-flare reconnection may occur at the lower coronal height or the chromospheric height. Because our results show the different non-potentiality between photosphere and chromosphere, the measurements of the chromospheric magnetic field before and/or during solar flares have the possibility to promote our understandings of the onset mechanism of solar flares. The MHD instabilities are also considered to be important mechanisms for the onset of the eruption of magnetic flux rope and are sensitive to the 3D magnetic field structure. The two kinds of the MHD instabilities (the kink instability and torus instability) are well known as the onset mechanism. The kink instability (Török et al., 2004) occurs when the twist of the magnetic flux rope exceeds a critical value. The kink instability is parameterized by the twist number T_w (Berger & Prior, 2006) of the flux rope, as follows,

$$T_w = \frac{1}{4\pi} \int \alpha dl, \tag{4.1}$$

where l is the length along the magnetic field line. The torus instability (Kliem & Török, 2006), on the other hand, occurs when the overlying field strapping the magnetic flux rope becomes weak. The criterion of the torus instability is defined by the decay index n,

$$n = -\frac{\partial \log(B_{\rm ext})}{\partial \log(h)}, \tag{4.2}$$

where $B_{\rm ext}$ is the overlying field at a geometrical height h above the photosphere. When the decay index at the height of the magnetic flux rope reaches the critical value ($n > 1.5$: Kliem & Török, 2006), the magnetic flux rope erupts. The relation among the eruption and MHD instabilities were investigated by Myers et al. (2015) based on plasma laboratory experiments and by Jing et al. (2018) based on solar observations. Myers et al. (2015) found that there are four regimes; eruptive, failed kink, failed torus, and stable. Failed kink and failed torus regimes corresponding to the regimes where the magnetic flux rope does not erupt even though the parameter satisfies the kink or torus criterion. They suggested that the dynamical magnetic tension force prevent the flux rope from erupting. To extend the view from the laboratory to the solar atmosphere, Jing et al. (2018) performed statistical study of the relation among the CME occurrence and MHD instabilities (the torus instability and kink instability) based on the NLFFF extrapolation, as shown in Figure 4.2. Their conclusion is that the kink instability plays little role in discriminating between confined and ejective events, which is not consistent with the results of Myers et al. (2015). On the other hand, the large decay index active regions produce CMEs (the gray solid line in Figure 4.2). Since both instabilities depend on

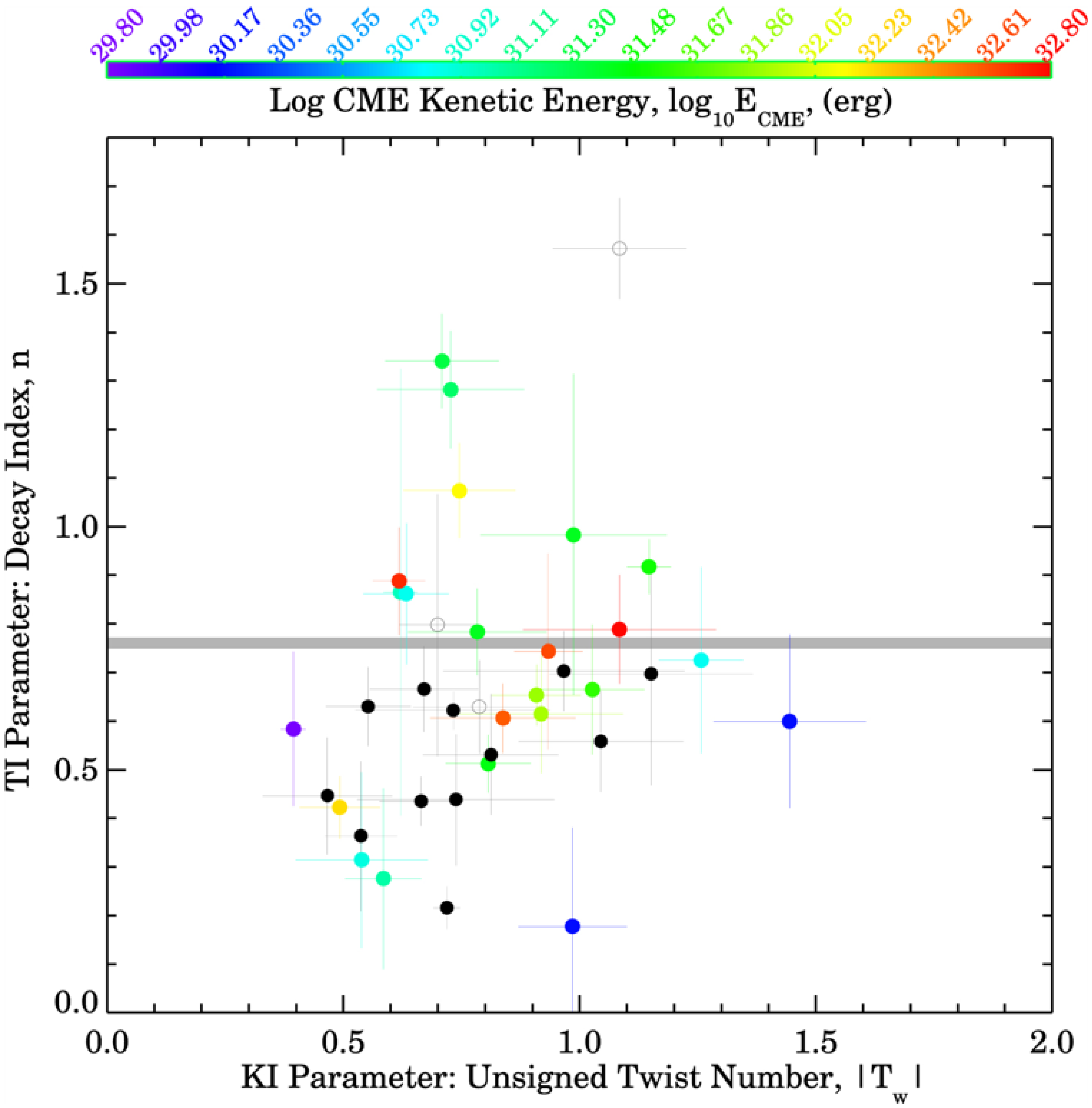

Figure 4.2: Scatter diagram of the torus instability parameter n vs. the kink instability parameter $|T_w|$. Black and colored symbols correspond to the confined and ejective flares, respectively. The color shows the kinetic energy of the CMEs. From Jing et al. (2018). ©AAS. Reproduced with permission

the 3D structure, this conclusion depends on the reliability of the NLFFF modelings. In terms of the kink instability, our results show that the magnitude of the underestimation of the non-potentiality is different between the two active regions in the SSA, as shown in Figures 3.7 and 3.10. To estimate how the twist number changes by underestimating the SSA, we consider the simple LFF magnetic field configuration, as follows,

$$\boldsymbol{B} = \begin{pmatrix} B_x \\ B_y \\ B_z \end{pmatrix} = B_0 \begin{pmatrix} \alpha_0 k^{-1} \cos ky \\ -lk^{-1} \cos ky \\ \sin ky \end{pmatrix} \exp(-lz), \tag{4.3}$$

where α_0 is the constant force-free parameter, k is a wave number, $l = (k^2 - \alpha_0^2)^{1/2}$, and B_0 is a constant. When $\alpha_0 = 0$, the magnetic field becomes potential field and the magnetic field vector is oriented parallel to the y-axis. With this magnetic field configuration, the SSA can be calculated as,

$$\begin{aligned} \mathrm{SSA} &= \tan^{-1}(-B_x/B_y), \qquad (4.4) \\ &= \tan^{-1}(\alpha_0/l), \qquad (4.5) \end{aligned}$$

By solving the equation above for α_0

$$\alpha_0 = \pm k \sin(\mathrm{SSA}). \tag{4.6}$$

Therefore, the force-free α depends on $\sin(\mathrm{SSA})$. The twist number is the integral of the force-free α along the field line as shown in Equation (4.1). The force-free α is constant along the field line in the force-free state. Then, the twist number can be calculated as follows,

$$T_w \sim \frac{1}{4\pi} \alpha L, \tag{4.7}$$

where L is the length of the field line. In the force-free state, the twist number increases linearly with α. Therefore, the twist number depends on $\sin(\mathrm{SSA})$. For example, when the SSA increases from 10 degree to 40 degree, the twist number increases by 3.7 times. On the other hand when the SSA increases from 30 degree to 50 degree, the twist number increases by only 1.5 times. Therefore, when the degree of the underestimation of the SSA is small such as case of NOAA 11158, the twist is underestimated by $\sim$ 2 times. However, for the case of NOAA 10969, the twist number will increase by more than 3 times compared to the NLFFF modeling from the photosphere. Therefore, the uncertainty of the NLFFF will significantly change independence of the twist number on the presence of ejective flares. Regarding the torus instability, when calculating the decay index, the height of the apex of the magnetic flux rope has to be determined. In the results of Jing et al. (2018), the height of the apex of the magnetic flux rope is in the range of $2 \sim 40$ Mm. We show that there is an initial condition dependence at 26 Mm in Figure 2.11, which may change their statistical result. In addition to the two instabilities, Ishiguro & Kusano (2017) proposed a new type of instability, which they call double arc instability. The double arc instability depends on the magnetic twist and the normalized reconnected magnetic flux. Therefore it is also important to derive accurate non-potentiality for analyzing this instability as a future task.

4.2 Improvement of NLFFF Extrapolation

As described above, our results have a possibility to change the conclusion of the previous studies by the NLFFF modeling because the non-potentiality in some active regions may be underestimated by the NLFFF modeling based on the photospheric magnetic field. As a future work, we need to improve the present extrapolation method. We discuss the future prospects of the improvement of NLFFF extrapolation based on the two point of view: One is a observational point of view. The other point of view is a technique of the NLFFF modeling.

4.2.1 Observational Point of View

From observational point of view, the promising way to improve the NLFFF is to use chromospheric magnetic field derived from spectropolarimetry as the additional information for the modeling. The chromospheric magnetic field is expected to improve the NLFFF modeling for estimating the magnetic field in the corona because the plasma beta is quiet low in the chromosphere compared with in the photosphere. However, as shown in the masked region in Figures 3.6 and 3.9, there are many pixels where the chromospheric magnetic field can not be correctly derived since the current observation of the chromospheric magnetic field does not provide sufficient signal-to-noise ratio. Therefore, it is difficult to use the chromospheric magnetic field derived by He I 10830 Å just as bottom boundary. We discuss three possible solutions to overcome the problem of the signal-to-noise ratio.

The first approach to solve the signal-to-ratio problem is using chromospheric B_z as additional information for the NLFFF modeling. With on-disk observations, B_z is determined mainly by the Stokes V, which can be obtained with sufficient signal-to-noise ratio compared to the Stokes Q and U. However, the results of our thesis imply that this approach has less possibility to improve the NLFFF modeling. Although there exists small deviation between chromospheric B_z from He I 10830 Å and NLFFF, they show good correlations in both active regions NOAA 10969 and 11861 as shown in Figures 3.11 and 3.12. This result indicates that only imposing B_z information may not improve the NLFFF modeling significantly.

The second approach is to gather more photons by the observation with the large aperture telescope. Daniel K. Inouye Solar Telescope (DKIST; Tritschler et al., 2016) will start to be operated in one or two years. The noise level in the linear polarization in this study with VTT is around 5.0×10^{-4} after binning process. The aperture of the VTT is 70 cm, while that of DKIST is 4 m. The photon noise will be improved with DKIST by a factor of 5$\sim$6 with the same spatial sampling, wavelength sampling, and exposure time.

One concern of the large aperture ground-based telescope is the limited size of the FOV. To solve this problem, the spectropolarimetric observation from space will be a promising approach, such as Solar UV-Visible-IR Telescope (SUVIT; Suematsu et al., 2017).

The third approach is to make self-consistent bottom boundary by using both photospheric and chromospheric magnetic field. The clue can be obtained from the technique of the preprocess (Wiegelmann et al., 2006). Preprocess technique is to drive the observed non force-free data towards suitable boundary conditions for a force-free extrapolation by minimizing the total force and torque on the bottom boundary. This technique is often applied to the photospheric magnetic field and the preprocessed magnetic field map is regarded as the pseudo chromospheric magnetic field map. However, this technique often works as smoothing the magnetic field map and the preprocessed magnetic field may not be similar to the real chromospheric magnetic field because our study shows the increase of the twist at the chromospheric height. We propose to make the artificial bottom boundary by using both photospheric and chromospheric magnetic field, whose concept comes from the study of Wiegelmann et al. (2008). They applied preprocess to the photospheric magnetic field before nonlinear force-free field extrapolation codes. The preprocess is composed of the force-free consistency integrals, spatial smoothing and match to the field direction as inferred from fibrils from chromospheric Hα observations. The flow chart of our proposal is summarized in Figure 4.3. The limitation of the FOV at the chromospheric height is compensated by the extrapolated field from the photosphere. In the combined field, there exists discontinuity between observed chromospheric field and extrapolated field. In addition, there are relatively large statistical noises in the horizontal magnetic field at the chromosphere. By applying the preprocess to the combined map, we can obtain the artificial force-free field map with smoothing the statistical noise, which reflects the information of the chromospheric magnetic field.

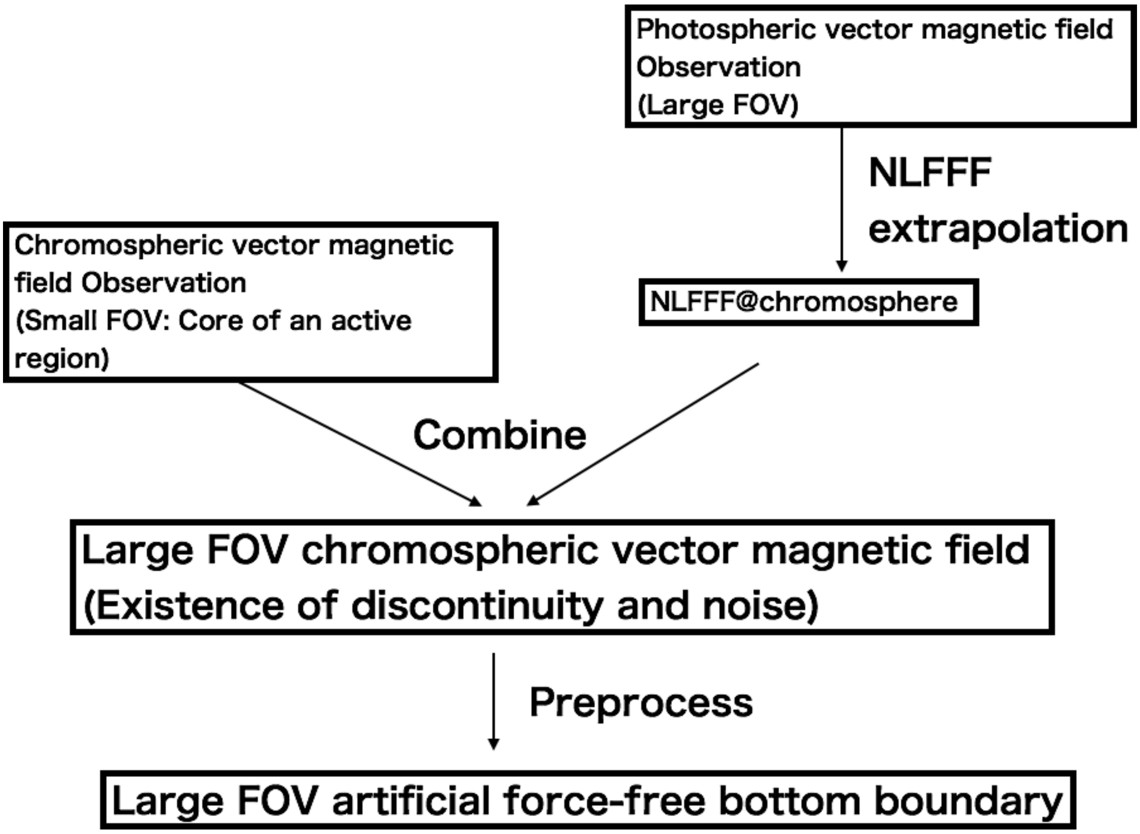

Figure 4.3: Flow chart to obtain the artificial force-free bottom boundary.

4.2.2 Technical Point of View

From the point of view of the technique of the NLFFF modeling, our study shows the non-uniqueness of the NLFFF at the higher region. Therefore, we have to develop the method to obtain the NLFFF solution, which is consistent to the coronal or chromospheric image.

First approach is to set the initial condition which is similar to the X-ray or EUV imaging observation. This approach aims to estimate the global force-free alpha by detecting the field lines from the X-ray or EUV imaging observations. If we choose the LFFF with the estimated constant force-free α as an initial condition, we may obtain the consistent NLFFF results with observations.

Second approach is more sophisticated, which comes from the study of Aschwanden (2016), who tried to minimize the misalignment angles between observed coronal loops and theoretical model field lines. To perform above two approaches, it is necessary to develop a method to detect magnetic field lines from X-ray or EUV imaging observations. With the state-of-art curvilinear tracing method developed by Aschwanden et al. (2013), it is difficult to detect sigmoidal field lines. We are now working on developing the method to detect the sigmoidal field lines (Kawabata et al., 2018), which will be applied to the improvement of the NLFFF. In addition, multi-wavelength observations at EUV or X-ray will be necessary because the coronal loop morphology is different among different wavelengths. Multi-wavelength EUV observations of the future mission, such as Solar-C_EUVST (Imada & Suematsu, 2018), will help the detection of coronal loops and lead to the improvement of the NLFFF modeling.

Chapter 5

Conclusion

The novelties and findings in this thesis are summarized in this chapter. We focused on the non-potential magnetic field and its 3D structure in the active regions. The novelties in our studies are followings.

1. We investigated the dependence of the NLFFF calculation with respect to the initial guess of the 3D magnetic field. While previous studies often use potential field as the initial guess for the NLFFF modeling, we adopted the linear force-free fields with different constant force-free alpha as the initial guesses. This method enabled us to investigate how unique the magnetic field obtained with the NLFFF extrapolation is.

2. The derivation of the chromospheric magnetic field in the whole active regions are performed by the spectropolarimetric observations at He I 10830 Å. In addition to the chromospheric observations, the results of NLFFF extrapolation from the photosphere are compared with the direct measurements. The comparisons allow quantitative estimation of the NLFFF uncertainty.

With these novelties, we obtained following findings.

1. The dependence of the initial condition of the NLFFF extrapolation is smaller in the strong magnetic field region. Therefore, the magnetic field at the lower height

(< 10 Mm) tends to be less affected by the initial condition (correlation coefficient $C > 0.9$ with different initial condition), although the Lorentz force is concentrated at the lower height. The 10-100 times larger Lorentz force, which is normalized by the square of the magnetic field strength, remains at the lower height (< 10 Mm) than that at higher region (> 10 Mm).

2. Chromospheric magnetic field may have larger non-potentiality compared to the photospheric magnetic field. The large non-potentiality in the chromospheric height may not be reproduced by the NLFFF extrapolation with the photospheric magnetic field. The magnitude of the underestimation of the non-potentiality is 30-40 degree in signed shear angle at many locations.

Our results indicate that although the NLFFF extrapolation produces less dependent result on the initial condition at the lower height, the non-potentiality is underestimated at the chromospheric height. From a comparative analysis of the chromospheric magnetic field and the NLFFF extrapolation for two active regions, we reveal that the magnetic field in the upper atmosphere may have higher non-potentiality than previously thought based on the NLFFF modeling. Our studies emphasize the importance of the chromospheric magnetic field measurements for more accurate 3D magnetic field modeling and the understanding of the non-potentiality in active regions corona. Because the non-potentiality is crucial in the MHD instability, our findings would improve the understanding of the onset mechanisms for solar flares and CMEs, which affect the environment in the solar system. In the current state, the chromospheric magnetic field observations in active regions are very few in number. We strongly suggest that we should make efforts to perform much more observations of the chromospheric magnetic field in flare-productive active regions with the future large aperture telescopes, giving improvement of the 3D magnetic field modeling.

Appendix A

Appendix

A.1 Spatial Scale Dependence of Force-Freeness

To investigate the spatial scale dependence of the force-freeness, we applied the lowpass filter to vector magnetic field maps in the photosphere and calculated the force-freeness. Panels (a) of Figures A.1 and A.2 show the absolute value of the Fourier component of vertical magnetic field, $|\tilde{B}_z(\boldsymbol{k})|$, where $\boldsymbol{k}$ is a wave vector. We used two different low pass filters (filter 1 and 2), whose cutoff wave numbers are different. Note that wave number k and length scale L are related by expression $k = 1/L$. Panels (b), (c), and (d) in Figures A.1 and A.2 show the original and lowpass filtered vector magnetic field maps (B_z, B_x, and B_y, respectively) for NOAA 10969 and NOAA 11861, respectively.

The values of force-freeness are summarized in Table A.1. For NOAA 10969, the value of $|F_z|/F_p$ tend to become smaller, when we remove the small spatial scale magnetic field. The value of $|F_x|/F_p$ increases by applying the lowpass filter and there is no clear tendency of increase or decrease for $|F_y|/F_p$. For NOAA 11861, $|F_z|/F_p$ and $|F_x|/F_p$ do not have tendency of increase or decrease by applying the lowpass filter, while $|F_y|/F_p$ tends to decrease. From above results, we suspect that lowpass filter reduce the value of force-freeness when the original value of the force-freeness is relatively large, e.g. $|F_z|/F_p$ of NOAA 10969. Although the value of $|F_z|/F_p$ reduces to 0.35 by using the filter 2, this value is not sufficiently small to be regarded as force-free. Therefore NOAA 10969 can not be regarded force-free even when we consider only large scale magnetic field.

Table A.1: Force-freeness of the active region from Eqns (1.16), (1.17), and (1.18)

	NOAA 10969 (No lowpass filter)	NOAA 10969 (Filter 1)	NOAA 10969 (Filter 2)
$\lvert F_x\rvert/F_p$	0.018	0.022	0.039
$\lvert F_y\rvert/F_p$	0.038	0.035	0.036
$\lvert F_z\rvert/F_p$	0.43	0.40	0.35
	NOAA 11861 (No lowpass filter)	NOAA 11861 (Filter 1)	NOAA 11861 (Filter 2)
$\lvert F_x\rvert/F_p$	0.024	0.026	0.025
$\lvert F_y\rvert/F_p$	0.071	0.059	0.034
$\lvert F_z\rvert/F_p$	0.03	0.056	0.052

A.2 Field of View Dependence of Force-Freeness

To estimate the dependence of the force-freeness on the field of view (FOV), we calculate the force-freeness of the active regions analyzed in Chapter 3 with different FOVs. The black boxes of Figure A.3 show the FOVs, which are used for calculation of the force-freeness. Table A.2 shows the force-freeness calculated with each FOV. For NOAA 10969, $|F_z|/F_p$ and $|F_y|/F_p$ increase as the FOV becomes large, while $|F_x|/F_p$ shows no trend with increasing the FOV. For NOAA 11861, $|F_x|/F_p$ and $|F_y|/F_p$ tend to decrease with increasing the FOV. For both active regions, while increasing FOVs from FOV 1 to FOV 3 changes the force-freeness, the difference between FOV 3 and full FOV is comparatively small. This result indicates that the force-freeness will not change significantly with increasing the FOV when the main magnetic flux is covered with the FOV. This result is consistent with the result of Zhang et al. (2017). They presented that the FOV would

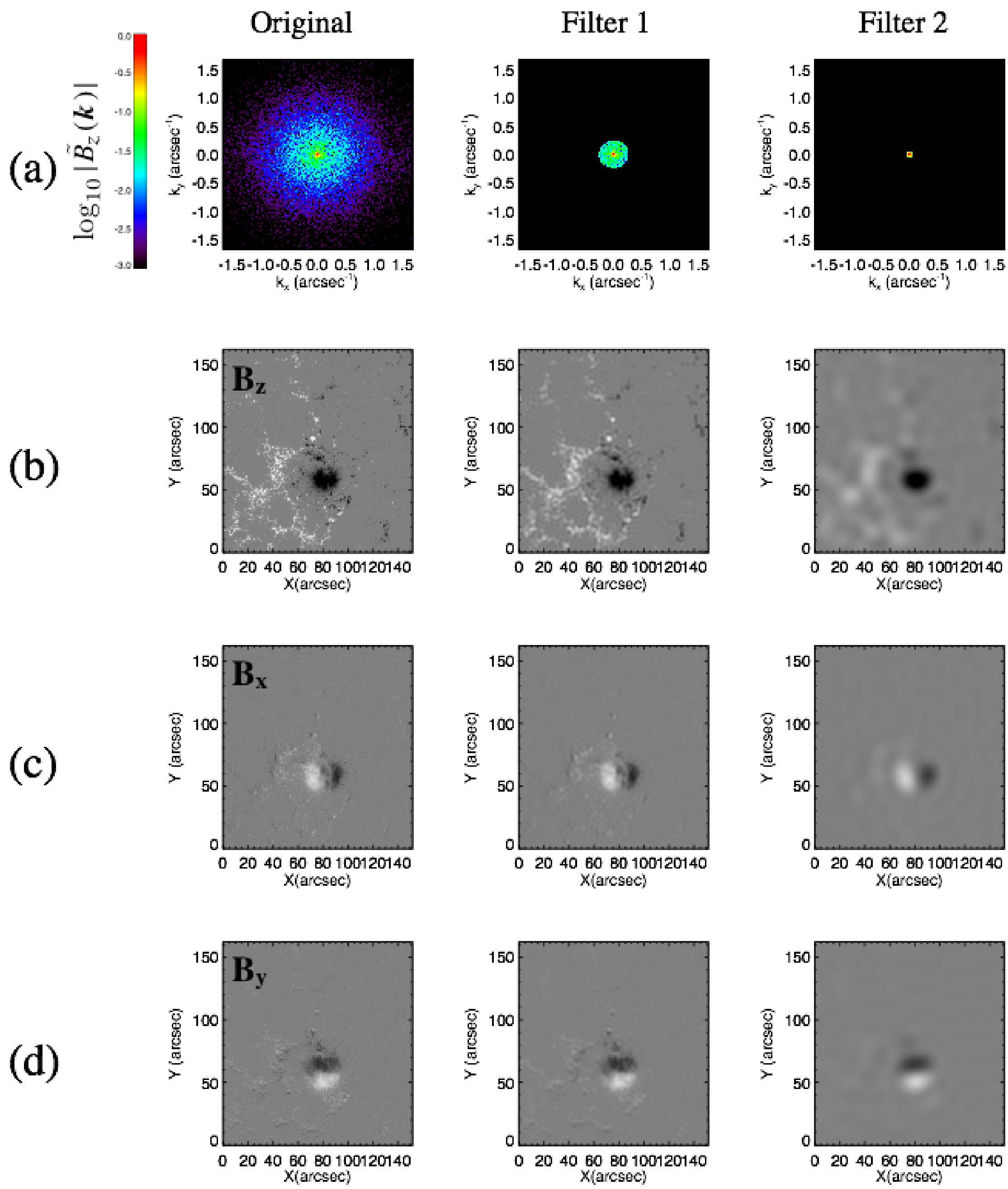

Figure A.1: Panels (a): The absolute value of the Fourier component of vertical magnetic field, $|\tilde{B}_z(\boldsymbol{k})|$ for NOAA 10969. Panels (b), (c), abd (d): Original (left) and lowpass filtered (middle and right) vector magnetic field maps in the photosphere.

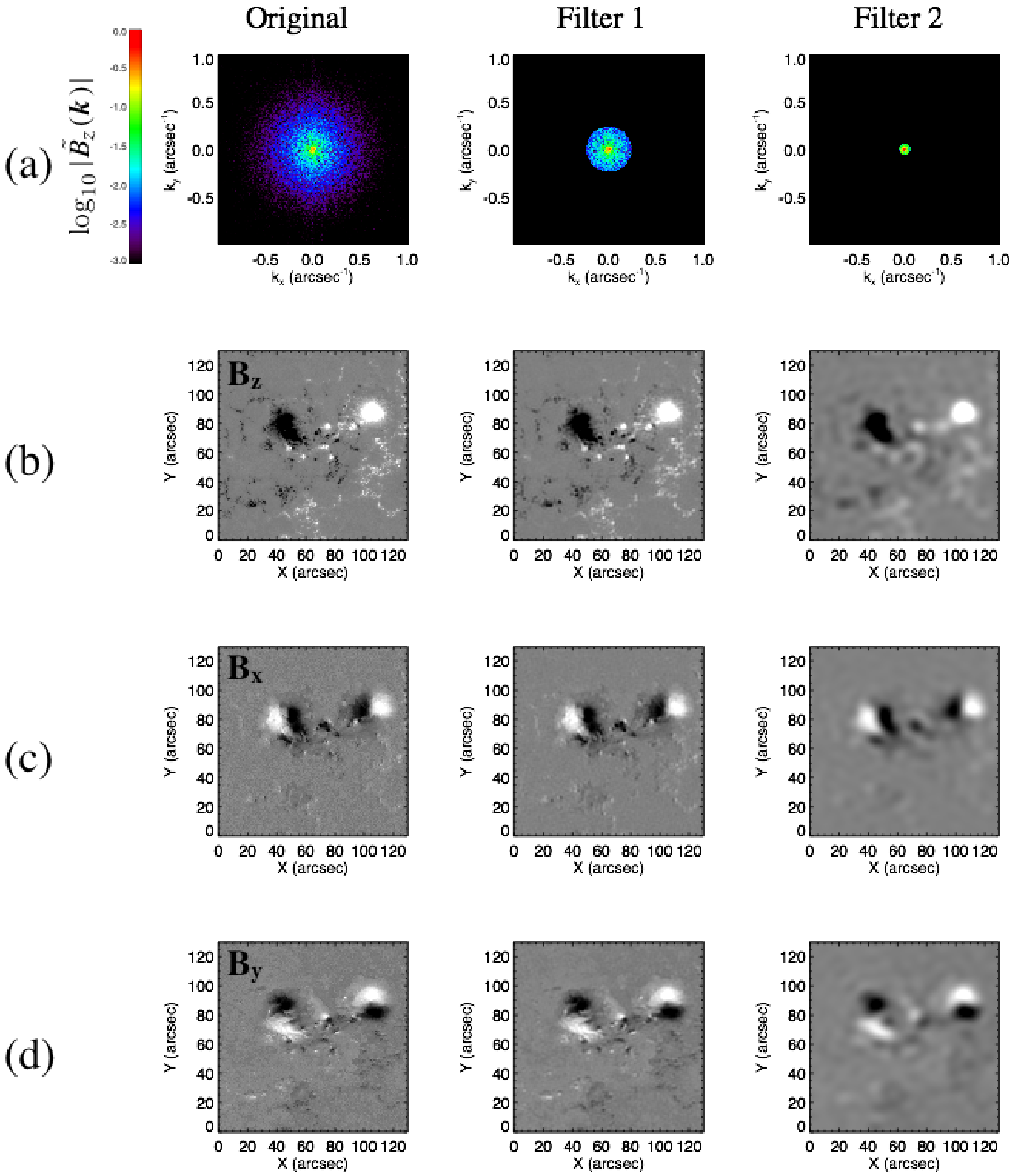

Figure A.2: Panels (a): The absolute value of the Fourier component of vertical magnetic field, $|\tilde{B}_z(\boldsymbol{k})|$ for NOAA 11861. Panels (b), (c), abd (d): Original (left) and lowpass filtered (middle and right) vector magnetic field maps in the photosphere.

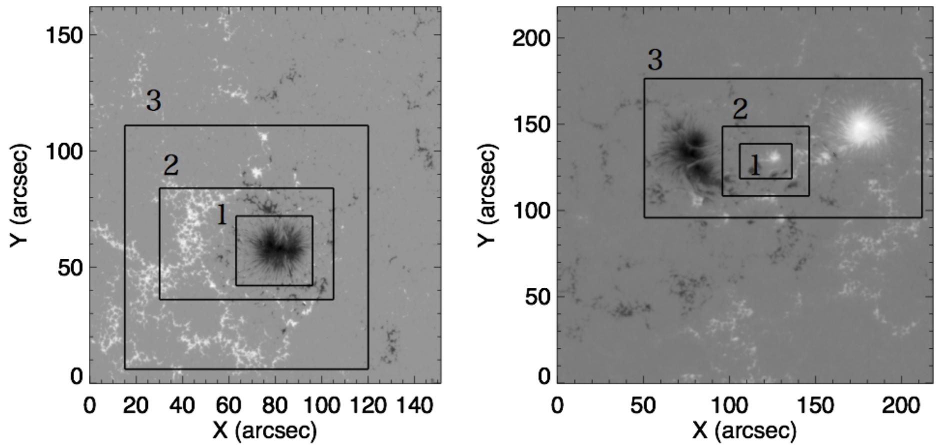

Figure A.3: The FOVs for the calculation of the force-freeness in Table A.2 for NOAA 10969 (left panel) and 11861 (right panel). Gray scale shows the vertical component of the magnetic field.

not significantly influence the force-freeness if magnetic flux imbalance is less than 10 %, in other words, the FOV covers most of the magnetic flux in the active region. The flux imbalances of NOAA 10969 and NOAA 11861 are 11% and 0.01% for full FOV, respectively. Therefore, the force-freeness of NOAA 10969 is expected to change slightly if we expand the current FOV, while that of NOAA 11861 will not change significantly with increasing the current FOV.

Table A.2: Force-freeness of the active region from Eqns (1.16), (1.17), and (1.18)

	NOAA 10969 (FOV 1)	NOAA 10969 (FOV 2)	NOAA 10969 (FOV 3)	NOAA 10969 (full FOV)
$\vert F_x\vert/F_p$	0.046	0.017	0.014	0.018
$\vert F_y\vert/F_p$	0.0011	0.019	0.028	0.038
$\vert F_z\vert/F_p$	0.18	0.31	0.40	0.43
	NOAA 11861 (FOV 1)	NOAA 11861 (FOV 2)	NOAA 11861 (FOV 3)	NOAA 11861 (full FOV)
$\vert F_x\vert/F_p$	0.11	0.048	0.022	0.024
$\vert F_y\vert/F_p$	0.33	0.21	0.059	0.071
$\vert F_z\vert/F_p$	0.084	0.11	0.038	0.03

References

Alissandrakis, C. E. 1981, A&A, 100, 197

Amari, T., Canou, A., & Aly, J.-J. 2014, Nature, 514, 465

Antiochos, S. K., DeVore, C. R., & Klimchuk, J. A. 1999, ApJ, 510, 485

Aschwanden, M., De Pontieu, B., & Katrukha, E. 2013, Entropy, 15, 3007

Aschwanden, M. J. 2016, ApJS, 224, 25

Asensio Ramos, A., de la Cruz Rodríguez, J., Martínez González, M. J., & Socas-Navarro, H. 2017, A&A, 599, A133

Asensio Ramos, A., Trujillo Bueno, J., & Landi Degl'Innocenti, E. 2008, ApJ, 683, 542

Bamba, Y., & Kusano, K. 2018, ApJ, 856, 43

Bamba, Y., Kusano, K., Yamamoto, T. T., & Okamoto, T. J. 2013, ApJ, 778, 48

Beck, C., Schmidt, W., Kentischer, T., & Elmore, D. 2005, A&A, 437, 1159

Benz, A. O. 2017, Living Reviews in Solar Physics, 14, 2

Berger, M. A., & Prior, C. 2006, Journal of Physics A Mathematical General, 39, 8321

Bineau, M. 1972, Comm. Pure and Applied, 25, 77

Bobra, M. G., Sun, X., Hoeksema, J. T., Turmon, M., Liu, Y., Hayashi, K., Barnes, G., & Leka, K. D. 2014, Sol. Phys., 289, 3549

Borrero, J. M., & Ichimoto, K. 2011, Living Reviews in Solar Physics, 8, 4

Casini, R., Judge, P. G., & Schad, T. A. 2012, ApJ, 756, 194

Chiu, Y. T., & Hilton, H. H. 1977, ApJ, 212, 873

Chodura, R., & Schlueter, A. 1981, Journal of Computational Physics, 41, 68

Collados, M., Lagg, A., Díaz Garcí A, J. J., Hernández Suárez, E., López López, R., Páez Mañá, E., & Solanki, S. K. 2007, in Astronomical Society of the Pacific Conference Series, Vol. 368, The Physics of Chromospheric Plasmas, ed. P. Heinzel, I. Dorotovič, & R. J. Rutten, Heinzel

Collados, M., Rodríguez Hidalgo, I., Bellot Rubio, L., Ruiz Cobo, B., & Soltau, D. 1999, in Astronomische Gesellschaft Abstract Series, Vol. 15, Astronomische Gesellschaft Abstract Series, ed. R. E. Schielicke, 11

Collados, M. V. 2003, in Proc. SPIE, Vol. 4843, Polarimetry in Astronomy, ed. S. Fineschi, 55–65

de la Cruz Rodríguez, J., & Socas-Navarro, H. 2011, A&A, 527, L8

de la Cruz Rodríguez, J., & van Noort, M. 2017, Space Sci. Rev., 210, 109

De Rosa, M. L., et al. 2009, ApJ, 696, 1780

Dedner, A., Kemm, F., Kröner, D., Munz, C.-D., Schnitzer, T., & Wesenberg, M. 2002, Journal of Computational Physics, 175, 645

del Toro Iniesta, J. C. 2007, Introduction to Spectropolarimetry

Delbouille, L., Roland, G., Brault, J. W., & Testerman, L. 1981

DeRosa, M. L., et al. 2015, ApJ, 811, 107

Gary, G. A. 2001, Sol. Phys., 203, 71

Golub, L., et al. 2007, Sol. Phys., 243, 63

Grad, H., & Rubin, H. 1958, Journal of Nuclear Energy (1954), 7, 284

Hagyard, M. J., Teuber, D., West, E. A., & Smith, J. B. 1984, Sol. Phys., 91, 115

Hale, G. E. 1908, ApJ, 28, 315

Handy, B. N., et al. 1999, Sol. Phys., 187, 229

Ichimoto, K., et al. 2008, Sol. Phys., 249, 233

Imada, S., & Suematsu, Y. 2018, in 42nd COSPAR Scientific Assembly, Vol. 42, E2.2–37–18

Inoue, S., Hayashi, K., Shiota, D., Magara, T., & Choe, G. S. 2013, ApJ, 770, 79

Inoue, S., Kusano, K., Büchner, J., & Skála, J. 2018, Nature Communications, 9, 174

Inoue, S., Magara, T., Pandey, V. S., Shiota, D., Kusano, K., Choe, G. S., & Kim, K. S. 2014, ApJ, 780, 101

Inoue, S., Shiota, D., Yamamoto, T. T., Pandey, V. S., Magara, T., & Choe, G. S. 2012, ApJ, 760, 17

Ishiguro, N., & Kusano, K. 2017, ApJ, 843, 101

Jaeggli, S. A., Lin, H., Mickey, D. L., Kuhn, J. R., Hegwer, S. L., Rimmele, T. R., & Penn, M. J. 2010, MmSAI, 81, 763

Jiang, C., Wu, S. T., Feng, X., & Hu, Q. 2014, ApJ, 786, L16

Jing, J., Liu, C., Lee, J., Ji, H., Liu, N., Xu, Y., & Wang, H. 2018, ApJ, 864, 138

Joshi, J., Lagg, A., Hirzberger, J., & Solanki, S. K. 2017, A&A, 604, A98

Kawabata, Y., Iida, Y., Doi, T., Akiyama, S., Yashiro, S., & Shimizu, T. 2018, ApJ, 869, 99

Kawabata, Y., Inoue, S., & Shimizu, T. 2017, ApJ, 842, 106

Kliem, B., & Török, T. 2006, Physical Review Letters, 96, 255002

Kosugi, T., et al. 2007, Sol. Phys., 243, 3

Krall, K. R., Smith, Jr., J. B., Hagyard, M. J., West, E. A., & Cummings, N. P. 1982, Sol. Phys., 79, 59

Kruskal, M., & Schwarzschild, M. 1954, Proceedings of the Royal Society of London Series A, 223, 348

Kusano, K., Bamba, Y., Yamamoto, T. T., Iida, Y., Toriumi, S., & Asai, A. 2012, ApJ, 760, 31

Lagg, A., Woch, J., Krupp, N., & Solanki, S. K. 2004, A&A, 414, 1109

Landi Degl'Innocenti, E., & Landolfi, M., eds. 2004, Astrophysics and Space Science Library, Vol. 307, Polarization in Spectral Lines

Leka, K. D., Barnes, G., & Crouch, A. 2009, in Astronomical Society of the Pacific Conference Series, Vol. 415, The Second Hinode Science Meeting: Beyond Discovery-Toward Understanding, ed. B. Lites, M. Cheung, T. Magara, J. Mariska, & K. Reeves, 365

Leka, K. D., Canfield, R. C., McClymont, A. N., & van Driel-Gesztelyi, L. 1996, ApJ, 462, 547

Lemen, J. R., et al. 2012, Sol. Phys., 275, 17

Lites, B. W., & Ichimoto, K. 2013, Sol. Phys., 283, 601

Lites, B. W., Socas-Navarro, H., Skumanich, A., & Shimizu, T. 2002, ApJ, 575, 1131

Lites, B. W., et al. 2013, Sol. Phys., 283, 579

Liu, S., Su, J. T., Zhang, H. Q., Deng, Y. Y., Gao, Y., Yang, X., & Mao, X. J. 2013, PASA, 30, e005

Low, B. C. 1985, in Measurements of Solar Vector Magnetic Fields, ed. M. J. Hagyard

Martínez-Sykora, J., De Pontieu, B., Carlsson, M., & Hansteen, V. 2016, ApJ, 831, L1

Merenda, L., Lagg, A., & Solanki, S. K. 2011, A&A, 532, A63

Metcalf, T. R. 1994, Sol. Phys., 155, 235

Metcalf, T. R., Jiao, L., McClymont, A. N., Canfield, R. C., & Uitenbroek, H. 1995, ApJ, 439, 474

Metcalf, T. R., et al. 2008, Sol. Phys., 247, 269

Mikic, Z., & McClymont, A. N. 1994, in Astronomical Society of the Pacific Conference Series, Vol. 68, Solar Active Region Evolution: Comparing Models with Observations, ed. K. S. Balasubramaniam & G. W. Simon, 225

Moon, Y.-J., Choe, G. S., Yun, H. S., Park, Y. D., & Mickey, D. L. 2002, ApJ, 568, 422

Moore, R. L., Sterling, A. C., Hudson, H. S., & Lemen, J. R. 2001, ApJ, 552, 833

Muhamad, J., Kusano, K., Inoue, S., & Bamba, Y. 2018, ApJ, 863, 162

Muhamad, J., Kusano, K., Inoue, S., & Shiota, D. 2017, ApJ, 842, 86

Myers, C. E., Yamada, M., Ji, H., Yoo, J., Fox, W., Jara-Almonte, J., Savcheva, A., & Deluca, E. E. 2015, Nature, 528, 526

Nakagawa, Y. 1974, ApJ, 190, 437

Parker, E. N. 1974, ApJ, 191, 245

Pesnell, W. D., Thompson, B. J., & Chamberlin, P. C. 2012, Sol. Phys., 275, 3

Pevtsov, A. A., Canfield, R. C., & McClymont, A. N. 1997, ApJ, 481, 973

Pevtsov, A. A., Canfield, R. C., & Metcalf, T. R. 1995, ApJ, 440, L109

Priest, E. 2014, Magnetohydrodynamics of the Sun

Régnier, S., & Amari, T. 2004, A&A, 425, 345

Rempel, M., & Schlichenmaier, R. 2011, Living Reviews in Solar Physics, 8, 3

Savcheva, A. S., van Ballegooijen, A. A., & DeLuca, E. E. 2012, ApJ, 744, 78

Schad, T. A., Penn, M. J., & Lin, H. 2013, ApJ, 768, 111

Schad, T. A., Penn, M. J., Lin, H., & Tritschler, A. 2015, Sol. Phys., 290, 1607

Schlichenmaier, R. 2009, Space Sci. Rev., 144, 213

Schou, J., et al. 2012, Sol. Phys., 275, 229

Schrijver, C. J., et al. 2006, Sol. Phys., 235, 161

—. 2008, ApJ, 675, 1637

Shimizu, T., et al. 2008, Sol. Phys., 249, 221

Socas-Navarro, H. 2001, in Astronomical Society of the Pacific Conference Series, Vol. 236, Advanced Solar Polarimetry – Theory, Observation, and Instrumentation, ed. M. Sigwarth, 487

Solanki, S. K. 2003, A&A Rv, 11, 153

Solanki, S. K., Lagg, A., Woch, J., Krupp, N., & Collados, M. 2003, Nature, 425, 692

Suematsu, Y., Katsukawa, Y., Shimizu, T., Ichimoto, K., Horiuchi, T., Matsumoto, Y., & Takeyama, N. 2017, in Society of Photo-Optical Instrumentation Engineers (SPIE) Conference Series, Vol. 10565, Society of Photo-Optical Instrumentation Engineers (SPIE) Conference Series, 105650R

Suematsu, Y., et al. 2008, Sol. Phys., 249, 197

Sun, X., Hoeksema, J. T., Liu, Y., Wiegelmann, T., Hayashi, K., Chen, Q., & Thalmann, J. 2012, ApJ, 748, 77

Thalmann, J. K., Tiwari, S. K., & Wiegelmann, T. 2013, ApJ, 769, 59

Title, A. M., Frank, Z. A., Shine, R. A., Tarbell, T. D., Topka, K. P., Scharmer, G., & Schmidt, W. 1993, ApJ, 403, 780

Titov, V. S. 2007, ApJ, 660, 863

Tiwari, S. K., Venkatakrishnan, P., Gosain, S., & Joshi, J. 2009a, ApJ, 700, 199

Tiwari, S. K., Venkatakrishnan, P., & Sankarasubramanian, K. 2009b, ApJ, 702, L133

Török, T., Kliem, B., & Titov, V. S. 2004, A&A, 413, L27

Tritschler, A., et al. 2016, Astronomische Nachrichten, 337, 1064

Trujillo Bueno, J. 2001, in Astronomical Society of the Pacific Conference Series, Vol. 236, Advanced Solar Polarimetry – Theory, Observation, and Instrumentation, ed. M. Sigwarth, 161

Trujillo Bueno, J. 2003, in Astronomical Society of the Pacific Conference Series, Vol. 288, Stellar Atmosphere Modeling, ed. I. Hubeny, D. Mihalas, & K. Werner, 551

Tsuneta, S., et al. 2008, Sol. Phys., 249, 167

Valori, G., Green, L. M., Démoulin, P., Vargas Domínguez, S., van Driel-Gesztelyi, L., Wallace, A., Baker, D., & Fuhrmann, M. 2012, Sol. Phys., 278, 73

van Driel-Gesztelyi, L., & Green, L. M. 2015, Living Reviews in Solar Physics, 12, 1

Vernazza, J. E., Avrett, E. H., & Loeser, R. 1981, ApJS, 45, 635

Wang, H., et al. 2017, Nature Astronomy, 1, 0085

Wang, R., Liu, Y. D., Yang, Z., & Hu, H. 2014, ApJ, 791, 84

Wheatland, M. S., Sturrock, P. A., & Roumeliotis, G. 2000, ApJ, 540, 1150

Wiegelmann, T., Inhester, B., & Sakurai, T. 2006, Sol. Phys., 233, 215

Wiegelmann, T., & Neukirch, T. 2006, A&A, 457, 1053

Wiegelmann, T., & Sakurai, T. 2012, Living Reviews in Solar Physics, 9, 5

Wiegelmann, T., Thalmann, J. K., Schrijver, C. J., De Rosa, M. L., & Metcalf, T. R. 2008, Sol. Phys., 247, 249

Xu, Z., Lagg, A., Solanki, S., & Liu, Y. 2012, ApJ, 749, 138

Yamamoto, T. T., & Kusano, K. 2012, ApJ, 752, 126

Yelles Chaouche, L., Kuckein, C., Martínez Pillet, V., & Moreno-Insertis, F. 2012, ApJ, 748, 23

Zhang, X. M., Zhang, M., & Su, J. T. 2017, ApJ, 834, 80